98/12-21-95 JS ①

ANL-95/36

Energy Technology Division
Energy Technology Division
Energy Technology Division
Energy Technology Division
Energy Technology Division
Energy Technology Division
Energy Technology Division
Energy Technology Division
Energy Technology Division
Energy Technology Division
Energy Technology Division
Energy Technology Division
Energy Technology Division
Energy Technology Division
Energy Technology Division
Energy Technology Division
Energy Technology Division
Energy Technology Division
Energy Technology Division
Energy Technology Division
Energy Technology Division
Energy Technology Division
Energy Technology Division
Energy Technology Division
Energy Technology Division
Energy Technology Division
Energy Technology Division
Energy Technology Division
Energy Technology Division
Energy Technology Division
Energy Technology Division
Energy Technology Division
Energy Technology Division
Energy Technology Division

The DART Dispersion Analysis Research Tool: A Mechanistic Model for Predicting Fission-Product-Induced Swelling of Aluminum Dispersion Fuels

User's Guide for Mainframe, Workstation, and Personal Computer Applications

by J. Rest

Argonne National Laboratory, Argonne, Illinois 60439
operated by The University of Chicago
for the United States Department of Energy under Contract W-31-109-Eng-38

Energy Technology Division
Energy Technology Division
Energy Technology Division
Energy Technology Division
Energy Technology Division
Energy Technology Division
Energy Technology Division
Energy Technology Division

DISTRIBUTION OF THIS DOCUMENT IS UNLIMITED

Reproduced from the best available copy.

Available to DOE and DOE contractors from the
Office of Scientific and Technical Information
P.O. Box 62
Oak Ridge, TN 37831
Prices available from (423) 576-8401

Available to the public from the
National Technical Information Service
U.S. Department of Commerce
5285 Port Royal Road
Springfield, VA 22161

ARGONNE NATIONAL LABORATORY
9700 South Cass Avenue, Argonne, Illinois 60439

ANL-95/36
Distribution Category: Mathematics and Computer Sciences (UC-505)

The DART Dispersion Analysis Research Tool: A Mechanistic Model for Predicting Fission-Product-Induced Swelling of Aluminum Dispersion Fuels

User's Guide for Mainframe, Workstation, and Personal Computer Applications

J. Rest
Energy Technology Division

August 1995

Work sponsored by
U.S. Department of Energy
Office of Arms Control and Nonproliferation
Contract W–31–109–Eng–38

The DART Dispersion Analysis Research Tool: A Mechanistic Model for Predicting Fission-Product-Induced Swelling of Aluminum Dispersion Fuels

User's Guide for Mainframe,
Workstation, and Personal Computer Applications

by

J. Rest

Abstract

This report describes the primary physical models that form the basis of the DART mechanistic computer model for calculating fission-product-induced swelling of aluminum dispersion fuels; the calculated results are compared with test data. In addition, DART calculates irradiation-induced changes in the thermal conductivity of the dispersion fuel, as well as fuel restructuring due to aluminum fuel reaction, amorphization, and recrystallization. Input instructions for execution on mainframe, workstation, and personal computers are provided, as is a description of DART output. The theory of fission gas behavior and its effect on fuel swelling is discussed. The behavior of these fission products in both crystalline and amorphous fuel and in the presence of irradiation-induced recrystallization and crystalline-to-amorphous-phase change phenomena is presented, as are models for these irradiation-induced processes.

Contents

Figures

Tables

Executive Summary

DART, a thermomechanical model for the prediction of fission-product-induced swelling in aluminum dispersion fuels, has been applied to the analysis of U_3Si and U_3Si_2 dispersion fuel swelling in plate, tube, and rod fuel element geometries for research reactor applications. The model calculates irradiation-induced swelling of fission gas bubbles as a function of fuel morphology. The DART mechanical model calculates the behavior of a rod, tube, or plate during closure of as-fabricated porosity, during which the fuel particle swelling is accommodated by the relatively soft aluminum matrix flowing into the existing porosity; it also calculates the subsequent macroscopic changes in rod diameter or plate/tube thickness caused by additional fuel deformation processes. DART also includes a calculation for the effect of irradiation on the thermal conductivity of the dispersion fuel, and for fuel restructuring due to the aluminum fuel reaction, amorphization, and recrystallization.

This report describes the primary physical models that form the basis of the DART mechanistic computer model for calculating fission-product induced-swelling of aluminum dispersion fuels. In addition, it compares calculated results with test data. Input instructions for execution on mainframe, workstation, and personal computers are provided, as is a description of DART output. The theory of noble-gas behavior and its effect on fuel swelling is discussed. The behavior of the fission products in both crystalline and amorphous fuel and in the presence of irradiation-induced recrystallization and crystalline-to-amorphous-phase change phenomena is presented, as are models for these irradiation-induced processes.

1 Introduction

DART, a thermomechanical model for the prediction of fission-product-induced swelling in aluminum dispersion fuels, has been applied to the analysis of U_3Si and U_3Si_2 dispersion fuel swelling in both plate and rod fuel element geometries for research reactor applications. The model calculates irradiation-induced swelling of solid fission products and of fission gas bubbles as a function of fuel morphology. The DART mechanical model calculates the behavior of a rod, tube, or plate during closure of as-fabricated porosity, during which the fuel particle swelling is accommodated through the relatively soft aluminum matrix flowing into the existing porosity; it also calculates the subsequent macroscopic changes in rod diameter or plate/tube thickness caused by additional fuel deformation processes. DART also includes a calculation for the effect of irradiation on the thermal conductivity of the bulk material.

This report describes the primary physical models that form the basis of the DART mechanistic computer model for calculating fission-product-induced swelling of aluminum dispersion fuels In addition, it compares calculated results with test data. Input instructions for execution on mainframe and personal computers are provided, as is a description of DART output. The theory of noble-gas behavior and its effect on fuel swelling is discussed. The behavior of the fission products in the presence of irradiation-induced recrystallization and crystallin-to-amorphous phase change phenomena is presented, as are models for these irradiation-induced processes.

The DART fission gas swelling model is based on the mechanistic Steady–State and Transient-Gas Release and Swelling Subroutine (GRASS–SST) [1]. Models are included for the effects of fission-product generation, atomic migration, bubble nucleation and re-solution, bubble migration and coalescence, bubble pinning and growth on dislocations and grain boundaries, grain growth and grain boundary sweeping, channel formation on grain faces, the existence of a fixed density of nodes that are identified as grain-edge corners or triple points, porosity interlinkage on the grain edges, irradiation-induced recrystallization (grain subdivision), and irradiation-induced crystallization. Bubble-size distributions are calculated as a function of fuel morphology and microstructure, as is the fuel swelling and gas release. DART incorporates algorithms for calculating the densities of bubbles in each of a number of bubble-size classes. Each bubble-size class is characterized by an average number of atoms per bubble, the value of which differs from that of the preceding size class by a constant multiplier. The number of size classes is a variable that is determined dynamically during a computer run. Changes in the bubble-size distribution, caused by bubble coalescence and irradiation-induced re–solution, for example, are determined by solving a large number of integral/differential equations for each time-step. Solutions are carried out for intragranular bubbles, bubbles along dislocations, and intergranular bubbles (bubbles on grain faces and edges). DART utilizes an iterative solution of a relatively large number of coupled equations.

During irradiation, fuel rods increase in diameter, and fuel plates and tubes increase in thickness as a result of swelling of the fuel core. The swelling is a direct result of the accumulation of fission product elements in the fuel. Although this accumulation is, to the first order, directly proportional to the burnup of the fissionable uranium, the resultant swelling is also affected by several microstructural changes that occur in the fuel core during irradiation.

An important factor in reducing the overall amount of net swelling is radiation-enhanced sintering of fabrication voids. In U_3O_8, this effect was first demonstrated by Reinke [2] and was later confirmed by an experiment of Martin et al. [3] in which U_3O_8 dispersion fuel made with depleted uranium was irradiated. The fabrication voids within the U_3O_8 particles, as well as cracks and gaps resulting from fabrication, sintered to spherical cavities after irradiation. It is well established that an increase in dispersant loading also increases the number of fabrication voids. Inasmuch as a substantial fraction of the sintered porosity can be taken up by the swelling fuel, a large volume of fabrication voids can substantially reduce the net swelling.

The DART mechanical analysis, based on the work of Blake [4], addresses the mechanical behavior of both dispersion fuel plates and fuel rods. The model examines a system of spherical fuel particles surrounded by a large spherical shell of matrix material bonded to an outer shell of aluminum cladding. The approach treats the inner sphere as a mechanically deforming body and the spherical shell as perfectly plastic. The DART swelling models provide the driving force for mechanical deformation.

DART does not currently model the thermal performance of the fuel element (aside from the calculation of the thermal conductivity of the dispersion material). Thus, fuel temperature and linear power are required input into the analysis. In a fully coupled model, the calculation of fuel deformation and thermal conductivity is interactive with the thermal analysis.

The DART model includes several assumptions. Among these is the assumption that no swelling of the aluminum matrix is assumed to occur during reactor operation. This assumption is based on the relative swelling rates of the aluminum matrix and the fuel. From these swelling rates, it can be shown that fuel swelling is several orders of magnitude greater than aluminum matrix swelling. Inclusion of aluminum matrix swelling would lead to a slight increase in predicted rod diameter or plate thickness.

The fuel particles are assumed to be identical in size and to have a uniform spherical shape. The size of actual fuel particles varies and their shape is irregular. However, irregular particle shapes are difficult to handle mathematically, and because the orientation of the particles is random, an assumption of uniform overall behavior seems reasonable. In addition, particle-particle interactions are ignored. Including particle-particle interactions will results in a greater degree of swelling than predicted by the model.

No change in aluminum yield stress with respect to fluence is assumed. Using the usual time-dependent deformation methodology, we did not include the effects of the creep of the fuel and matrix. These phenomena are modeled by including a factor that multiplies the aluminum yield strength. This factor differs, depending on whether the fuel element is in a plate/tube or a rod geometry.

In addition to uncertainties involving model assumptions, various uncertainties exist in the experimental data. Physical measurements are subject to errors induced by oxide layers. Measurements are made at various points on the plate or rod to yield an overall thickness and/or diameter measurement, which is an average and is subject to error. Measurement of fabricated porosity is subject to uncertainties. Likewise, it is difficult to accurately measure

matrix dimensions after fabrication. Actual interface conditions between both fuel particles and matrix, and between the matrix and the cladding are not precisely known, and are presumably not orderly and homogeneous as assumed in the model. All of these uncertainties will contribute to deviations between model predictions and experimental data.

This User's Guide includes and describes a typical DART input file, a dictionary of variables in COMMON/PROG/PROG(250), and a typical DART output file in Appendixes A-C, respectively.

2 DART Theory of Fission Gas Behavior in Crystalline Fuel

The DART code predicts atomic and bubble behavior of fission gas in aluminum dispersion fuels under steady-state and transient conditions. Included are models that assess the effects of fission product generation, atomic migration, bubble nucleation and re-solution, bubble migration and coalescence, channel formation on grain faces, porosity interlinkage on grain edges, the existence of a fixed density of nodes that are identified as grain edge corners or triple points, and grain growth/grain boundary sweeping on both the amount of released fission products and on their distribution within the fuel. DART solves a set of coupled nonlinear differential equations for the intra- and intergranular concentrations of fission-product atoms and gas bubbles of the form

$$\frac{dC_i^\alpha}{dt} = -a_i^\alpha C_i^\alpha C_i^\alpha - b_i^\alpha C_i^\alpha + e_i^\alpha \quad (i = 1, \ldots, N;\ \alpha = 1,2,3,4), \tag{1}$$

where C_i^α is the number of α-type bubbles in the i-th size class per unit volume; $\alpha = 1,2,3,4$ represents the lattice, dislocation, grain face, and grain edge distributions, respectively; and the coefficients a_i^α, b_i^α and e_i^α obey functional relationships of the form

$$a_i^\alpha = a_i^\alpha(C_i^\beta),$$

$$b_i^\alpha = b_i^\alpha(C_1^\beta, \ldots, C_{i-1}^\beta, C_{i+1}^\beta, \ldots, C_N^\beta).$$

The variables in Eq. 1 are defined in Table 1. a_i^α represents the rate at which α-type bubbles are lost from (grow out of) the i-th size class because of coalescence with bubbles in that class; b_i^α represents the rate at which α-type bubbles are lost from the i-th size class because of coalescence with bubbles in other size classes, migration out of the structural region, change in bubble type (i.e., by acquiring a different value of α) due to bubble migration processes and re-solution; and e_i^α represents the rate at which bubbles are being added to the i-th size class because

of fission gas generation, bubble nucleation, bubble growth resulting from bubble coalescence, migration processes, and bubble shrinkage due to gas atom re-solution.

The bubbles are classified by an average size, where size is defined in terms of the number of gas atoms per bubble. This method of bubble grouping significantly reduces the number of equations needed to describe the bubble size distributions. The bubble classes are ordered so that the first class refers to bubbles that contain only one gas atom. If S_i denotes the average number of atoms per bubble for bubbles in the i-th class (henceforth called I bubbles), then the bubble size classes are defined by

$$S_i = mS_{i-1}, \tag{2}$$

where the integer $m \geq 0.5 + \sqrt{1.25}$, $i \geq 2$, and $S_1 = 1$. The i = 1 class is assumed to consist of a single gas atom associated with one or more vacancies or vacancy clusters. In general, the rate of coalescence Γ_{ij} of i bubbles with j bubbles is given by

$$\Gamma_{ij} = P_{ij} C_i^{\alpha} C_j^{\alpha}, \tag{3}$$

where P_{ij} is the probability in $m^3 s^{-1}$ of an i bubble coalescing with a j bubble. For i = j, Γ_{ij} becomes

$$\Gamma_{ii} = \frac{1}{2} P_{ii} C_i^{\alpha} C_i^{\alpha} \tag{4}$$

so that each pairwise coalescence is counted only once.

Coalescence between bubbles results in bubbles growing from one size class to another. The probability that a coalescence between an i bubble and a j bubble will result in a k bubble is given by the array T_{ijk}. The number of gas atoms involved in one such coalescence is $S_i + S_j$. The array T_{ijk} is defined by three conditions:

1. $\sum_k T_{ijk} = 1$ (the total probability of producing a bubble is unity).

2. $\sum_k T_{ijk} S_k = S_i + S_j$ (the number of gas atoms, on average, is conserved).

3. For a given pair ij, only two of the T_{ijk} array elements are nonzero. These elements correspond to k and k+1, where $S_k \leq S_i + S_j \leq S_{k+1}$.

From these three conditions, it follows that k = i, and

$$T_{ijk} S_k + (1 - T_{ijk}) S_{k+1} = S_i + S_j. \tag{5}$$

Thus, the probability that a coalescence between an i bubble and a j bubble will result in a k bubble is given by

$$T_{ijk} = \frac{S_{k+1} + S_i - S_j}{S_{k+1} - S_k} = 1 - \frac{S_j}{S_{k+1} - S_k}, \tag{6}$$

and the probability that the coalescence will result in a k+1 bubble is given by

$$T_{ijk+1} = \frac{S_i + S_j - S_k}{S_{k+1} - S_k} = \frac{S_j}{S_{k+1} - S_k}. \tag{7}$$

The array T_{ijk} may be considered the probability that an i bubble will become a k bubble as a result of its coalescence with a j bubble. The rate N_{ijk} at which i bubbles become k bubbles is given by

$$N_{ijk} = \sum_{j \le i} \Gamma_{ij} T_{ijk}. \tag{8}$$

The j bubble is assumed to disappear because gas atoms are absorbed into the i bubble. The rate of disappearance χ_j is given by

$$\chi_j = \sum_{j \ge i} \Gamma_{ij}. \tag{9}$$

The rate N_{ik} at which i bubbles become k bubbles, with k = i+1, is reduced by various processes such as the re-solution of gas atoms. Re-solution is the result of collisions (direct and/or indirect) between fission fragments and gas bubbles. From Eqs. 7 and 8,

$$\mathrm{N_{ik}} = \sum_{\mathrm{j \le i}} \Gamma_{\mathrm{ij}} \mathrm{T_{ijk}}$$

$$= \sum_{j \le i} P_{ij} C_i C_j \frac{S_j}{S_k - S_i}$$

$$= \frac{C_i}{S_k - S_i} \sum_{j \le i} P_{ij} C_j S_j. \tag{10}$$

The expression $\sum_{j \le i} P_{ij} C_j S_j$ is the rate at which gas atoms are added to an i bubble. Re-solution causes an i bubble to lose gas atoms at a rate given by $b_i S_i$, where b_i is the probability that a gas atom in an i bubble is redissolved. The reduced N_{ik} becomes

$$N_{ik} = \frac{C_i}{S_k - S_i} \sum_{j \le i} (P_{ij} C_j S_j - b_i S_i). \tag{11}$$

If the expression within the parentheses is negative, then N_{ik} is zero, and $N_{ik'}$, the rate at which i bubbles become i-1 bubbles, with k = i-1, is defined as

$$N_{ik'} = \frac{C_i}{S_i - S_k} \left(b_i S_i - \sum_{j \le i} P_{ij} C_j S_j \right). \tag{12}$$

Equations 11 and 12 are proportional to the probabilities that any particular i bubble will become an i+1 or an i-1 bubble, respectively; the ratio of the probabilities is equal to the ratio of the rates. Clearly, the above definitions of N_{ik} and $N_{ik'}$ are consistent with the conservation of the total number of gas atoms.

The components of the basic equations (i.e., Eq. 1) solved in DART are described below.

2.1 Intragranular Fission Gas and Fission Gas on Dislocations

The flux of gas atoms diffusing to the grain boundaries in a concentration gradient is obtained by solving for the concentration of gas atoms C_g within a spherical grain that satisfies the equation

$$\frac{\partial C_g}{\partial t} = \frac{1}{r^2} \frac{\partial}{\partial r} \left(D_g r^2 \frac{\partial C_g}{\partial r} \right) + \alpha \dot{f}, \tag{13}$$

where D_g is the gas atom diffusion coefficient, $\dot{f}$ is the fission rate, α is the average number of rare-gas atoms produced per fission, and r is the radial distance from the grain center.

In general, Eq. 13 is solved with the boundary conditions

$$C_g = 0 \quad \text{at } t = 0 \qquad \text{for } 0 \le r \le d_g / 2, \tag{14}$$

$$C_g = 0 \quad \text{at } r = d_g / 2 \text{ for } t_0 \le t \le t_0 + \Delta t, \tag{15}$$

$$\frac{\partial C_g}{\partial r} = 0 \quad \text{at } r = 0 \qquad \text{for } t_0 \le t \le t_0 + \Delta t, \tag{16}$$

where Δt is an increment of time.

Table 1. Definition of variables in Eq. 1, $\frac{dC_i^\alpha}{dt} = -a_i^\alpha C_i^\alpha C_i^\alpha - b_i^\alpha C_i^\alpha + e_i^\alpha$

α	i	C_i^α	$a_i^\alpha C_i^\alpha C_i^\alpha$	$b_i^\alpha C_i^\alpha$	e_i^α
1,2	1	Concentration of intragranular gas atoms ($\alpha = 1$), and gas atoms on dislocations ($\alpha = 2$)	Rate of gas atom loss due to gas bubble nucleation	Rate of gas atom loss due to diffusive flow to grain boundaries, grain boundary sweeping, and diffusion into gas bubbles	Rate of gas atom gain due to atom re-solution and fission of uranium nuclei
1,2	2,...,N	Concentrations of intragranular gas bubbles ($\alpha = 1$), and gas bubbles on dislocations ($\alpha = 2$)	Rate of gas bubble loss due to bubble coalescence with bubbles within the same size class	Rate of gas bubble loss due to coalescence with bubbles in other size classes, diffusive flow to grain boundaries ($\alpha = 1$), grain boundary sweeping, and gas atom re-solution	Rate of gas bubble gain due to bubble nucleation and coalescence, and diffusion of gas atoms into bubbles
3	1,...,N	Concentrations of grain face gas atoms ($i = 1$) and gas bubbles ($i > 1$)	Rate of gas loss due to gas bubble nucleation ($i = 1$) and bubble coalescence with bubbles within the same size class ($i > 1$)	Rate of gas bubble loss due to coalescence with bubbles in other size classes, venting to grain edges, and microcracking, and rate of gas atom loss due to capture by gas bubbles	Rate of gas bubble gain due to bubble nucleation and coalescence diffusion of gas atoms into bubbles, and intragranular migration to grain faces
4	1,...,N	Concentrations of grain edge gas atoms ($i = 1$) and gas bubbles ($i > 1$)	Rate of gas loss due to gas bubble nucleation ($i = 1$) and bubble coalescence with bubbles within the same size class ($i > 1$)	Rate of gas bubble loss due to coalescence with bubbles in other size classes, long-range grain edge bubble interconection, and microcracking, and rate of gas atom capture by bubbles	Rate of gas bubble gain due to bubble nucleation and coalescence diffusion of gas atoms into bubbles, and the venting of gas from the grain faces

The concentration of gas atoms in a spherical grain described in Eq. 13 is

$$\frac{1}{r^2}\frac{d}{dr}\left(D_g r^2 \frac{dC_g}{dr}\right) - \frac{C_g}{\delta t} + \frac{C_g^o}{\delta t} + \alpha \dot{f} = 0. \tag{17}$$

Euler's theorem may now be used to obtain a variational principle equivalent to Eq. 17:

$$\delta \int_0^{1/2 d_g} 4\pi \left[\frac{D_g}{2}\left(\frac{dC_g}{dr}\right)^2 + \frac{C_g^2}{2\delta t} - \left(\frac{C_g^o}{\delta t} + \alpha \dot{f}\right) C_g\right] r^2 dr = 0, \tag{18}$$

which assumes that Dirichlet boundary conditions are to be applied. An approximate solution to the problem may now be obtained by choosing a trial function that satisfies the boundary conditions and minimizes the integral in Eq. 18 in terms of free parameters in the function. Many types of trial function could be chosen, but it is easier to work with piecewise functions than global functions. Quadratic functions are attractive because they allow an exact representation of Eq. 13 for long times. To meet the objective of a realistic level of accuracy with a minimum of computer storage and running time, the spherical grain is split into two concentric regions of approximately equal volume, as shown in Fig. 1. In each region, the gas concentration is represented by a quadratic function constrained to have $dC_g/dr = 0$ at $r = 0$. In the outer Region II (Fig. 1), the concentration function is constrained to a value of $C_g = 0$ at $r = d_g/2$. The two functions are also constrained to be continuous at the common boundary of the two regions. This leaves three free parameters. Matthews and Wood [5] chose these

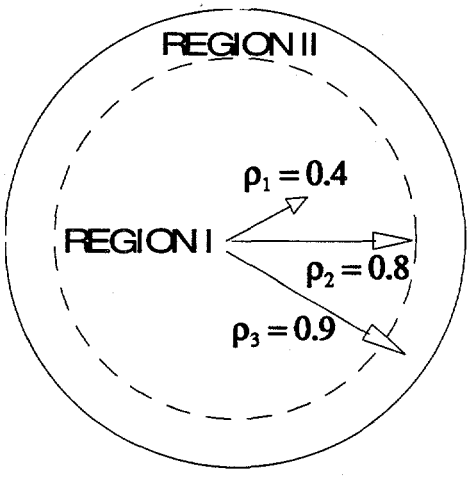

Fig. 1. Configuration of two–zone model.

to be the concentrations C_1^g, C_2^g, and C_3^g, respectively, for the radius ratios $r_1 = 0.4$, $r_2 = 0.8$, and $r_3 = 0.9$, where $r = 2r/d_g$. These positions are the midpoint radi of Region I, the boundary between the regions, and the midpoint radius of Region II, respectively. Thus, the trial functions are as follows:

For Region I,

$$C_g = C_1^g\left(0.64-\rho^2\right)/0.48+\left(\rho^2-0.16\right)/0.48. \tag{19}$$

For Region II,

$$C_g = C_1^g\left(0.64-\rho^2\right)/0.48+\left(\rho^2-0.16\right)/0.48. \tag{20}$$

Eqs. 19 and 20 are substituted for C_g in Eq. 18 and an extremum is found by differentiating with respect to C_1^g, C_2^g, and C_3^g in turn. The following three linear equations are thus obtained:

$$\begin{aligned}&\left(q_1 D_g/d_g^2+q_{2/\delta t}\right)C_1^g+\left(q_3 D_g/d_g^2+q_{4/\delta t}\right)C_2^g\\&=K_g q_5+\left(C_1^0 q_2+C_2^0 q_4\right)/\delta,\end{aligned} \tag{21a}$$

$$\begin{aligned}&\left(q_3 D_g/d_g^2+q_{4/\delta t}\right)C_1^g+\left(q_2 D_g/d_g^2+q_{7/\delta t}\right)C_2^g+\left(qD_g/d_g^2+q_{9/\delta t}\right)C_3^g\\&=K_g q_{10}+\left(C_1^0 q_4+C_2^0 q_7+C_3^0 q_9\right)/\delta t,\end{aligned} \tag{21b}$$

$$\begin{aligned}&\left(q_9 D_g/d_g^2+q_{9/\delta t}\right)C_2^g+\left(q_{11} D_g/d_g^2+q_{12/\delta t}\right)C_3^g\\&=K_g q_{13}+\left(C_2^0 q_9+C_3^0 q_{12}\right)/\delta t,\end{aligned} \tag{21c}$$

where C_1^0, C_2^0, and C_3^0 are the values of the concentrations at the evaluation points at the start of the time increment. The various q coefficients are integrals, which, when directly evaluated, are, to four figures,

$q_1 = 4.552$, $q_2 = 0.06935$, $q_3 = -4.552$,

$q_4 = 0.02167$, $q_5 = 0.09102$, $q_6 = 37.78$,

$q_7 = 0.07615$, $q_8 = -38.72$, $q_9 = 0.008456$,

$q_{10} = 0.01008$, $q_{11} = 87.04$, $q_{12} = 0.08656$,

$q_{13} = 0.1083$.

Equations 21a-c can be directly solved to obtain concentrations C_1, C_2, and C_3 as follows:

$$C_1^g = \frac{X_1 - F_2 C_2^g}{F_1}, \tag{22a}$$

$$C_2^g = \frac{\frac{F_2}{F_1} X_1 + \frac{F_4}{F_5} X_3 - X_2}{\frac{F_2}{F_1} F_2 + \frac{F_4}{F_5} F_4 - F_3}, \tag{22b}$$

and

$$C_3^g = (X_3 - F_4 C_2^g) / F_5, \tag{22c}$$

where

$$F_1 = q_1 D_g / d_g^2 + q_2 / \delta t,$$
$$F_2 = q_3 D_g / d_g^2 + q_4 / \delta t,$$
$$F_3 = q_6 D_g / d_g^2 + q_7 / \delta t,$$
$$F_4 = q_8 D_g / d_g^2 + q_9 / \delta t,$$
$$F_5 = q_{11} D_g / d_g^2 + q_{12} / \delta t,$$
$$X_1 = \dot{f} q_5 + \left(C_1^0 q_2 + C_2^0 q_4\right) / \delta t,$$
$$X_2 = \dot{f} q_{10} + \left(C_1^0 q_4 + C_2^0 q_7 + C_3^0 q_9\right) / \delta t,$$
$$X_3 = \dot{f} q_{13} + \left(C_2^0 q_9 + C_3^0 q_{12}\right) / \delta t.$$

The flux of gas atoms to the boundary (in units of atoms/m^3/s) is given by

$$J = -\frac{6 D_g}{dg} \frac{\partial C}{\partial r}\Big|_{r=d_g/2}, \tag{23}$$

or

$$J = -\frac{D_g}{d_g^2}\left(-60 C_2^g + 240 C_3^g\right). \tag{24}$$

For proper coupling of the diffusive flow process with other processes that affect fission gas behavior, (e.g., gas atom re–solution, gas atom trapping by bubbles, and gas bubble nucleation and coalescence) information about the average concentration of fission gas within the grain is required.

Matthews and Woods [5] determined that the best expression for the average concentration within the grains, $\overline{C}_g$, is given by

$$\overline{C}_g = 0.2876C_i^g + 0.2176C_2^g + 0.4261C_3^g. \tag{25}$$

At the end of an iteration, the concentrations C_i^g, C_2^g, and C_3^g in Eq. 25 are scaled by imposing the condition that the average concentration calculated with Eq. 25 is equal to the average concentration calculated with Eq. 1, i.e., that the modified C_i^g, C_2^g, and C_3^g then become the initial values of the concentrations (i.e., C_1^0, C_2^0 and C_3^0) that are to be used for the next iteration. The diffusive flow of fission gas bubbles is treated in a manner analogous to that for fission gas atoms, but with $\dot{f} = 0$ in Eq. 13. This method of coupling diffusive flow with other processes that affect fission gas behavior (e.g., gas atom re–solution, gas atom trapping by gas bubbles, gas nucleation and coalescence) is computationally efficient and has been benchmarked against various analytical solutions.

Re-solution causes an i bubble to lose gas atoms at a rate given by $b_i S_i$ (see Eq. 11), where the rate at which gas atoms are ejected from the bubble, b_i, is calculated under the assumption that gas atom re–solution from a spherical bubble is isotropic and proceeds by the ejection of single gas atoms. Thus,

$$b_i = \frac{3b_o \dot{f}}{R_i^3}\int_{R_i-\lambda}^{R_i}\left(\frac{1+\cos\theta_i}{2}\right)r^2 dr, \tag{26}$$

where R_i is the radius of an i bubble and $\cos\theta_i = \left(R_i^2 - \lambda^2 - r^2\right)/2r\lambda$. A straightforward integration of Eq. 26 results in

$$b_i = \frac{3b_o f}{R_i^3}\left\{R_i^2\left[\frac{R_i}{6} + \frac{R_i^2}{16\lambda} + \frac{1}{8}\left(\lambda - \frac{R_i}{\lambda}\right)\right] - \left(R_i - \lambda\right)^2\left[\frac{R_i - \lambda}{6} + \frac{\left(R_i - \lambda\right)^2}{16\lambda} + \frac{1}{8}\left(\lambda - \frac{R_i}{\lambda}\right)\right]\right\}, \tag{27}$$

where λ is the average distance an ejected atom travels, b_o is a measurable property of the material, and δ is a measure of the "strength" of gas atom re–solution from grain boundary bubbles.

The atom fission gas diffuses by random migration to dislocations at a rate governed by

$$R_i^d = \frac{2\pi D_g \rho C_g}{\ln(r_c / r_i)}, \tag{28}$$

where ρ is the dislocation density (mm/mm^3), r_i is the mathematical radius of a single gas atom, and r_c is the radius of the cylindrical capture volume; i.e.,

$$(\pi r_c^2)\rho = 1. \tag{29}$$

Once the fission gas is pinned to dislocations, the gas can coalesce with both lattice and dislocation bubbles (re-solution causes gas atoms to be knocked back into the lattice), and the gas can be pulled back into the lattice by the force of a temperature gradient if the fission-gas bubbles grow beyond a specified critical size. In the lattice, the probability, P_{ij} of an I bubble coalescing with a j bubble by random motion is given by

$$P_{ij} = 4\pi(R_i + R_j)(D_i + D_j), \tag{30}$$

Coalescence probabilities for bubbles on dislocations can be derived based on a solution of the one-dimensional, time-independent diffusion equation and are given by

$$P_{ij}^R = (D_i^d + D_j^d) / \sqrt{\rho} \tag{31}$$

where D_i^d is the average dislocation i-bubble diffusion coefficient. The coalescence probabilities for dislocation bubbles coalescing with lattice bubbles is given by Eq. 30 with the diffusivity of the dislocation bubble equal to zero; i.e., the bubble on the dislocation is assumed pinned and immobile.

2.2 Intergranular Fission Gas: Grain Faces

DART calculates fission gas saturation in the grain face by directly addressing the calculated distribution of fission gas bubble sizes. The projected areal coverage of the grain face by these bubbles, per unit volume, is given by

$$A_f = \pi f_f(\theta) \sum_i (R_i^f)^2 C_i^f, \tag{32}$$

where $f_f(\theta)$ is a geometrical factor that accounts for the lenticular shape of the grain face bubbles, and R_i^f is the radius of a grain face i bubble. If the gas is assumed to be made up of equal, closely packed, touching bubbles, the maximum areal coverage per unit area of grain face is $A_f^* = 0.909$. (Under conditions where this assumption is

not valid, i.e., $A_f^* < 0.909$, the DART code utilizes a nominal value of $A_f^* = 0.5$). Grain face saturation (i.e., the initiation of gas channel formation) occurs when

$$A_f \geq A_f^* S_v^{\alpha\alpha}, \tag{33}$$

where $S_v^{\alpha\alpha}$ is the grain face area per unit volume.

Equations 32 and 33 do not account for local variations in fuel microstructure. To include these effects in the calculation of grain face channel formation, it is assumed that the local variations in fuel microstructure can be represented by the width σ_f of a distribution of A_f (Eq. 32) such that the probability fraction of grain face channel interlinkage P_{A_f} is given by

$$P_{A_f} = \frac{1}{\sigma_f \sqrt{2\pi}} \int_{x=A_F^* S_v^{\alpha\alpha}} \exp\left[\left(-x - A_f\right)^2 / 2\sigma_f^2\right] dx. \tag{34}$$

The width of the distribution in Eq. 34 is a function of erratic structural parameters, depending on local fuel condition and heterogeneity; in principle, it can be determined experimentally.

2.3 Intergranular Fission Gas: Grain Edges

The DART model for calculating the probability of long–range grain edge tunnel interconnection is based on the assumption that long–range interconnection is a function of the swelling of grain edge bubbles. This assumption is supported by experiment [6] and theory [7]. To account for local fluctuations in fuel microstructure and gas bubble morphology, the grain edge/porosity interlinkage fraction P_I is assumed to be a statistical distribution around an average value of the grain edge swelling B_{vedge}, thus,

$$P_I = \frac{1}{\sigma_e \sqrt{2\pi}} \int_{x=B_{vcrit}}^{\infty} \exp\left[-\left(x - B_{vedge} - B_{vpor}\right)^2 / 2\sigma_e^2\right] dx, \tag{35}$$

where $B_{vedge} = \frac{4\pi\sigma_e}{3} \sum_{i=1}^{n\max} \left(R_i^e\right)^3 C_i^e$ and σ_e is the width of a distribution of P_I that accounts for local fluctuations in fuel microstructure and gas bubble morphology (e.g., the ellipsoidal shape of grain edge bubbles). The value of the grain edge swelling at which long–range interconnection would take place if the fuel microstructure and gas bubble morphology were homogeneous is $B_{vcrit} = 0.05$; the fractional as-fabricated grain edge porosity is B_{vpor}. Retained grain edge fission gas causes the deformation of grain edges (i.e., grain edge swelling of fission gas bubbles), and subsequent increased long-range interconnections of grain edge tunnels. This interconnection of

grain edge tunnels provides the pathways for fission gas release to triple points. The DART intergranular swelling model has been benchmarked against experimental results [8].

2.4 Intergranular Fission Gas: Dead-End Nodes

A striking aspect of the observed bubble population is that it is uniformly distributed and noninteracting. As discussed in Section 6 (see Fig. 7), the total number of bubbles in the second (large bubble) peak of the measured bimodal distribution remains relatively constant for all of the examined samples.

It is assume here that the large bubble population inhabits fixed sites. These sites are formed upon grain recrystallization and are associated with nodes that are formed by the intersection of grain edges within the subgrain boundary structure. Upon intersection, fission gas that collects along grain edges vents to these nodes, where it is trapped. Gas bubbles at these "dead–end" nodes grow as they continue to collect additional gas. If the grains are assumed to be cubes, and the dead–end nodes are taken to be grain corners formed by the intersection of six grain edges, the number of nodes per cubic centimeter C_N is given by the inverse of the cube root of the grain diameter, i.e., $C_N = d_g^{-1/3}$.

2.5 Fission Gas Release

Contributions to fission gas release come from the venting of grain face gas into interconnected grain edge tunnels, and from the venting of previously trapped grain edge gas through newly interconnected tunnels. The fission gas release rate (atoms m^{-3} s^{-1}) is given by

$$\frac{\mathrm{dfgr}}{\mathrm{dt}} = \sum_i P_{A_f} C_i^f S_i P_I / h + \sum_i \frac{dP_I}{dt} C_i^e S_i \,. \tag{36}$$

For a multinode calculation, the various gas release contributions from each individual node, given by Eq. 37, are summed up to obtain the total gas released during the time step h.

2.6 Options for Calculating Bubble Radii

Whereas intragranular bubbles are assumed to be spherical, the intergranular gas bubbles are assumed to be lenticular on the grain faces and ellipsoidal along the grain edges. Grain corner bubbles are assumed to be spherical. The diffusional growth of nonequilibrium intragranular bubbles is based on an analysis by Gruber [9] . The rate of change of the lattice i bubble radius is given by

$$\frac{d\mathrm{R}_i^l}{dt} = \frac{D_u}{\mathrm{R}_i^l}\left[1 - \exp\left(P_i^l - P_h - \frac{2\gamma}{\mathrm{R}_i^l}\right)\frac{\Omega}{kT}\right], \tag{37}$$

where D_u is the vacancy diffusion coefficient, Ω is the atomic volume, kT is the thermal energy, P_i^l is the internal gas pressure in the lattice i bubble, P_h is the external hydrostatic pressure, and γ is the surface energy. For ease in calculating, an approximation is utilized for the relaxation time; it is of the form

$$R_i^l = R_i^l(0) + \left[R_i^{l,eq} - R_i^l(0)\right]\left(1 - e^{-t/\tau_i^l}\right), \tag{38}$$

where τ_i^l is defined by the initial growth rate calculated with Eq. 37. In DART, $R_i^{l,eq}$ is obtained by solving an approximate equation of state simultaneously with the capillarity relationship.

The diffusional growth of nonequilibrium intergranular bubbles is taken from Speight and Beere [10]. Accordingly, the rate of volume change of grain boundary pores is given by

$$\frac{dV_i}{dt} = \frac{2D_{gb}W}{kTL}\left(P_i - \frac{2\gamma}{\rho_i} - P_h\right), \tag{39}$$

where V_i is the volume of the pore, ρ_i is the radius of curvature of the pore, L is a function of the fraction of the grain boundary area occupied by pores, D_{gb} is the grain boundary diffusion coefficient, and W is the boundary thickness. DART provides three choices for the Xe equation of state: Van der Waals, Harrison's extrapolation, and a perturbed hard-sphere model. The perturbed hard-sphere model also provides an equation of state for Kr and Ar.

3 DART Model for Irradiation-Induced Changes in Thermal Conductivity of Dispersion Fuel

The DART thermal conductivity model accounts for the dependence of thermal conductivity on both as–fabricated and irradiation-induced porosity. For dispersion fuels, two distinct classes of pores exist, namely, fission gas microbubbles generated within the U_3Si_2 fuel particles and as–fabricated voids contained within the aluminum matrix. Where pore geometry and physical properties are of prime importance, the analytical treatment of such pores is, however, similar. Pore geometry is defined by its size, shape, and orientation with respect to the direction of heat flow. Physical properties of importance are the emissivity of the pore surface and the thermal conductivity of the gas trapped within the pore. Figure 2 can be used to establish a geometric relationship for the thermal conductivity of a solid material containing a gas pore. The unit cell can be represented as a cube of solid material surrounding a spherical pore. The most important variable considered, and the one that appears in all theoretical models [11-13], is the volume porosity P, defined as

$$P = \frac{\text{Pore Volume}}{\text{Pore Volume} + \text{Volume of Solid}}. \tag{40}$$

Assuming that heat flows in the y direction only, the effective thermal conductivity k_e of the unit cell in the y direction is given by the expression

$$k_e = P_c k_{ap} + (1 - P_c) k_s, \tag{41}$$

where k_e = effective thermal conductivity, k_S = thermal conductivity of solid material, k_{ap} = apparent thermal conductivity of the pore tube, and P_c is the fraction of the cross–sectional area of the x–z face of the unit cell that is occupied by the pore. To assess the conductance over the path length in the y direction, we define a pore tube length L that considers both the pore and the solid material that occupies the remaining tube length. The apparent thermal conductance of the pore tube (pore plus solid material in the path length) can be evaluated by considering the thermal resistance of these two regions; it can be expressed as

$$\frac{1}{k_{ap}} = \frac{P_L}{k_p} + \frac{1 - P_L}{k_s}, \tag{42}$$

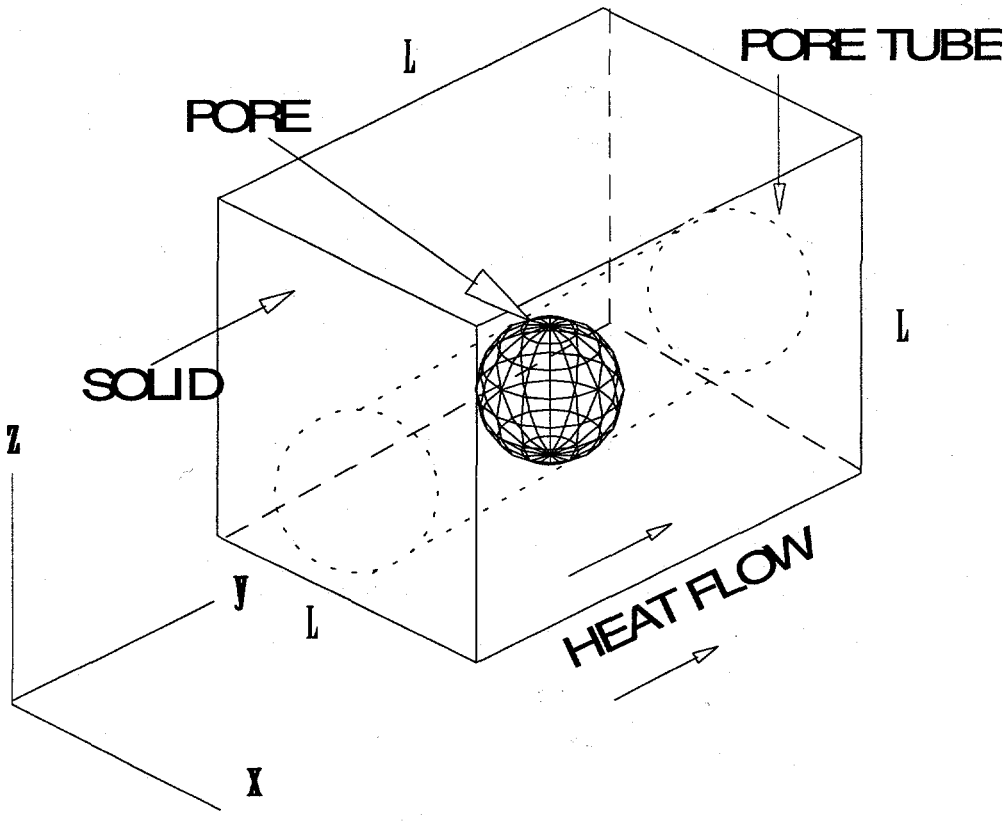

Fig. 2. Representation of unit cell of a porous body for which effective thermal conductivity is assessed.

where P_L = fractional length of pore and k_p = effective pore thermal (gas conductivity plus radiation). By eliminating k_{ap} between Eqs. 41 and 42, we obtain the following expression [14 ,15]:

$$\frac{k_e}{k_s} = 1 - P_c\left(1 - \frac{k_p/k_s}{P_L}\right). \tag{43}$$

In Eq. 43, the effect of volume porosity on thermal conductance is contained in the quantities P_C and P_L. For the case of fission gas bubbles within U_3Si_2 fuel particles, it is assumed that the bubbles are spherical, with a radius R, and uniformly spaced in the material. Under these assumptions, the following expressions apply:

$$P_c = \pi R_g^2 / l_g^2 = \pi\phi^2 R_g^2(\rho_g)^{2/3}, \tag{44}$$

$$P_L = 2R_g / l_g = 2\phi R_g(\rho_g)^{1/3}, \tag{45}$$

where ρ_g is the bubble density (bubbles/cc), l_g is the interbubble spacing, and ϕ is a geometric factor that relates the average interbubble spacing to the bubble density, i.e., $l_g = \phi\,\rho_g^{-1/3}$. For uniformly spaced gas bubbles, φ = 1.26.

The thermal conductivity of a pore filled with gas is given by the expression [16]

$$k_p = k_g + 4\varepsilon\,\sigma R T^3, \tag{46}$$

where k_g = bulk thermal conductivity of the gas, ε = emissivity, σ = Stefan–Boltzmann constant, and T = temperature.

For the size pores and range of temperatures under consideration, the second term in Eq. 46, representing radiative heat transfer, can be neglected. Thus, Eq. 43, when applied to gas bubbles, reduces to the form

$$k_e^g / k_f = 1 - \left[\pi R_g^2(\rho_g)^{2/3}\right]\left[1 - k_g / \left(2k_f R_g \rho_g^{1/3}\right)\right], \tag{47}$$

where k_e^g = effective thermal conductivity of fuel particles that contain fission gas, and k_f = thermal conductivity of bulk U_3Si_2.

Equation 47 can be written in the form

$$k_e^g / k_f = 1 - \pi(R_g / l_g)^2 + \frac{\pi k_g}{2k_f}(R_g / l_g), \tag{48}$$

where the ratio of the bubble radius R_g to interbubble spacing l_g can be expressed as

$R_g / l_g = \phi^{-1} R_g \rho_g^{1/3} = \phi^{-1} \sum_{\alpha} \sum_{i} R_i^{\alpha} \left(C_i^{\alpha} \right)^{1/3}$, where α sums over the various morphological fuel regions (e.g., bulk, dislocations, faces, and edges) and i sums over the bubble size distribution.

The geometric condition for bubble interconnection is given by $l_g = 2R_g$. Equations 47 and 48 represent expressions for k_e^g / k_f in terms of average properties of the fission gas bubble size distribution that evolves within the U_3Si_2 fuel particles during irradiation. The expression for k_g that is used to evaluate Eqs. 47 and 48, as given in Ref. 13, is

$$k_g(\text{xenon}) = \left(4.0288 \text{x} 10^5\right) T^{0.872} \text{ (W / mK)}. \tag{49}$$

To include the effects of both as–fabricated and irradiation-induced porosity on the thermal conductivity of U_3Si_2 particles dispersed in an aluminum matrix, successive applications of a mixing formula of the form given by Eq. 48 have been utilized. For example, the thermal conductivity of aluminum containing a dispersion of U_3Si_2 particles (i.e., containing fission gas) with no as–fabricated porosity is given by

$$k_e^p = 1 - \left(\pi R_f^2 \rho_f^{2/3}\right)\left[1 - k_e^g / \left(2 k_{al} R_f \rho_f^{1/3}\right)\right], \tag{50}$$

where k_e^p = effective thermal conductivity of dispersion with no as–fabricated porosity, R_f = radius of particle, k_e^g = effective thermal conductivity of U_3Si_2 particles containing fission gas (given by Eq. 48), ρ_f = density of U_3Si_2 particles, and k_{al} = thermal conductivity of pure aluminum.

If as–fabricated porosity is now introduced into the material,

$$\frac{k_e^m}{k_e^p} = 1 - \pi R_p^2 \rho_p^{2/3}, \tag{51}$$

where k_e^m = thermal conductivity of dispersion, containing both as–fabricated and irradiation-induced porosity; R_p = radius of as–fabricated pores; and ρ_p = density of as–fabricated porosity.

In deriving Eq. 51, the thermal conductivity of an as–fabricated pore has been assumed to be zero. For particles dispersed in aluminum and for the distribution of as-fabricated porosity, $\varphi = 1$. Utilizing Eqs. 50 and 51, we can express k_e^m as

$$\begin{aligned} k_e^m = k_{al}\Big[& Z_1 + Z_2 F_f^{2/3} + Z_3 \left(k_e^g / k_{al}\right) F_f^{1/3} \left(1 + Z_2 F_p^{2/3}\right) \\ & + Z_2 F_p^{2/3} + Z_4 \left(F_f F_p\right)^{2/3} \Big], \end{aligned} \tag{52}$$

where the fuel and pore volume fractions F_f and F_p are given by

$$F_f = \frac{4}{3}\pi R_f^3 \rho_f, \tag{53}$$

$$F_p = \frac{4}{3}\pi R_p^3 \rho_p, \tag{54}$$

and where Z_1–Z_4 are constants:

$$Z_1 = 1$$
$$Z_2 = -\pi(3/4\pi)^{2/3}$$
$$Z_3 = \pi/2(3/4\pi)^{1/3}$$
$$Z_4 = \pi^2(3/4\pi)^{4/3}$$

Implicit in the derivation of Eq. 52 is the assumption of a homogeneous distribution of spherical particles (i.e., fission gas, as–fabricated pores, U_3Si_2 particles) within the respective host materials. To quantify the effects of deviations from this idealized geometry, such as nonspherical pores and particles, as–fabricated and irradiation-induced pores preferentially distributed along the particle/matrix interface (e.g., fission gas released from the grain interior can collect at the particle/matrix interface), the constant Z_4 was determined by regression analysis, based on unirradiated dispersion fuel data from Ref. 17, shown in Table 2 to be:

$Z_4 = 0.6521.$

Equation 52 is valid as long as the matrix aluminum is the continuous media. An analogous expression to Eq. 52 can be derived for cases where the fuel is the continuous media. This case is not considered here. In addition, Z_4 has been determined based on a comparison with plate-fuel conductivity measurements in the transverse (thickness) direction. As such, Eq. 52 is valid for thermal conductivity calculations in the transverse direction only. An extension of Eq. 52 to conductivity calculations in the longitudinal direction can be obtained by an appropriate utilization of measured anisoptropy in U3Si2 ground-powder-based fuel plates.

The results of this analysis are shown in Table 2 and Figs. 3 and 4. Figure 3 shows the results of the regression analysis performed with Eq. 52 and with the data listed in Table 2. Figure 4 shows the thermal conductivity data and the results calculated for thermal conductivity with Eq. 52, plotted against the volume fraction of fuel plus voids. Figure 5 shows the DART–calculated thermal conductivity for U_3Si fuel as a function of irradiation–induced porosity, and measured values [18] for irradiated and subsequently annealed bulk U_3Si. The calculations shown in Fig. 5 were made utilizing ϕ=1.33, or a distribution closely approximating a distribution of equally spaced bubbles (given by ϕ=1.26). The effect of swelling porosity on the thermal conductivity of irradiated U_3Si was deduced from electrical conductivity measurements on samples with pore volume fractions of 0.01-0.27. The

Table 2. Results of regression analysis from Eq. 52 and data from Ref. 17

#	k_e^m (W/mK)	F_f (%)	F_p (%)	k_e^g / k_{al}	k_e^m / k_{al}	
					Data	Model
01	70.9	32.5	6.9	0.06607	0.31652	0.3122
02	75.5	34.0	6.9	0.06607	0.33705	0.2969
03	33.0	39.7	10.5	0.06607	0.14732	0.1908
04	34.0	38.4	11.6	0.06607	0.15179	0.1890
05	39.0	38.0	12.4	0.06607	0.17411	0.1828
06	12.0	49.9	18.4	0.06607	0.05357	0.0121
07	181.0	13.7	1.9	0.06607	0.80804	0.6353
08	78.0	32.3	6.0	0.06607	0.34821	0.3286
09	40.0	39.4	9.2	0.06607	0.17857	0.2108
10	48.0	37.0	9.3	0.06607	0.21429	0.2325
11	40.0	39.1	9.5	0.06607	0.17857	0.2097
12	59.0	46.4	4.0	0.06607	0.26339	0.2225
13	59.0	46.4	4.0	0.06607	0.26339	0.2225
14	13.9	46.4	15.4	0.06607	0.06205	0.0729
15	14.5	46.9	15.4	0.06607	0.06473	0.0686

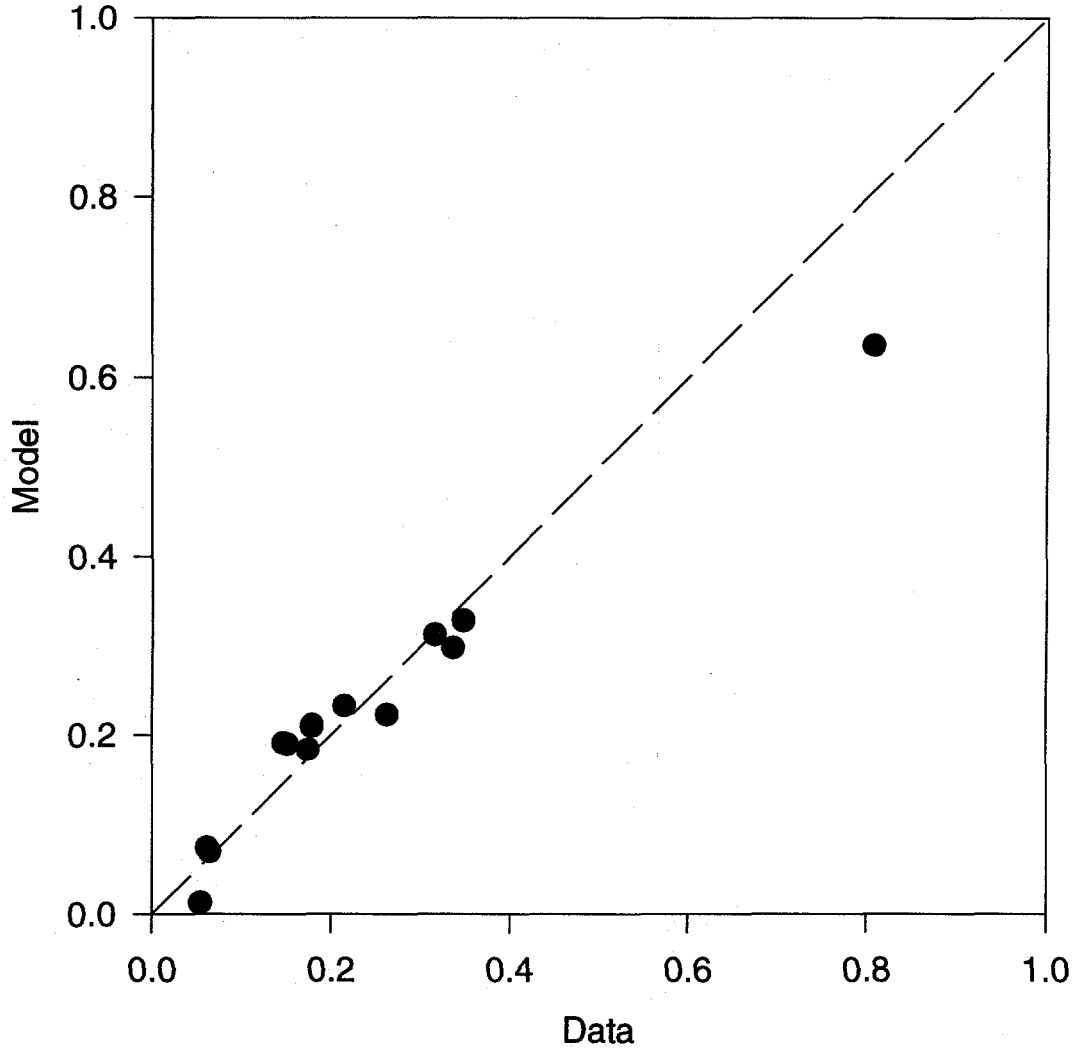

Fig. 3. Results of regression analysis obtained from Eq. 52 and from data in Table 2

authors of Ref. 18 state that the porosity in the irradiated and annealed U_3Si consists of fission gas as compared with predominantly empty voids in the irradiated-only case. As shown in Fig. 5, the DART-calculated change in thermal conductivity agrees reasonably well with the measured values.

Equation 52 provides a physically based expression for the evolution of thermal conductivity in irradiated dispersion fuels. As such, even though the geometric constant Z_4 was determined from unirradiated data, Eq. 52 embodies physically realistic functional dependencies, e.g., the dependence of thermal conductivity on fuel and matrix volume fractions and on as–fabricated and irradiation-induced porosity, which allow for a reasonable extrapolation to irradiated materials.

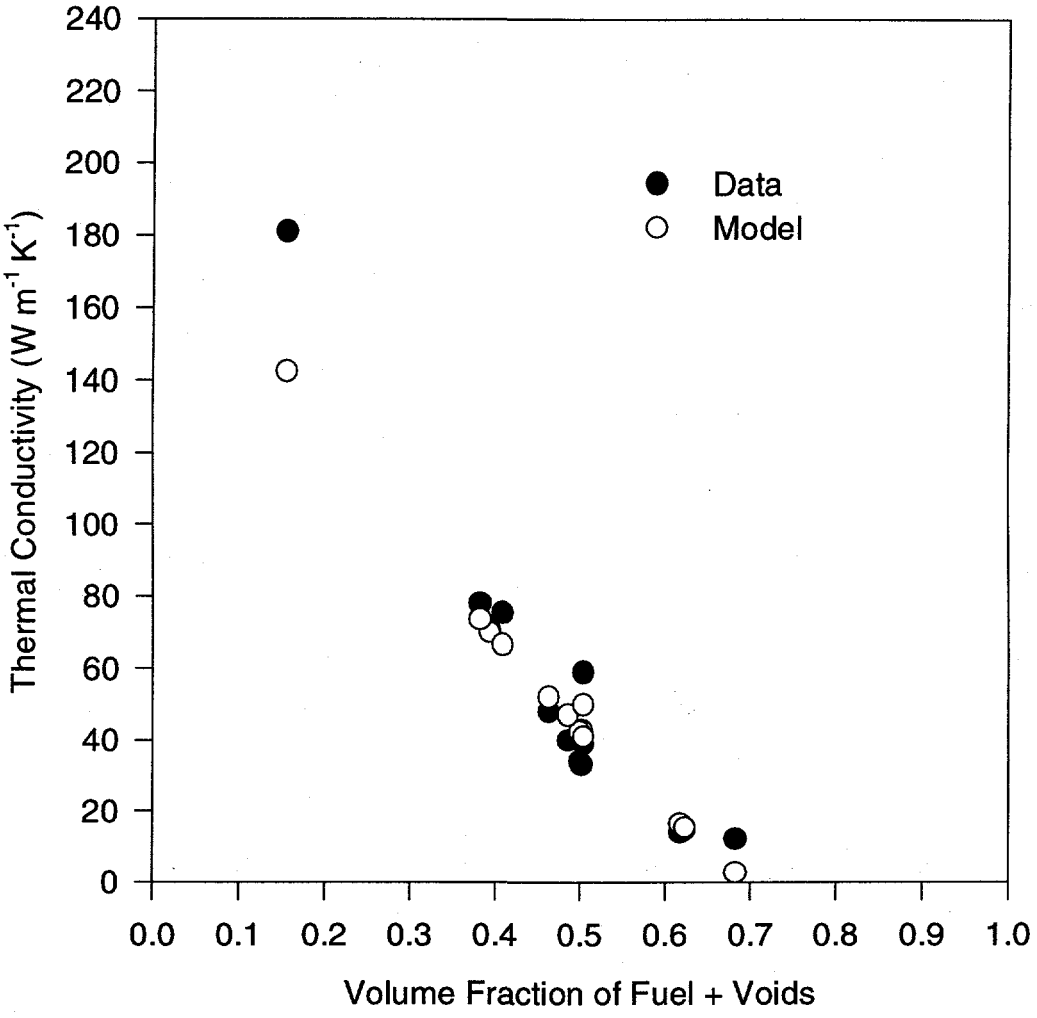

Fig. 4. Thermal conductivity obtained from Eq. 52 and from data listed in Table 2, as a function of volume fraction of fuel + voids

4 DART Model for Mechanical Behavior of Aluminum Dispersion Fuels

During irradiation, the fuel rods, plates, and tubes increase in diameter (thickness) as a result of swelling of the fuel core. The swelling is a direct result of the accumulation of fission-product elements in the fuel. Although this accumulation is, in the first order, directly proportional to the burnup of ^{235}U, the resultant swelling is also

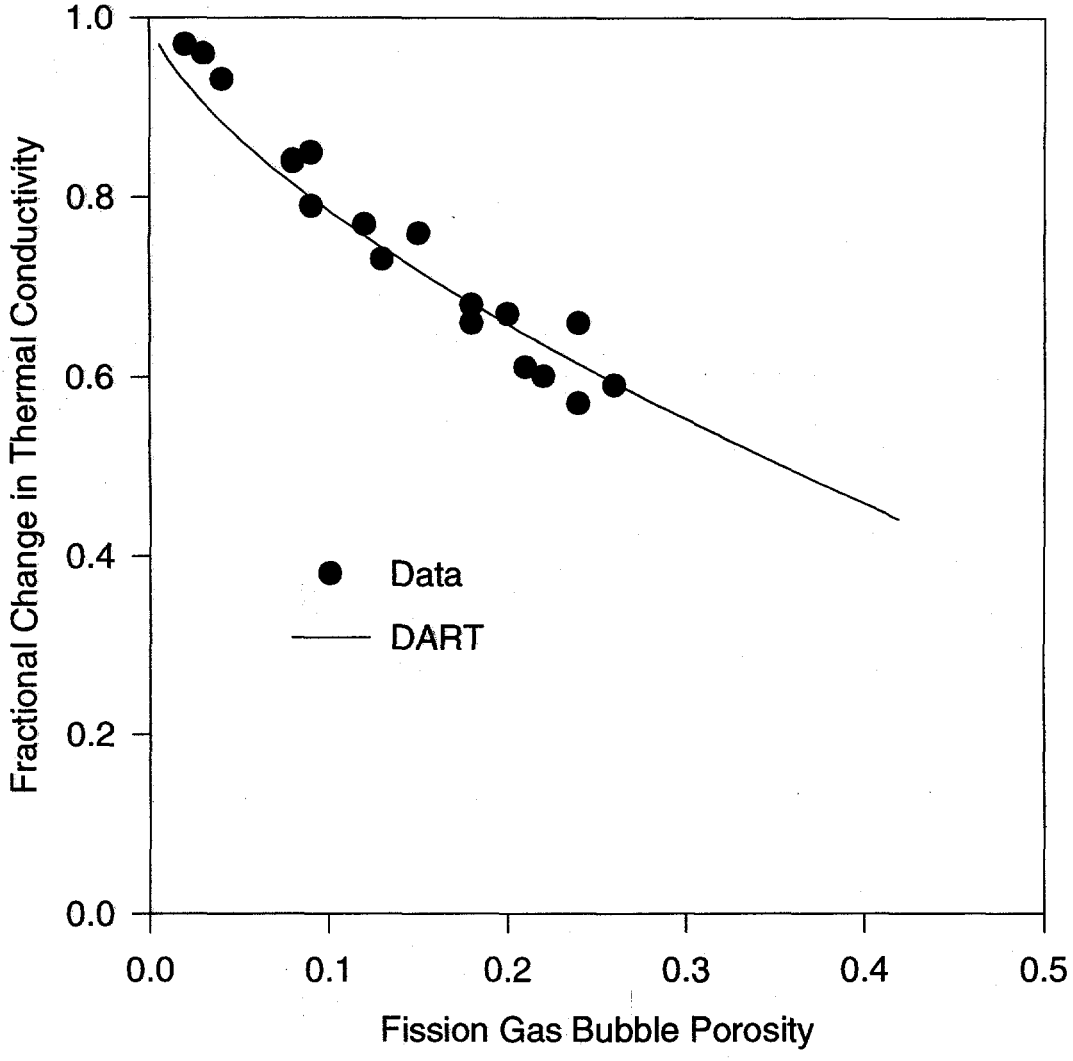

Fig. 5. DART-calculated and measured (deduced from electrical conductivity measurements) change in thermal conductivity for U_3Si fuel as a function of irradiation-induced porosity in irradiated and subsequently annealed bulk U_3Si

affected by several microstructural changes that occur in the fuel core during irradiation. An important factor in reducing the overall amount of net swelling is radiation-enhanced sintering of fabrication voids. In U_3O_8, this effect was first demonstrated by Reinke [2], and later confirmed by an experiment Martin et al. [3], in which U_3O_8 dispersion fuel made with depleted uranium was irradiated. The fabrication voids within the U_3O_8 particles, as well as cracks and gaps resulting from fabrication, were found to have sintered to spherical (or eliptical) cavities after irradiation. It is well established that an increase in dispersant loading also increases fabrication voids.

Inasmuch as a fraction of the sintered porosity can be taken up by the swelling fuel, the fabrication voids can substantially reduce the net fuel swelling.

Except for the calculation of thermal conductivity of the dispersion material described in Section 3, DART does not currently model the thermal performance of the fuel element. Thus, fuel temperature and linear power (i.e., fission rate), are required input into the analysis. In a fully coupled mode, the calculation of fuel deformation, fuel swelling, and thermal conductivity is interactive with the thermal analysis.

No matrix swelling is assumed to occur during reactor operation. This assumption is based on the relative swelling rates of the matrix and the fuel, from which it can be seen that fuel swelling is several orders of magnitude greater than matrix swelling. Inclusion of matrix swelling would lead to a slight increase in predicted rod diameter or plate/tube thickness.

The fuel particles are assumed to be identical in size and to have a uniform spherical shape. The actual fuel particles vary in size and are irregular in shape. However, because irregular particle shapes are difficult to handle mathematically, and because the orientation of the particles is random, an assumption of uniform overall behavior seems reasonable. In addition, particle-particle interactions are ignored. If particle-particle interactions are included, a greater degree of swelling than predicted by the model will occur.

No change in yield stress with fluence is considered. Evaluation of available data indicates that the change in yield stress due to fluence is negligible. Inclusion of this phenomenon will slightly reduce deformation estimates. In addition, the effects of irradiation-enhanced creep and irradiation hardening are not considered. Consideration of these phenomena would require time-dependent deformation analysis, which would add significantly to the complexity and execution efficiency of the DART code. The effects of irradiation-enhanced creep and hardening are accounted for by the inclusion of a phenomenological factor that multiplies the aluminum yield strength. The value of this factor depends on the geometry of the element, i.e., plate or rod.

The DART mechanical analysis addresses the mechanical behavior of dispersion fuel plates, tubes, and fuel rods. The model examines a system of spherical fuel particles surrounded by a large spherical shell of matrix material bonded to an outer shell of aluminum cladding. This approach treats the inner sphere as an elastically deforming body and the spherical shell as perfectly plastic [4]. The DART swelling models provide the driving force for mechanical deformation. The model is derived directly from the equations of equilibrium, compatibility, strain displacement, and the constitutive equations (stress-strain relationships) coupled with the assumption of incompressibility of plastic strains. The boundary conditions assume finite radial stresses at the center of the inner sphere, no discontinuity in the radial stress at the fuel/matrix interface, and no pressure on the outer surface of the spherical shell. It is also assumed that thermal expansion and swelling are not functions of radial position and that the outer radius of the spherical shell approaches infinity. This approach to thermal and swelling strains is based on calculations that indicate the temperature changes across a fuel plate or rod are small.

The model consists of the stress analysis of a hard sphere of radius a, assumed to behave elastically, surrounded by a spherical shell with outer radius b of a softer material that is assumed to behave in a perfectly plastic manner ($b >> a$). This plastic behavior is assumed to extend out to a plastic radius r_c such that $a < r_c < b$. This procedure yields an equation for the interfacial pressure (radial stress) at the fuel/matrix interface in terms of fuel particle swelling and plastic deformation in the matrix (i.e., as the interfacial pressure increases, plastic flow is induced in the matrix out to some radius beyond which only elastic deformation occurs). Based on the results of a general solution to the problem, an approximation is introduced that avoids the simultaneous solution of the interfacial pressure and the radius of plastic deformation. For positive interface pressure P_I,

$$P_I = 2\left[\frac{1}{3} + \ln\left(\frac{r_c}{a}\right)\right] S_y, \tag{55}$$

where S_y is the yield stress determined from the von Mises criterion for plastic flow. The results of the general solution indicate that r_c increases rapidly to include most of the matrix aluminum. Thus, it appears reasonable to make the approximation that the fuel volume fraction is given by

$$\frac{V_o^f + \Delta V^f}{V_0^c} = \frac{4/3\pi a^3}{4/3\pi r_c^3} = \left(\frac{a}{r_c}\right)^3, \tag{56}$$

where $\frac{V_0^f}{V_o^c}$ is the as-fabricated fuel volume fraction in the core and $\frac{\Delta V^f}{V_o^c}$ is the increase in fuel volume fraction due to processes such as as-fabricated pore closure and fuel particle swelling. Thus, from Eqs. 55 and 56,

$$P_h = P_I = \frac{2}{3}\left[1 - \ln\left(\frac{V_0^f + \Delta V^f}{V_0^c}\right)\right] \beta S_y, \tag{57}$$

where P_I has been identified with the hydrostatic stress within the fuel particle P_h, and β is a phenomenological factor (discussed above) that has been introduced to account for the effects of irradiation (e.g., irradiation-enhanced creep and hardening).

5 DART Model for Aluminum Silicide Fuel Reaction

U_3Si_2 reacts exothermally with aluminum to form the reaction product $U(Al,Si)_3$, a notation for UAl_3 in which Si has been substituted for some of the aluminum atoms. Below the melting temperature, the reaction is diffusion controlled and proceeds quite slowly. Irradiation enhances diffusion rates. The interaction depth y (μm) fits an

irradiation-enhanced diffusion correlation developed with irradiation data from the Oak Ridge Research Reactor (ORR) [19] and with irradiation data from the High-Flux Isotope Reactor (HFIR) [20]

$$y = \left(D_0^{ie} \exp(-Q^{ie} / kT)\, \dot{f} t \right)^{0.5}, \tag{58}$$

where $D_0^{ie} = 3.74 \times 10^{-17}$ μm²/s and $Q^{ie} = 7182$ calories. At higher temperatures, thermally activated diffusion becomes measurable and the correlation developed is

$$y = \left(D_0^{ie} \exp(-Q^{ie} / kT)\, \dot{f} t + D_0^{T} \exp(-Q^{T} / kT) t \right)^{0.5}, \tag{59}$$

where $D_0^{T} = 9.27 \times 10^{20}$ μm²/s, and $Q^{T} = 83{,}357$ calories.

6 DART Theory of Irradiation-Induced Recrystallization

6.1 Introduction

Experimental observations on low–temperature swelling of uranium silicide dispersion fuels (U_3Si_2) irradiated in the ORR have shown that the growth of fission gas bubbles is affected by fission rate [21-23]. The swelling of U_3Si_2 exhibits a distinct knee that shifts to a higher fission density with increased fission rate. Below the knee, no gas bubbles can be detected by scanning electron microscopy (SEM); if present, they must be below the resolution limit of the instrument, i.e., smaller than ≈0.04 μm in diameter. Just at the knee, gas bubbles are first seen to form in a heterogeneous fashion. Above the knee, the bubble population rapidly multiplies and the bubble size increases with fission density. Bubble size distributions are clearly bimodal and bubble morphology of samples that have similar volume increase, albeit at different fission densities, is similar.

The bimodal distributions persist to very high fission densities for HEU at 9 and 16 x 10^{27} fissions m^{-3}. The second peak in the distribution shifts to a larger diameter as the bubbles acquire more fission gas. However, the total number of bubbles in the second part of the distribution remains relatively constant (≈3 x 10^{18} m^{-3}) for all of the examined samples. This is interpreted to mean that the larger bubbles nucleate and grow on a fixed number of sites.

The bubble morphology retains its stable character up to the highest fission densities, i.e., bubble size and spacing are rather uniform, with no sign of bubble interlinking. The bubbles also form patterns suggestive of association with an underlying microstructural feature.

State–of–the–art models for fission gas behavior do not predict dependence of bubble growth on fission rate, and a bubble population with the observed bubble diameters can only be calculated [24] if microstructural features such as grain boundaries or dislocation networks are introduced. The original grain size of the fuel is large, i.e., approximately that of the fuel particles. Therefore, very few, if any, grain boundaries exist in the as–fabricated fuel. Indeed, the bubble patterns suggest bubbles associated with grain–boundarylike features, as discussed below, and there is evidence in the literature to support this interpretation.

Grain "subdivision" was observed by Bleiberg et al. [25] and Lambert [26] in uranium dioxide. Bleiberg et al. [25] showed that original 10–20-μm grains subdivided into unit sizes of <1 μm at a dose of ≈2 x 10^{21} fissions m^{-3} while retaining their crystalline structure. UO_2 swelling also increased in rate at this point (i.e., a knee in the UO_2 swelling curve) and the bubble morphology is similar to that observed in U_3Si_2. More recently, other investigators have observed that the peripheral region of light water reactor (LWR) fuel pellets reveals an increasingly porous microstructure with burnup [27-31]. At burnups above ≈45 GWd/t U, a porous outer ring, with a typical thickness of 100-200 μm, is formed. Examination of this "rim effect" shows an extremely fine–grained structure, apparently formed by recrystallization of the original, much larger, UO_2 grains. Further evidence of this phenomenon has been found in ion bombardment studies on crystalline U_3Si [32]. In these studies, recrystallized grain sizes of ≈100 Å were observed directly in a high–voltage electron microscope. It seems plausible that formation of small grains also occurs in U_3Si_2.

Evidence for a restructuring of U_3Si_2 that is undergoing high doses of low–temperature irradiation indicates that a subgrainlike structure exists in U_3Si_2 above the knee [23]. This preliminary observation, as well as observations from UO_2 irradiations and the ion bombardment studies mentioned above, leads us to speculate that at high burnup (corresponding to the knee in the swelling curve), a dense network of subgrain boundaries forms in these materials. Upon this network, gas bubbles nucleate and then grow at an accelerated rate relative to that in the bulk material.

The observation in U_3Si_2 that gas bubble swelling depends on fission rate has led to the theoretical formulation presented in Section 6.2, wherein the fission–induced stored energy in the material is concentrated on a network of recrystallization nuclei; this concentration diminishes with dose because of interaction with radiation–produced defects (i.e., vacancy–impurity pairs). Recrystallization starts when the energy per nucleus is high enough to offset creation of grain boundary surfaces by creating strain–free volumes, with a resultant net decrease in the free energy of the material. In Sections 6.3 and 6.4, the theory is applied, within the context of the DART mechanistic treatment of gas bubble behavior, to the interpretation of swelling in U_3Si_2. In Section 6.4, the theory is used to calculate UO_2 swelling, as well as to provide an interpretation of the rim effect in UO_2. Finally, the conclusions are summarized in Section 6.5.

6.2 Model for Grain Recrystallization

The recrystallization model proposed in this paper is derived from recrystallization in heavily cold–worked solids [33-35]. During deformation of metals, dislocations interact and tend to cluster into arrangements of high dislocation density that are separated by regions with relatively low dislocation density. Clustering of dislocations is a general observation in deformed single–crystal and polycrystalline metals and alloys [35-37]; typical dislocation configurations are dislocation tangles, two–dimensional dislocation boundaries (or walls), and three–dimensional dislocation cell structures. The different dislocation configurations derive from energy minimization, where glide–dislocation configurations increasingly approach the minimum energy per unit length of dislocation line as dislocation density, and hence interaction between dislocations, increases.

The concept that recrystallization ion nuclei [38] could originate from small preformed "strain–free" blocks in a crystal within the microstructure of a deformed state was proposed by Cahn [39] and Beck [40]. These strain–free blocks within a crystal are formed by the spatial rearrangement of dislocations into lower–energy arrays by polygonization. This model for recrystallization nuclei was further modified by Cottrell [41], who suggested that an additional need for the formation of a successful recrystallization nucleus was likely to be the development of a highly mobile bounding interface. These ideas have led to the low–angle boundary migration model, in which a viable recrystallization nucleus has a size advantage over the neighboring subgrain structure and is surrounded, at least in part, by a highly mobile interface. The mobility of this interface is affected by impurity atoms, which in an irradiated fuel are amply provided by fission products.

Recent transmission electron microscopy examination of the porous region of high–burnup LWR fuel has revealed networks on dislocations [29,30], and the cell size of these subgrain networks corresponds to the grain size of the rim material. An alternative mechanism to low–angle boundary migration, and a mechanism by which a subgrain of the above type can be formed, is the process known as subgrain coalescence [34]. In this process, the constituent dislocations of a low–angle boundary that separate two subgrains migrate along the plane of the boundary and are incorporated into the structure of surrounding low–angle boundaries. As a result, the low–angle boundary disappears and the two originally separated subgrains are joined as one much larger subgrain. The driving force for subgrain coalescence originates in the reduction in stored energy that accompanies the transfer of a dislocation from one low–angle boundary to another of higher angle; as a result, the interface accepting the dislocations will increase in misorientation. The increase in size of subgrains that are agglomerating by subgrain coalescence is obviously a favorable step toward the formation of a recrystallization nucleus, as is the accompanying increase in misorientation of a segment of the interface that surrounds the coalesced region.

Relatively few published reports have examined the phenomenon of radiation–enhanced recrystallization [42,43]. In a study of the microstructure of two copper alloys after heavy ion irradiation and thermal annealing [43], it was observed that some type of solute segregation/precipitation mechanism caused the pinning of subgrain boundaries in one of the alloys in the damage region. This alloy essentially retained the small polygonized subgrain structure in the damage region after irradiation at 773 K, while the unirradiated region of the crystal completely recrystallized. This is in contrast to the other alloy, which displayed no evidence of subgrain–boundary

pinning, completely recrystallized, and showed no discernible difference between irradiated and nonirradiated regions.

The model for radiation–induced recrystallization described below is based, in part, on the following assumptions:

- A cellular dislocation structure evolves relatively early in the irradiation period.
- Impurities formed during fissioning of the material diffuse to cell walls as vacancy/impurity complexes.
- The impurities effectively pin the wall, i.e., dislocation movement to and from the wall is retarded.
- Not all cell walls are uniformly affected by impurities; the walls that contain no impurities continued to undergo subgrain coalescence, which results in viable recrystallization nuclei.

Based on the above discussion, it is assumed that there exist a number C_S of recrystallization nuclei per unit volume of material. We think that these nuclei form relatively early in the irradiation period at low values of stored energy and that they are associated with microstructural features such as subgrain-boundary triple points or walls of cellular dislocation structures. Recrystallization nuclei act as sinks for irradiation–produced defects. As the irradiation proceeds, the nuclei are eliminated by interaction with vacancy-solute pairs. In other words, the concentration of impurities reduces the mobility of the interface. Many potential solute atoms are produced during fission, e.g., gas atoms and rare earths. Thus, the available stored energy is concentrated on fewer and fewer nuclei (one can consider that the nuclei are holes in the material and that they act as stress concentrators), with a resultant increase in average energy per nucleus. Recrystallization is induced when the energy per nucleus is high enough to offset the creation of a grain boundary surface by creating a of strain-free volume, with a resultant net decrease in the free energy of the material.

It is assumed that the solute atoms require significant energy to become part of a dumbbell-shaped interstitial [44] and therefore, do not migrate via an interstitial mechanism. It is further assumed that long-range diffusion of vacancy-solute pairs to the immobile nuclei eliminates the nuclei at a rate given by

$$\frac{d c_s}{d t} = -K_{sm} c_s c_m, \tag{60}$$

where c_m is the pair concentration and K_{sm}, the reaction rate for the immobilization of recrystallization nuclei by vacancy-solute pairs, is defined as

$$K_{sm} = 4\pi r_{sm} D_{vI} / \Omega, \tag{61}$$

where r_{sm} is the annihilation radius of a recrystallization nucleus/vacancy-solute pair, D_{vI} is the diffusivity of the vacancy-solute pair, and Ω is the atomic volume. D_{vI} consists of thermal and athermal components, i.e.,

$$D_{vI} = \xi a^2 \upsilon_v e^{-\varepsilon_{vI}/kT} + \chi\sqrt{\dot{f}}, \tag{62}$$

where a is the lattice parameter, υ_v is the vibration frequency factor for vacancies, ε_{vI} is the migration energy for a vacancy-solute pair, ξ is a preexponential factor that accounts for deviations from diffusion in a pure solvent, $\dot{f}$ is the fission rate (fissions/cm^3/s), χ is a factor related to the strength of athermal diffusion, k is Boltzman's constant, and T is the absolute temperature.

The concentration of vacancy-solute pairs c_m is given by

$$\frac{\partial c_m}{\partial t} = 12(K + 7\omega_4^v c_v)c_I - c_m(\alpha c_i + 7\omega_3^v), \tag{63}$$

where K is the damage rate in displacements per atom per second; c_v and c_i are the concentrations of vacancies and interstitials, respectively; c_I is the solute concentration; ω_3^v and ω_4^v are the jump rates of vacancies away from and toward nearest–neighbor nuclei of solute atoms; and α is the recombination coefficient given by

$$\alpha = 12(\omega_0^v + \omega_0^i), \tag{64}$$

where ω_0^v and ω_0^i are the jump frequencies of vacancies and interstitials, respectively, unperturbed by the presence of a solute atom.

If we assume that the concentration of vacancy-solute pairs is in steady state with the concentration of vacancies, interstitials, and solute atoms (i.e., $\partial C_m/\partial t = 0$), we obtain

$$12(K + 7\omega_4^v c_v)c_I = c_m(\alpha c_i + 7\omega_3^v). \tag{65}$$

This expression for the steady–state concentration of vacancy-solute pairs consists of the direct production of solute-defect pairs by irradiation (first term on the left side of Eq. 65), pair production due to interaction between vacancies and solute atoms (second term on the left side of Eq. 65), the loss of pairs through the interaction between vacancy-solute pairs and interstitials (first term on the right side of Eq. 65), and the loss of pairs due to dissociation (second term on right side of Eq. 65). In most cases, direct production of solute-defect pairs by irradiation should have only a small influence on the proportion of vacancies and interstitials trapped in vacancy-solute pairs. However, if the temperature is low, the dose rate is high, and the point-defect-solute binding energy is large, then recombination will be important. For the more general case, where recombination is important, the

equation for c_m is obtained from Eq. 65 (neglecting the effect of direct production of vacancy-solute pairs by irradiation, i.e., the first term within parentheses on the right side of Eq. 65) as

$$c_m = \frac{84\omega_4^v c_v c_I}{(\alpha c_i + 7\omega_3^v)}. \tag{66}$$

An equilibrium concentration of mobile defects is reached relatively early in the irradiation. Studies by Rest [45], who used a chemical rate theory of solute segregation for a solute concentration that depends on the fission (or dpa) rate, indicate that the above result (Eq. 66) for a fixed solute concentration is approximately true for the irradiation conditions of interest in this paper. In this case, the relevant solute concentration is that which is in dynamic solution within the fuel matrix and is thus able to participate in vacancy-solute pair formation. The equilibrium concentration of mobile point defects within the bulk material, c_v and c_i, can be determined from the rate equations that describe point–defect behavior, which, for negligible bulk diffusion (e.g., to a surface) are given by

$$\frac{\partial c_i}{\partial t} = K - K_{iv} c_i c_v - K_{sv} s_v c_v, \tag{67}$$

and

$$\frac{\partial c_i}{\partial t} = K - K_{iv} c_i c_v - K_{si} s_i c_i, \tag{68}$$

where K_{iv}, K_{sv}, and K_{si} are the rate coefficients for mutual recombination and for the annihilation of vacancies and interstitials at sinks. Here the assumption is made that the overall effect of solute concentration on the steady-state concentration of point defects is small. The sinks, which occupy time-independent fractions of the lattice nuclei, are assumed to be inexhaustible and randomly distributed. The rate coefficients are

$$K_{iv} = 4\pi r_{iv}(D_i + D_v)/\Omega \cong 4\pi r_{iv} D_i/\Omega, \tag{69}$$

$$K_{sv} = 4\pi r_{sv} D_v/\Omega, \tag{70}$$

$$K_{si} = 4\pi r_{si} D_i/\Omega. \tag{71}$$

Here, r_{iv} is the radius of the recombination volume; r_{sv} and r_{si} are annihilation radii and depend on the type of sink, e.g., dislocation line, jog, or microvoid; and D_v and D_i are the random-walk diffusion coefficients of vacancies and interstitials given by

$$D_v = \xi a^2 \omega_0^v, \tag{72}$$

$$D_i = \frac{2}{3}\xi a^2 \omega_0^i, \tag{73}$$

where and ξ is a preexponential factor that accounts for deviations from diffusion in a pure solvent,

$$\omega_0^v = \upsilon_v e^{-\varepsilon_v/kT}, \tag{74}$$

and

$$\omega_0^i = \upsilon_i e^{-\varepsilon_i/kT}, \tag{75}$$

where ε_v, ε_i and υ_v, υ_i are the migration energies and vibration–frequency factors for vacancies and interstitials, respectively.

When we use Eqs. 2, 5, and 6 in Eq. 1, and because $\omega_0^v << \omega_0^i$, we obtain

$$\frac{1}{c_s}\frac{dc_s}{dt} = -\frac{28\pi\, r_{sm} c_1 D_{vl} \omega_4^v c_v}{\Omega\left(c_i + 7\omega_3^v / 12\omega_0^i\right)\omega_0^i}. \tag{76}$$

The concentration of viable recrystallization nuclei, which results from the integration of Eq. 76, is quite different from that given by classical nucleation theory in that the concentration decreases with fluence instead of increasing with irradiation, until the nucleation barrier is surmounted and the higher energy state of the crystal forms. In the present case, the nuclei are formed early in the irradiation by the damage process at relatively low values of strain energy. As the irradiation proceeds and the nuclei are eliminated by interaction with the vacancy-solute pairs, the available stored energy is concentrated on fewer and fewer nuclei, thus increasing the energy per nucleus. For a given value of stored energy E_s, nucleation of a new crystal of material results in a net change in free energy ΔG, given by

$$\Delta G = -E_s V + 8\pi\gamma\left(\frac{3}{4\pi}V^{2/3}\right), \tag{77}$$

where V is the volume of the newly nucleated crystal (a spherical crystal shape has been assumed for simplicity), and γ is the surface energy density. The first term on the right side of Eq. 77 is the decrease in free energy due to the creation of a strain-free volume V, and the second term is the work required to create the boundary surface. The maximum value of ΔG occurs at a value of V given by

$$V_{max} = \frac{4\pi}{3}\left(\frac{4\gamma}{E_s}\right)^3, \tag{78}$$

where the value of ΔG at V_{max} is

$$(\Delta G)_{max} = \frac{128\pi}{3}\frac{\gamma^3}{E_s^{\,2}}. \tag{79}$$

From Eqs. 78 and 79, we see that as E_s increases, V_{max} and $(\Delta G)_{max}$ shift to smaller values. When $(\Delta G)_{max}$ decreases to a value approximately equal to the thermal energy kT, a relatively small energy fluctuation can allow the system to jump over the energy barrier, and a new recrystallized grain of material will be created. As $(\Delta G)_{max}$ approaches kT, the rate of change in the stored energy (which, as discussed above, is taken to be concentrated on the network cs), of the nuclei with respect to a change in cs is given by Boltzman's law, i.e.,

$$\frac{dE_s}{dc_s} = -\frac{kT}{c_s}. \tag{80}$$

Equation 76 provides a solution for c_S that is based on a kinetic analysis, whereas the equation for c_S provided by Eq. 80 is based on a thermodynamic analysis. By equating c_S obtained from Eq. 76 to the value of c_S determined from Eq. 80, where a relatively small energy fluctuation can allow the system to jump over the energy barrier and cause the creation of a relatively defect–free crystal of material, we obtain a relationship for the value of the fission density (m^{-3}) FDX at which recrystallization will occur, i.e.,

$$FDX = \frac{E_{sf}\,\dot{f}\,\Omega\left(c_i + 7\omega_3^v / 12\omega_0^i\right)\omega_0^i}{28\pi\, r_{sm} kTc_I D_{vI}\omega_4^v c_v}, \tag{81}$$

where $\dot{f} = BK$ (B is a conversion factor), $E_{sf} = E_s + E_f$, and E_f is the formation energy of a viable nucleus. Equation 81 can be simplified to

$$FDX = \frac{E_{sf}\left[9\,\Omega\,\dot{f} + 7a\sqrt{\pi B r_{iv}\xi\upsilon_v\Omega\dot{f}}\,e^{-(\varepsilon_{vI}-\varepsilon_v/2)/kT}\right]}{168\,\pi r_{sm}\,kTc_I\left(\xi_{vi}\,a^2\,\upsilon_v\,e^{-\varepsilon_{vI}/kT} + \chi_2\dot{f}\right)}. \tag{82}$$

Equation 81 or 82 is the basic result of this generalized analysis.

Before proceeding, we must establish criteria to determine when mutual recombination of point defects dominates annihilation at internal sinks, and when the loss of vacancy-impurity pairs by recombination with interstitials dominates pair loss due to dissociation (i.e., vacancy emission). If the assumption is made that $s_v \approx s_i$, the solution to Eqs. 67 and 68 is given by

$$D_v c_v = D_i c_i = (K / f_0^{1/2})\left[(1+Q)^{1/2} - Q^{1/2}\right], \tag{83}$$

where

$$Q = \frac{s_i^{\,2} K_{si}^{\,2} D_v}{4 K K_{iv} D_i}, \tag{84}$$

and

$$f_0 = \frac{K K_{iv}}{D_i D_v}. \tag{85}$$

For values of K above a minimum value K_{min} (e.g., those for ORR and HFIR irradiation conditions), Q<<1 and corresponds to mutual recombination that is dominant over annihilation at internal sinks, and leads to

$$D_v c_v = D_i c_i = \left(\frac{K D_i D_v}{K_{iv}}\right)^{1/2}. \tag{86}$$

At higher temperatures, Q>>1 and corresponds to annihilation at internal sinks dominant over mutual recombination, leading to

$$D_v c_v = D_i c_i = \frac{K D_i}{s_i K_{si}} = \frac{K D_v}{s_v K_{sv}}. \tag{87}$$

Correspondingly, for vacancy-impurity pairs, if the temperature is low, dose rate high, and point-defect-impurity binding energy large, then $\alpha c_i >> 7\omega_3^v$ and the loss of pairs due to recombination will be important. In this case, Eq. 81 becomes

$$FDX = \frac{E_{sf}\sqrt{f}\,\omega_0^i c_i \Omega}{28\pi\, r_{sm} k T c_I \chi \omega_4^v c_v}, \tag{88}$$

where, for these conditions, it is reasonable to assume (as will be quantified below) that athermal diffusion of the pair dominates over thermal diffusion, i.e., $\xi a^2 \upsilon_v e^{-\varepsilon_{vi}/kT} < \chi\sqrt{\dot{f}}$. On the other hand, if the temperature is high enough (e.g., as will be shown later for T in the intermediate–to-high temperature regime), the dissociation rates of the vacancy-impurity pairs are much higher than the loss rate of the vacancy in a vacancy-impurity pair by recombination with interstitials, and Eq. 81 becomes

$$FDX = \frac{E_F' \dot{f} \Omega \omega_3^v}{48\pi r_{sm} kTc_I \xi a^2 \upsilon_v e^{-\varepsilon_{vI}/kT} \omega_4^v c_v}, \tag{89}$$

where, for these conditions, it is reasonable to assume (as will be quantified below) that thermal diffusion of the pair dominates athermal diffusion, i.e., . $\xi a^2 \upsilon_v e^{-\varepsilon_{vi}/kT} > \chi\sqrt{\dot{f}}$.

Table 3. Values of various properties used in calculating recrystallization dose for U_3Si_2

Property	Value	Reference
υ_v	5×10^{13} s^{-1}	46
ε_v	0.9 eV	47
ε_{vi}	1.3 eV	Present Calculations
χ	6×10^{-24} cm$^{7/2}$ s$^{-1/2}$	Present Calculations
E_{sf}	2.0 eV	Present Calculations
c_I	1×10^{-6}	Present Calculations
r_{iv}	2×10^{-10} m	48
r_{sm}	3×10^{-10} m	48
ξ	0.1	Present Calculations

6.3 Recrystallization and Swelling in U_3Si_2

Figure 6 shows calculated values and measured data from Ref 23; the recrystallization dose for U_3Si_2 was calculated by solving Eq. 79 and the values of the material constants listed in Table 3 as a function of fission rate for an irradiation temperature of 373 K. Because many of the material constants for U_3Si_2 are not available, estimates of various parameters were taken from the references listed in Table 3. As is evident from Fig. 6, the above analysis provides a plausible interpretation of the observed knee in the U_3Si_2 swelling curve. Figure 6 also shows the analogous calculation and data for UO_2, which are discussed in the next section.

The DART code was used to calculate U_3Si_2 swelling. Fuel grain size was taken as the as–fabricated value until fuel burnup reached the recrystallization dose calculated with Eq. 79. Subsequently, the grain size used in the DART calculation was reduced to 0.5 μm (see below for details).

The following assumptions were made for the DART model:

1. Whole–bubble destruction is the physically realistic mechanism of gas atom re–solution from gas bubbles. Below a certain critical size, bubbles are completely destroyed when "hit" by a passing fission fragment; above the critical size, the bubbles survive the encounter.

2. The critical size for whole–bubble destruction is smaller for bubbles on grain surfaces than for bubbles in the bulk material because the gas–atom capture strength of the grain surfaces is strong. Here, a zero critical size is used for grain boundary bubbles.

3. Gas atoms diffuse from the bulk material to the grain surfaces by irradiation–enhanced diffusion.

4. The nucleation factor for bubbles on grain faces and grain edges is the same as that for bubbles within the grains (the nucleation factor is the probability that two interacting gas atoms will form a stable gas–bubble nucleus).

5. Gas atom diffusivity on grain surfaces is a factor of 10^4 greater than in the bulk material.

6. Both grain faces and grain edges are included in the calculation. Gas on grain faces can vent to grain edges upon bubble interconnection. The observed bubble population is its uniformly distributed and noninteracting. As discussed in Section 6.1, the total number of bubbles in the second peak of the measured bimodal distribution remains relatively constant for all examined samples.

7. The large bubble population inhabits fixed sites. These sites are formed upon grain recrystallization and are associated with nodes formed by the intersection of grain edges within the subgrain boundary structure. Fission gas that collects along grain edges vents upon intersection with these nodes, where it is trapped. Gas bubbles at these dead–end nodes grow as they continue to collect additional gas.

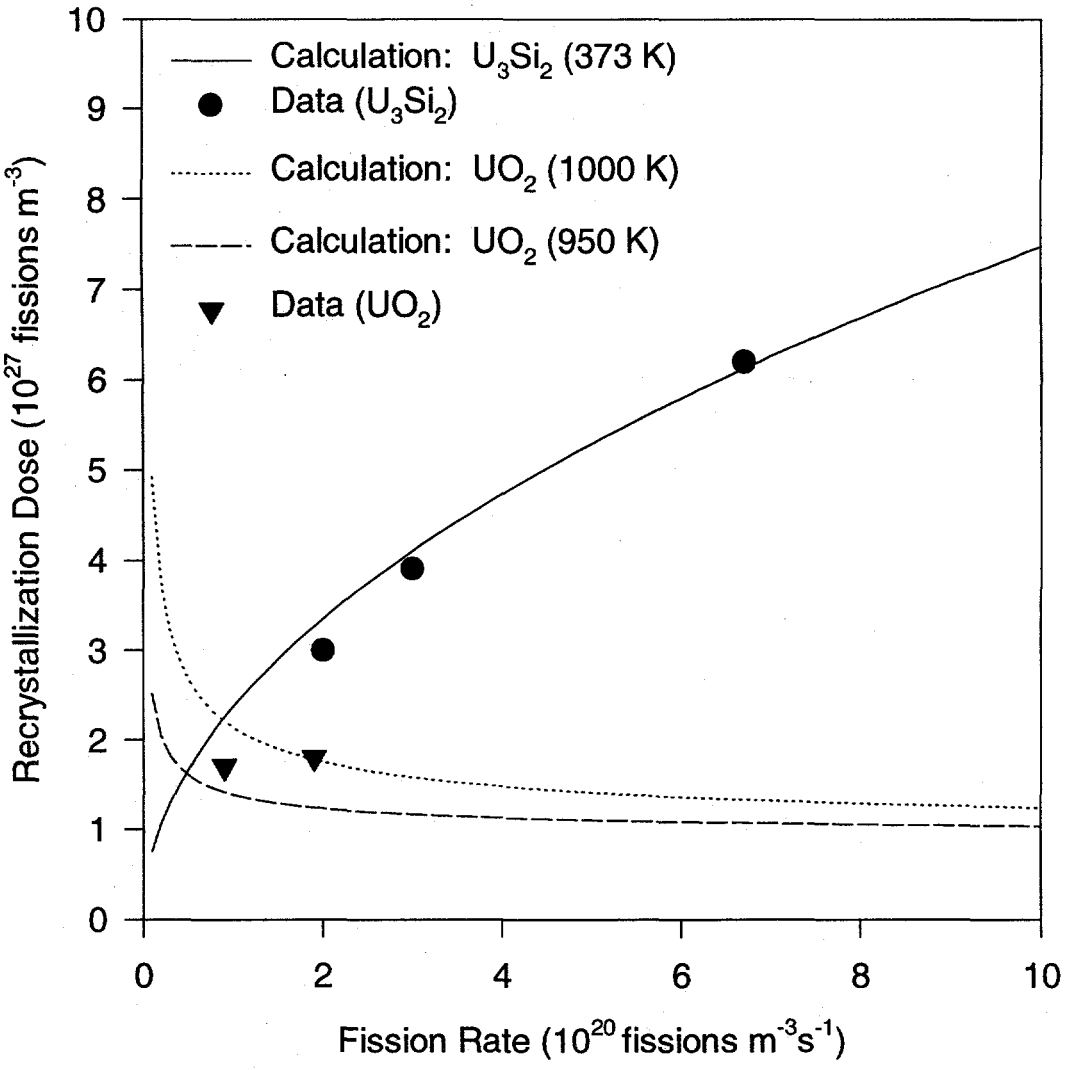

Fig. 6. Calculated curve of Eq. 79 and data from Refs. 23, 25, and 26

The results of DART calculations made without Assumption 7 are not consistent with the measured distributions. First, the data show a bimodal bubble size distribution (very evident from the SEM photomicrographs), whereas the calculated distributions do not. (The calculated quantities do show a bimodal bubble size distribution if very small bubbles are included in the plot. However, these small bubbles are well below the limits of experimental resolution). Second, the calculated distributions are much broader than the measured quantities. If the grains are assumed to be cubes and the dead–end nodes are taken to be grain corners formed by

the intersection of six grain edges, the number of nodes per cubic centimeter is given by the inverse of the cube of the grain diameter.

Upon grain recrystallization, gas diffuses athermally (by irradiation–enhanced diffusion) from the bulk material to the grain faces, where it accumulates in gas bubbles that grow until the grain face is saturated. DART calculates fission gas saturation of the grain–face by directly addressing the calculated distribution of fission gas bubble sizes. Grain face saturation occurs when the projected areal coverage of the grain face by these bubbles exceeds the maximum areal coverage. If the gas is assumed to be made of equal, closely packed, touching bubbles, the maximum areal coverage per unit area of grain face is 0.907.

Once formed on the grain edge, the bubbles grow by accumulating additional gas that arrives from the grain faces. When long–range interconnection of the grain edge porosity occurs, the gas is vented to the dead–end nodes. The DART model for calculating the probability of long–range grain edge tunnel interconnection is based on the assumption that the long–range interconnection is a function of the swelling of the grain edge bubbles. This assumption is supported by both experiment and theory for oxide fuels [49]. The value of the grain edge bubble fractional swelling at which long–range interconnection takes place if the fuel microstructure and gas bubble morphology are homogeneous is 0.055. To account for local fluctuations in fuel microstructure and gas bubble morphology, the grain face saturation and the long–range grain edge interlinkage fractions are assumed to be statistical distributions around average values of these parameters.

The DART mechanical/stress model consists of spherical fuel particles surrounded by matrix aluminum. The model treats the inner fuel sphere as an elastically deformable body and the surrounding shell of aluminum matrix material as perfectly elastic. During irradiation, fission induces elastic deformation of the fuel particles. First, the as–fabricated pores in the matrix material close in response to expansion of fuel particle volume, then plastic flow/swelling of the aluminum occurs.

In Figs. 7a and b, the points connected by solid lines show DART-calculated bubble size distribution at fission densities of 9×10^{27} m^{-3} and 16×10^{27} m^{-3} when the dead–end nodes are included in the analysis and a recrystallized grain size of 0.6 μm is utilized. Grain recrystallization was calculated to occur at a fission density of 6.5×10^{27} m^{-3}. Also shown in Figs. 7a and b are data obtained from SEM photomicrographs of the irradiated material. The calculated bubble distributions for bubble sizes below 0.4 μm and 0.6 μm (Figs. 7a and b, respectively), are due to the accumulated gas in the dead–end nodes. Currently, DART calculates only the growth of an average–sized node and does not account for the experimentally observed distribution of node bubble sizes. In addition, the observed density of node bubbles appears to decrease from $\approx 3.6 \times 10^{18}$ m^{-3} at a fission density of 9×10^{27} m^{-3} to $\approx 2.4 \times 10^{18}$ m^{-3} at a fission density of 16×10^{27} m^{-3}. This decrease in density may be due to the consumption of smaller node bubbles by larger node bubbles. This process is currently not included in the DART calculations. Consequently, if we use 0.6-μm recrystallized grain size, which corresponds to a node density of 3.6×10^{-18} m^{-3}, the calculated size of the node bubbles at 16×10^{27} m^{-3} will be underpredicted, as seen in Fig. 7b. Given the above considerations, the DART calculations shown in Figs. 7a and b follow the trends of observed bubble size distribution in irradiated U_3Si_2 as a function of burnup and, as such, provide plausible

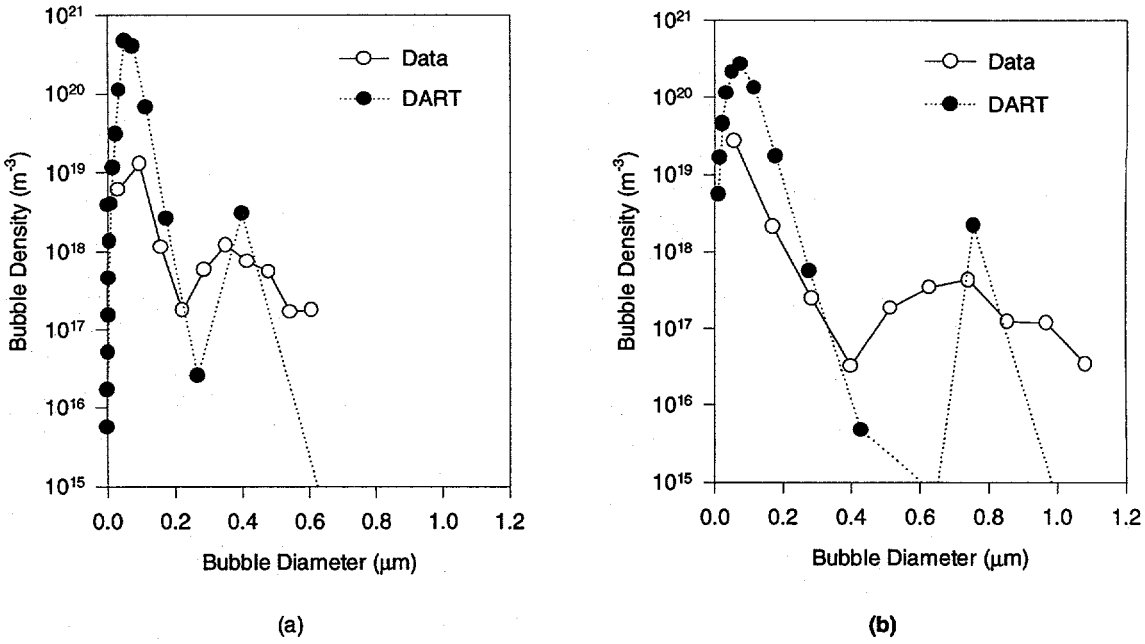

Fig. 7. Measured and DART-calculated bubble distributions in U_3Si_2 at (a) 9 x 10^{27} and (b) 16 x 10^{27} fissions m^{-3}. Effects of both fission density and grain size on position of second node of distribution are evident.

physical interpretation of the irradiation behavior. More detailed calculations may be possible when the actual subgrain morphology in the samples can be quantitatively determined.

6.4 Recrystallization and Swelling in UO_2

In this section, we assess the theory of grain recrystallization as applied to high–burnup UO_2, where grain subdivision has also been observed directly. Postirradiation examination [25] of bulk UO_2 wafers irradiated to high burnup in pressurized hot–water loops have revealed that grain subdivision from ≈15 to <1 μm in diameter occurred in the burnup range of 24–31 x 10^{20} fissions/cm^3. Changes in fuel volume determined by immersion–density measurements also showed that the swelling rate of the material changed from an initial value of ≈0.16% to 0.5% ΔV per 10^{20} fissions/cm^3 in the burnup range of 17–36 x 10^{20} fissions/cm^3. This observation of a knee in the swelling curve and its association with grain recrystallization is qualitatively similar to that observed in U_3Si_2 [23]. In Fig. 6, we presented recrystallization-dose data for UO_2 from Refs. 25 and 26, and values calculated with Eq. 81 and the material constants listed in Table 4 for irradiation temperatures of 950 and 1000 K. As is evident from Fig. 6, the analysis provides a plausible interpretation of recrystallization in UO_2.

Figure 8 shows DART–calculated fractional fuel volume increase in bulk UO_2 as a function of fission density with and without recrystallization. The calculation with recrystallization utilized a recrystallized grain size of 0.5 μm. Various properties used in the calculation are listed in Table 4. Except for E_{sf}, the ratio of the various

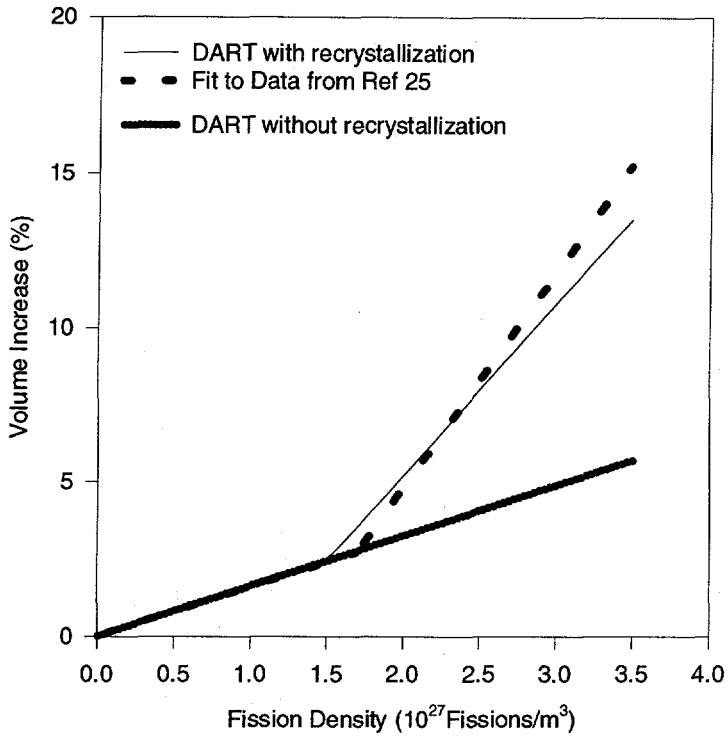

Fig. 8. Calculated fractional fuel volume increase in bulk UO_2 as a function of fission density with and without recrystallization and a fit to data from Ref. 25

energies in UO_2 to that in U_3SI_2 (see Table 3) is about the same as the ratio of the melting temperatures in the two materials. The radiation–enhanced diffusion parameter χ is a factor of 100 larger in UO_2 than in U_3Si_2. This is consistent with values of this property measured in other materials with higher thermal conductivity (as compared with UO_2, e.g., UC [31]). The solute concentration c_I is a factor of 100 lower in UO_2 than in U_3Si_2. This finding is consistent with the higher activity of an ionic material when compared with that of a largely covalent compound. By theory, with the materials properties shown in Table 4, grain recrystallization is predicted to occur at $\approx 20 \times 10^{20}$ fissions cm^{-3}. The observed bubbles in the recrystallized material are relatively widely spaced because of the high value of the grain boundary area per unit volume and the existence of fixed–nucleus nodes associated with the intersection of grain edges within the subgrain texture. Thus, the bubbles are noninteracting and grow by accumulation of gas atoms. It is this growth mechanism that leads to the linear swelling behavior shown in Fig. 8. This predicted behavior is consistent with the observation of regularly spaced, noninteracting bubbles in the U_3Si_2.

Table 4. Values of various properties used in calculating the recrystallization dose for UO_2

Property	Value	Reference
υ_v	$5 \times 10^{13}\ s^{-1}$	24
ε_v	2.4 eV	34
ε_{vi}	2.8 eV	Present Calculations
χ	$6 \times 10^{-23}\ cm^{7/2}\ s^{-1/2}$	34
E_{sf}	2 eV	Present Calculations
c_I	1×10^{-7}	Present Calculations
r_{iv}	1×10^{-10} m	27
r_{sm}	3×10^{-10} m	27
ξ	0.1	Present Calculations

As discussed in Section 6, Eq. 81 (or 82) provides an interpretation of recrystallization in UO_2 across a high–burnup cusp at the outer surface of the fuel rod, i.e., the so–called rim effect. This is seen more clearly in Fig. 9, which shows an example of the calculated burnup at which recrystallization will occur as a function of fractional radius and fuel temperature. Also shown in Fig. 9 are the fuel burnup and fission rate. When fuel burnup exceeds recrystallization burnup, calculated with Eq. 81 (or 82), recrystallization is predicted (hatched rectangle shown in Fig. 9). Also, the fission rate in this region, is enhanced by a factor of ≈2.8 over the average. Values of various properties used in the calculation shown in Fig. 9 are listed in Table 4.

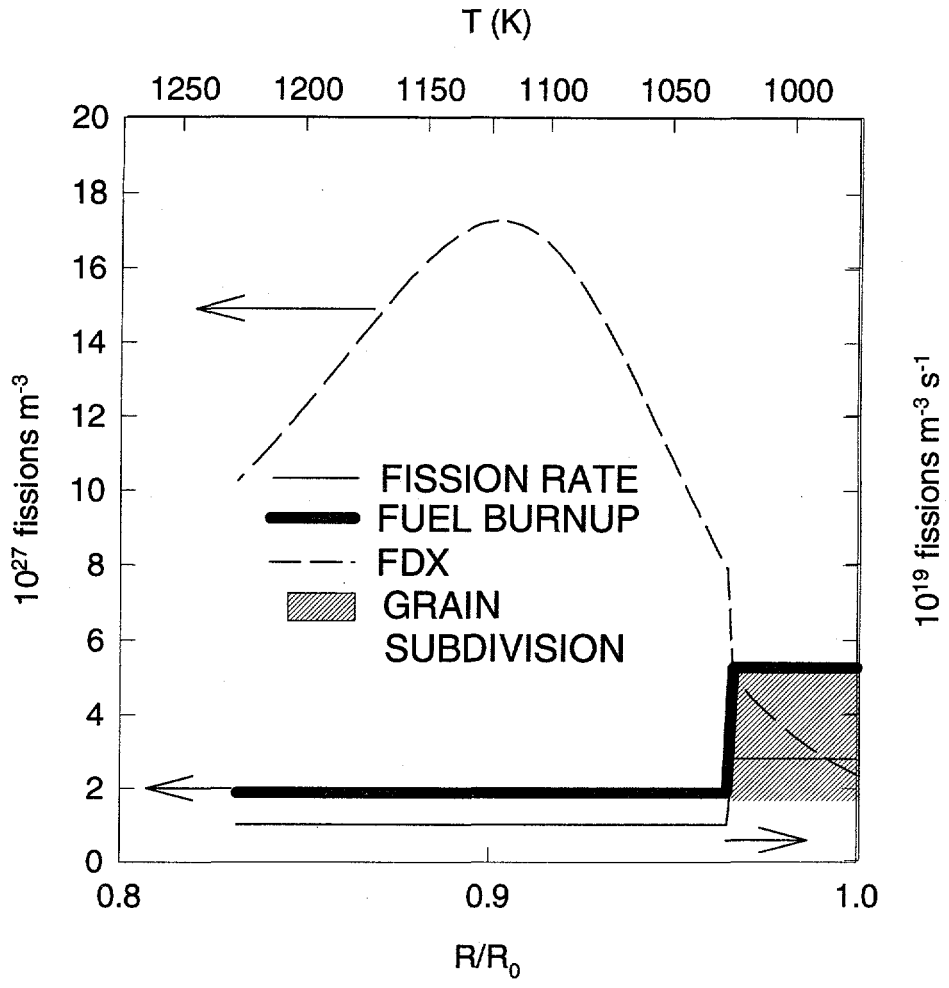

Fig. 9. Calculated burnup at which recrystallization will occur as a function of fractional radius (lower horizontal scale) and fuel temperature (upper horizontal scale). Also shown is fuel burnup and fission rate. When fuel burnup exceeds recrystallization burnup, calculated with Eq. 81 (or 82), recrystallization is predicted (hatched rectangle).

It is important to reiterate that a cellular dislocation structure has been observed within the porous band or rim [30]. This observation is consistent with the physical basis underlying the model presented in this paper. The results in Fig. 9 are intended to show that the trends of the calculation are consistent with observation. The predicted size of the porous band is a function of fuel temperature and fission rate, as well as of the properties listed in Table 4.

6.5 Discussion and Conclusions

Earlier in this section, we described a model for irradiation-induced recrystallization (grain subdivision) and swelling in U_3Si_2 and UO_2 fuels wherein the stored energy in the material is concentrated in a network of sinklike nuclei that diminish with dose because of interaction with radiation-produced defects. The sinklike nuclei were identified as a cellular dislocation structure that evolves relatively early in the irradiation period. Impurities formed during fissioning of the material diffuse as vacancy-impurity complexes to cell walls where they effectively pin the wall, i.e., dislocation movement to and from the wall is retarded. Not all cell walls are uniformly affected by impurities; walls that contain no impurities continue to undergo subgrain coalescence, which results in viable nuclei for recrystallization. Recrystallization is induced when the energy per nucleus is high enough to offset creation of grain-boundary surfaces by creating strain-free volumes, with a resultant net decrease in the free energy of the material. This formulation, applied within the context of a mechanistic treatment of fission gas bubble behavior, was shown to provide a plausible interpretation of the fission density at which grain subdivision begins, as well as the rate of fuel swelling, and the percentage of gas release in high-burnup UO_2 fuel.

In a recent paper [50], Nogita and Une describe their TEM observations of the formation mechanism of the recrystallized region (the so-called rim structure) in high-burnup UO_2 fuel. Dislocation density and the volume fraction of small intragranular fission gas bubbles increase with burnup. Low-angle boundaries begin to form above 7.5-8 x 10^{26} fissions/m^3. Analyses of fuel irradiated to 2.1 x 10^{27} fissions/m^3 show 20-30-mm subdivided grains, with high-angle boundaries due to the accumulation of an extremely high density of subboundaries; 50-200 nm recrystallized grains, adjacent to the subdivided grain region, that are presumably induced by the stored energy of the matrix; and the absence of bubbles within the recrystallized grains and the appearance of larger bubbles that most likely exist on the new grain boundaries. This is essentially the physical picture that we proposed as the basis of our theory of irradiation-induced recrystallization and swelling.

The observed dependence, at high burnup, of low–temperature swelling of irradiated uranium silicide dispersion fuels on fission rate is ascribed to the formation of grain boundaries in the material. Subsequently, fission gas atoms diffuse to the boundaries and nucleate fission gas bubbles that grow more rapidly on the boundaries than in the bulk material. We propose the existence of recrystallization nuclei (walls of a cellular dislocation network) on which stored energy is concentrated. Grain boundaries are formated when the density of recrystallization nuclei decreases to a level where the net change in free energy due to the creation of strain–free volumes (decrease in free energy) and boundary surfaces (increase in free energy) is approximately equal to the thermal energy kT. We further propose that the decrease in recrystallization nuclei density is due to interaction with mobile, irradiation–produced impurities (i.e., vacancy–impurity pairs).

The theory of grain recrystallization and gas–driven fuel swelling presented in this paper has been applied to the interpretation of the observed low–temperature swelling of irradiated uranium silicide dispersion fuels. The swelling rate of the material exhibits a distinct knee that shifts to higher fission density with increased fission rate. A subgrainlike structure has been observed in U_3Si_2 above the knee. No such structure is apparent in the material at fission densities below the knee. We propose that the basis for this kinetic phenomenon is the formation of

vacancy–solute pairs that, upon migrating to potential recrystallization nuclei, immobilize the nuclei and thereby increase the average value of the stored energy per nucleus. This theory was compared with data both swelling and bubble size distribution and provides a plausible interpretation of the phenomenon.

The theory was also applied to grain recrystallization in high–burnup UO_2, where grain subdivision was observed directly. Calculations for the onset of grain recrystallization, fuel swelling rate, and the size of the rim effect zone agree reasonably well with the data trends.

7 DART Theory of Gas Bubble Behavior in Amorphous Fuel

7.1 Introduction

Observations of certain low-enrichment, high-density, uranium-base intermetallic alloys, such as U_3Si and U_6Fe, have revealed extraordinarily large voids (breakaway swelling) at low and medium fuel burnup. This phenomenon of breakaway swelling does not occur in other fuel types, such as U_3Si_2 and UAl_3, where, instead, a distribution of relatively small, stable fission gas bubbles forms. The in-situ observations of ion-radiation-induced rapid swelling of intermetallic materials are consistent with growth by plastic flow.

In this section, we describe a microscopic theory of fission gas bubble behavior in irradiated amorphous compounds. The assumption underlying the overall theory is that the difference in the evolution of porosity in crystalline and amorphous U_3Si is due to a softening of the irradiated amorphous material, with a concurrent orders-of-magnitude increase in the effective gas bubble diffusivity due to plastic flow. The coupling of changes in shear modulus with radiation-induced softening of amorphous material and gas atom mobility within defect cascades is also discussed.

7.2 Model for Irradiation-Induced Softening of Amorphous Materials

The major differences between the crystalline and amorphous phases are due to changes in elastic properties. In the studies, substantial elastic softening of irradiated intermetallic compounds occurred in the crystalline phase and was associated with progressive destruction of the long-range chemical order. Brillouin scattering experiments and transmission electron diffraction studies have shown that single-crystal silicon and polycrystalline intermetallic compounds undergo dramatic elastic softening after irradiation with charged-particle beams. Measurements of the change in sound velocity show that the average shear constant decreases by as much as 30% in silicon and by as much as 50% in intermetallics [51]. These results point to a strong coupling between strain

and order parameters as a possible origin of the elastic softening and to strain accumulation as an important prerequisite for the amorphization of these intermetallics.

The degree of long-range atomic order S is exponentially dependent on the total irradiation dose ϕ t

$$S / S_0 = \exp(-K\phi \, \mathrm{t}). \tag{90}$$

Measurements of the Zr_3Al lattice dilatation $\Delta a / a$ show that $\Delta a / a$ increases with increasing dose, reaches a maximum value of ≈0.8% at the dose where amorphization starts, then drops abruptly to -0.7% $(S \approx 0)$ and thereafter remains approximately constant [52]. For doses up to 0.2 dpa, the percentage lattice dilation is a quadratic function of S

$$\Delta a / a = (\Delta a / a)_m \left[1 - (S / S_0)^2\right], \tag{91}$$

where $S / S_0 = \exp[-11.6\phi \, \mathrm{t}]$ is the observed dose dependence of S, and $(\Delta a / a)_m$ = 0.775% is the maximum lattice dilatation due to disordering. The results of postirradiation Brillouin scattering measurements of the same material show that a large (≈50%) decrease in the shear constant occurs after chemical disordering. The decrease occurs before the onset of amorphization, and, hence, the elastic softening is a precursor effect rather than a consequence of amorphization. This result is significant because it strongly suggests that an elastic instability triggers the onset of amorphization. For doses up to 0.15 dpa, the shear constant is a quadratic function of S

$$C / C_0 = 0.5\left[1 + (S / S_0)^2\right]. \tag{92}$$

The S^2 dependence described by Eqs. 91 and 92 implies that the shear constant is a linear function of volume dilatation, $3\Delta a / a$. Eliminating $(S / S_0)^2$ in Eqs. 91 and 92 yields

$$C / C_0 = 0.5\left[1 - (3\Delta a / a) / 4.65\right]. \tag{93}$$

As described by Eq. 93, the shear constant decreases linearly with volume dilatation and extrapolates through the glass gap. That is, the change in density between the partially disordered crystalline phase and the amorphous phase ≈2.5% at $3\Delta a / a \approx 4.7\%$, which is very close to the value of 4±1% measured for total volume expansion of amorphous Zr_3Al [53]. The loss of resistance to shearing at a dilatation of 4.7% indicates that the partially disordered material ($S \approx 0.2$) is mechanically unstable with respect to density fluctuations comparable in magnitude to the glass expansion gap. Because density fluctuations of comparable magnitude may occur in the cores of energetic cascades, the irradiation itself can provide the additional density fluctuation required to trigger an elastic-inelastic instability in the partially disordered material.

The elastic instability that occurs during irradiation is not one in which the entire crystal transforms catastrophically to an amorphous phase at some critical disorder. The glass expansion gap represents a nucleation

barrier against glass formation in the highly strained, metastable, disordered crystalline material. Although the dilatational strain will have a well-defined average value, local dilatation fluctuations result in regions of mechanical instability, that is, amorphization, and not everywhere simultaneously. In the context of the theory being developed in this section, the important point is that disorder results in a volume-dependent shear coefficient during irradiation similar to that associated with the heating and melting of metals.

7.3 Calculation of Gas Atom Diffusivities within Defect Cascades

Measurements of ion-beam mixing of tracer impurities in metallic glasses and in the pure crystalline elements that comprise the glasses [54] demonstrate that the ion mixing efficiency of the tracer impurities is greater in the metallic glasses than in either of the constituent elements. The radiation-enhanced diffusivities of the tracer impurities in the metallic glasses is within a factor of 10 of those measured in the crystalline materials. Although in the right direction, a factor-of-10 increase in the gas atom diffusivities is not sufficient to explain the breakaway swelling observed in irradiated U_3Si material. However, these results are consistent with the picture of cascade dynamics provided by molecular-dynamics computer simulations [55]. The simulations show that the cascade region exhibits a liquidlike structure during the thermal-spike phase of cascade evolution.

A simple picture for the relationship between the migration energy for diffusion and the elastic constants of the material can be developed on the basis of the following arguments. A diffusion jump introduces a lattice strain. One may expect the strain caused by the jump to be mainly a shear. The energy in this shear strain can be estimated by treating the material as a Hookeian solid. For Hookeian shear, the work done per unit volume of strain energy in the body is given by

$$W = \frac{1}{2}\varepsilon^2 C', \tag{94}$$

where C' is the shear modulus and ε is the strain caused by the jump. The energy in the shear strain is obtained by multiplying W by the strained volume. Choice of a volume given by $4/3\pi a^3$, where a is the atomic spacing, results in

$$E_m = \frac{2}{3}\pi a^3 C' \varepsilon^2, \tag{95}$$

which shows that a decrease in the shear modulus will result in a proportional decrease in the migration energy necessary for diffusion.

The thermally activated gas atom diffusivities in the amorphous phase can be described by an exponential dependence on temperature, i.e.,

$$D_g = D_0 \exp(-E_m / RT). \tag{96}$$

Gas atom mobility in irradiated crystalline material at relatively low temperatures is dominated by radiation-enhanced diffusion. However, a decrease in E_m may result in domination of the diffusion process by thermal activation. From Eqs. 93 and 95, the migration energy in the damaged material E_d is given by

$$E_d = E_m\left[1-(3\Delta a / a)/4.65\right], \tag{97}$$

where E_m is on the order of the migration energy in the undamaged material. Thus, the diffusivity in the damaged material is given by

$$D_d = D_0 \exp\left[(E_m / RT)(3\Delta a / a)/4.65\right]. \tag{98}$$

For a 3% volume dilatation, the diffusivity at 150°C would be enhanced by ≈11 orders of magnitude over thermal diffusion.

It is important to note that the gas atom diffusivity given by Eq. 98 is appropriate only for local regions of the amorphous (or crystalline) material. The dilitation $\Delta a / a$ in Eq. 98 applies to these damaged regions (for example, the volume of a damage cascade), and is estimated to have a lifetime on the order of the defect cascade (10^{-10} s). Equation 98 applies to damaged regions in partially disordered crystalline materials and in amorphous materials. The key difference between bubble behavior in most irradiated crystalline and in amorphous materials is that the amorphous materials can undergo substantial plastic flow due to an enhanced softening under irradiation. Some crystalline materials, however, behave very much like U_3Si because of very low shear modulus values (e.g., the γ phase of various uranium alloys). In irradiated amorphous materials that contain fission gas, over-pressurized bubbles can provide the driving force for plastic flow. In addition, density fluctuations produced by damaging cascades can be a driving force for microscopic deformation. Plastic flow, in turn, results in enhanced bubble coalescence and bubble sweeping of gas atoms out of solution.

The calculation of bubble growth in irradiated amorphous materials is complicated by the interplay between bubble growth (driven by plastic flow) and plastic flow (e.g., driven by bubble overpressure). To provide for a computationally tractable description of this phenomenon, the assumption is made that bubble motion in a material that undergoes plastic flow can be described by an effective bubble diffusivity based on random motion in a liquid where the bubbles move by volume diffusion. The diffusivity of a bubble of radius r_i migration by volume diffusion is given by

$$D_i = \frac{3\Omega}{4\pi r_i^3} D_a, \tag{99}$$

where Ω is the molecular volume and D_a is the diffusivity of the diffusing atoms. This diffusion is qualitatively described by the Stokes-Einstein equation

$$D_a = kT/(6\pi r_a \eta), \tag{100}$$

where r_a is the radius of the diffusing species and η is the viscosity. A softening of the material produces a decrease in η and a corresponding increase in D_a. The assumption is made here that, in irradiated amorphous materials, the effect of plastic flow can be described by using an effective atomic diffusivity D_a that is equal to D_d of Eq. 98.

8 Dart Methodology for Calculating Stress and Phase Gradients within U_3Si_2 Fuel Particles

As shown in Eqs. 35 and 37, the growth of fission gas bubbles depends on the hydrostatic pressure P_h in the fuel adjacent to the bubble surface. Equation 55 relates P_h to the overall fuel volume fraction and the aluminum yield stress and therefore provides an estimate of the average hydrostatic stress within the fuel particle. As seen in the above sections, a gradient in fuel composition will, in general, exist across fuel particle. This phase gradient will give rise to a gradient in swelling, and thus a gradient in stress. To realistically calculate the fission gas bubble size distributions (Eq. 1), and hence fuel swelling, we must introduce a mechanism for evaluating the stress gradient within the fuel particle.

DART employs a radial nodalization scheme to characterize temperature, stress, and phase gradients. As discussed in Section 3, a phenomenological factor has been introduced in the elastic/perfectly plastic analysis of fuel particle deformation within an aluminum matrix to account for the effects of irradiation (e.g., irradiation-enhanced creep and hardening) without resorting to a much more complicated time-dependent deformation analysis. This approach has been extended to the deformation analysis within the fuel particle. In particular, Eq. 55 is utilized for radial nodes that consist of a given phase surrounded by radial nodes that are composed of a different phase. In this case, the fuel volume fraction in Eq. 55, i.e., $V_o^f + \Delta v^f / V_o^c$, is replaced by the volume fraction within the fuel particle that is occupied by the given fuel phase, and the effective yield strength βS_y of aluminum in Eq. 55 is replaced with the effective yield strength of the different fuel phase.

9 DART Validation for Behavior of U_3Si_2 Particles Irradiated in the HFIR

As discussed in the above sections, DART consists of models for the formation of various phases of U_3Si_2 (i.e., aluminide, recrystallized, amorphized), the evaluation of fission gas bubble morphology and swelling within various phases, aluminum diffusion into the U_3Si_2 particle, thermal conductivity, and mechanical deformation. A key assumption in the bubble morphology model is that within the recrystallized material, the observed large bubble population inhabits fixed sites. These sites are formed upon grain recrystallization and are associated with nodes that are formed by the intersection of grain edges within the subgrain boundary structure (e.g., grain

corners). Fission gas that collects along the grain edges vents upon interconnection with these nodes, where it is trapped. The gas bubbles at these dead-end nodes grow as they continue to collect additional gas. Although the model is based on some assumptions that are derived from systems other than U_3Si_2, it represents a physically realistic interpretation of the observed irradiation behavior of U_3Si_2 over a wide rage of fission densities and fission rates.

Observations of photomicrographs of U_3Si_2 fuel particles dispersed in an aluminum powder and irradiated in the HFIR have revealed a microstructure of an outer aluminide shell (e.g., a UAl_3-type structure) that shows no evidence of grain recrystallization (Region 1 of Fig. 10F), an inner aluminide-type annulus that shows evidence of grain recrystallization (Region 2 of Figs. 10F, and Fig 10C), and a central region that shows swelling that is characteristic of an amorphous material (Region 3 of Fig. 10F). DART analyses of the evolution and swelling of this complex microstructure have identified the following phenomena. The formation of the outer aluminide shell acts as a restraint on the swelling of the inner fuel material. This is because the outer (unrestructured) aluminide shell contains predominantly small (not visible by SEM) intragranular bubbles (Fig. 10D). Thus, this outer shell has a relatively low swelling rate when compared with the interior regions (which are composed of recrystallized and/or amorphouslike material) and appears "hard," or stiff, when compared with the relatively "soft," or ductile interior regions. DART calculations show that if the outer aluminide shell does not form (e.g., for fuel particles irradiated in the absence of aluminum), fuel particle swelling rates increase significantly. It is conjectured (based on observation) that the aluminide material is stable against amorphization and recrystallization. Thus, for DART to generate an aluminide outer shell, aluminum diffusion into the material (i.e., through the outer fuel ring defined in the multinode configuration of the calculations) must occur before the recrystallization model predicts grain recrystallization in that node.

The inner nodes recrystallize prior to aluminum penetration, leading to an aluminide annulus with a refined grain structure (Region 2 of Figs. 10F and C). DART-calculated swelling rates in an annulus that has a refined grain structure are significantly higher (Fig. 10A) than what would occur in the absence of recrystallization (i.e., in the aluminide region, Fig. 10D) due to enhanced bubble growth on grain boundaries and on dead-end nodes. Subsequent to recrystallization, aluminum penetration of this inner annulus occurs, converting the material to a restructured (with a refined grain structure) aluminide region (Region 2 of Figs. 10F and C). The pre-exponential factor in the expression for the thermal diffusivity of aluminum was determined on the basis of a calculated amorphous annulus, which is consistent with the observations (Fig. 10B). As the simulation moves across the U-Si phase diagram, the code tests for whether the calculation has entered the unstable USi_2 phase. If so, models for the behavior of fission gas bubbles in irradiated amorphous U_3Si are invoked. Swelling rates in the amorphous inner core (Fig. 10E) are higher than in the outer crystalline regions because of plastic nature of this amorphous material in the presence of irradiation. The outer, relatively hard, crystalline regions constrain the swelling of the inner, relatively soft, amorphous core.

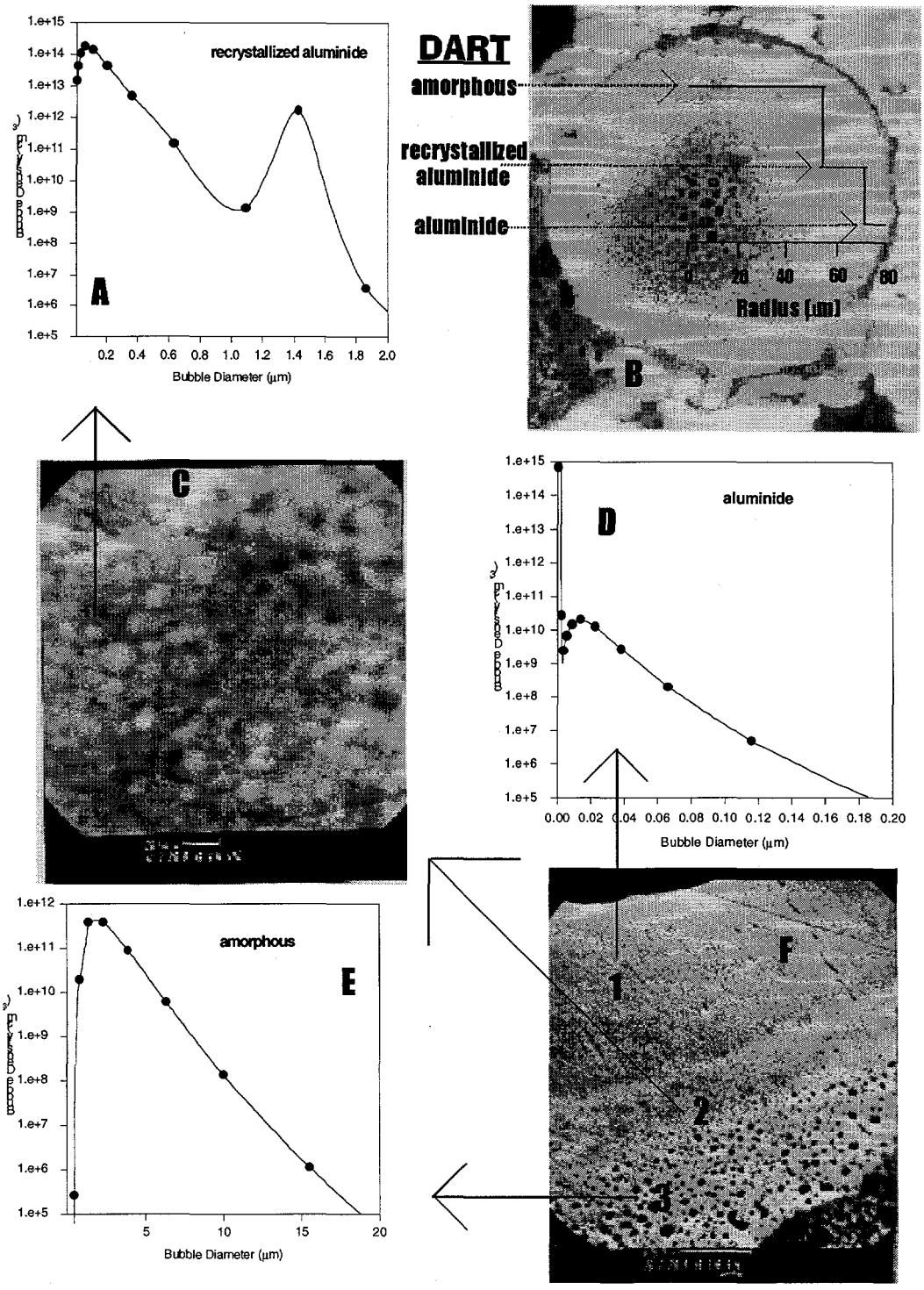

Fig. 10. DART interpretation of U_3Si_2 particle irradiation in HIFR

Calculated bubble distributions result in an absence (by SEM) of visible bubbles in the outer unrecrystallized aluminide shell (Fig. 10D), visible intergranular bubbles in the inner recrystallized aluminide annulus (Fig. 10A), and relatively large bubbles in the inner amorphous core (Fig. 10E). As shown in Fig. 10, these results are in qualitative agreement with the observations. In addition, the DART-calculated fuel restructuring overlaid on a photomicrograph of a cross section of a fuel particle, shown in Fig. 10B, follows the trend of the observations.

10 DART Validation for Irradiation Behavior of Various Designs of Uranium Silicide Dispersion Fuel Elements

The DART mechanical (stress) model consists of a fuel sphere that deforms because of both solid fission product and fission gas bubble swelling. The fuel sphere is surrounded by an aluminum matrix shell, which is assumed to behave in a perfectly plastic manner and which deforms (yields) when fuel particle volume expands. The effects of cladding are included by a suitable adjustment of the effective aluminum volume fraction. Currently, the effects of creep are not included; instead, the stress relaxation is approximated by lowering the aluminum yield stress to an "effective" value. Different values of this effective yield stress are used for the rod, plate, and tube geometries to simulate the quite complicated time-dependent deformation behavior of the rod and plate with the rather simplistic DART stress model. The deformation of the matrix and cladding material generates stresses within the expanding fuel particles, which affect the swelling rate of the fission gas bubbles.

The swelling fuel particles push the matrix aluminum into as-fabricated porosities and simultaneously cause cladding deformation. The swelling rate primarily depends on the plastic yielding of the aluminum matrix and cladding. The hydrostatic stress σ_i (i = 1,2 refers to plate or rod geometry), acting on the gas bubbles is given by (see Eq. 57)

$$\sigma_i = \frac{2}{3}\left[1 - \ln\left(\frac{V_o^F + \Delta V^F}{V_o^C}\right)\right]\beta_i \sigma_{Al}^Y(T), \tag{101}$$

where $\sigma_{Al}^Y(T)$ is the as-fabricated temperature-dependent yield strength of the aluminum, $\frac{V_o^F + \Delta V^F}{V_o^C}$ is the fuel volume fraction, and β_i is a factor that accounts for the effects of irradiation (e.g., irradiation-enhanced creep). The values of β_i used in DART are $\beta_1 = 7.5$ and $\beta_2 = 2.5$.

Results of DART calculations are shown in Figs. 11 and 12. The calculations shown in Figs. 11 and 12 were all performed at the same constant fuel temperature of 373 K. Figure 11 shows DART results for fuel swelling of U_3SiAl-Al in plate, tube, and rod configurations as a function of fission density compared with data. The lower calculated fuel swelling in the rod-type element is due to an assumed biaxial stress state as compared with an assumed uniaxial stress state for the plate and thin-walled tube geometries. Fuel swelling in plates results in plate

thickness increase only, while plate width and length remain relatively unchanged. Likewise, in tubes, only the wall thickness increases and the overall diameter remains unchanged. Thus, cladding of these element designs contains minimal lateral or circumferential strain and consequently, much less restraint compared with the hoop stress state in a solid-clad rod. Irradiation experiments have shown that plate-type dispersion fuel elements can develop blisters or pillows at high ^{235}U burnup when fuel compounds exhibiting breakaway swelling, such as U_3SiAl and U_3Si, are used at moderate to high fuel volume fractions. The U_3SiAl plate data shown in Fig. 11 exhibits this behavior at fission densities above about $\approx 5 \times 10^{27}$ m^{-3}. Figure 12 shows DART-calculated results for fuel particle swelling of low-enriched U_3Si_2-Al fuel plates and rods as a function of fission density. The calculated values shown in Fig. 12 indicate that irradiation-induced recrystallization occurred at $\approx 3.5 \times 10^{27}$ m^{-3}. Again, the fuel rods exhibit lower values of swelling than the plates because of the greater restraint imposed by the rod configuration.

Figure 13 shows DART-calculated results for pore closure of low-enriched U_3Si_2 fuel plates fabricated to 50% and 13% fuel and pore volume fractions, respectively, compared with the measured values [56]. In Fig. 13, V_p^0 and V_p are the inital and remaining values of the fraction of as-fabribcated porosity in the dispersion. The DART calculations show the effects of fuel recrystallization (increased rate of pore closure) which is calculated to occur at a fission density of 3.5×10^{27} m^{-3}. Both the data and the calculations show that the as-fabricated porosity is completely removed by 4.5×10^{27} m^{-3}. As is evident from Figs. 11-13 , DART calculated fuel swelling and pore closure is in reasonable agreement with observation.

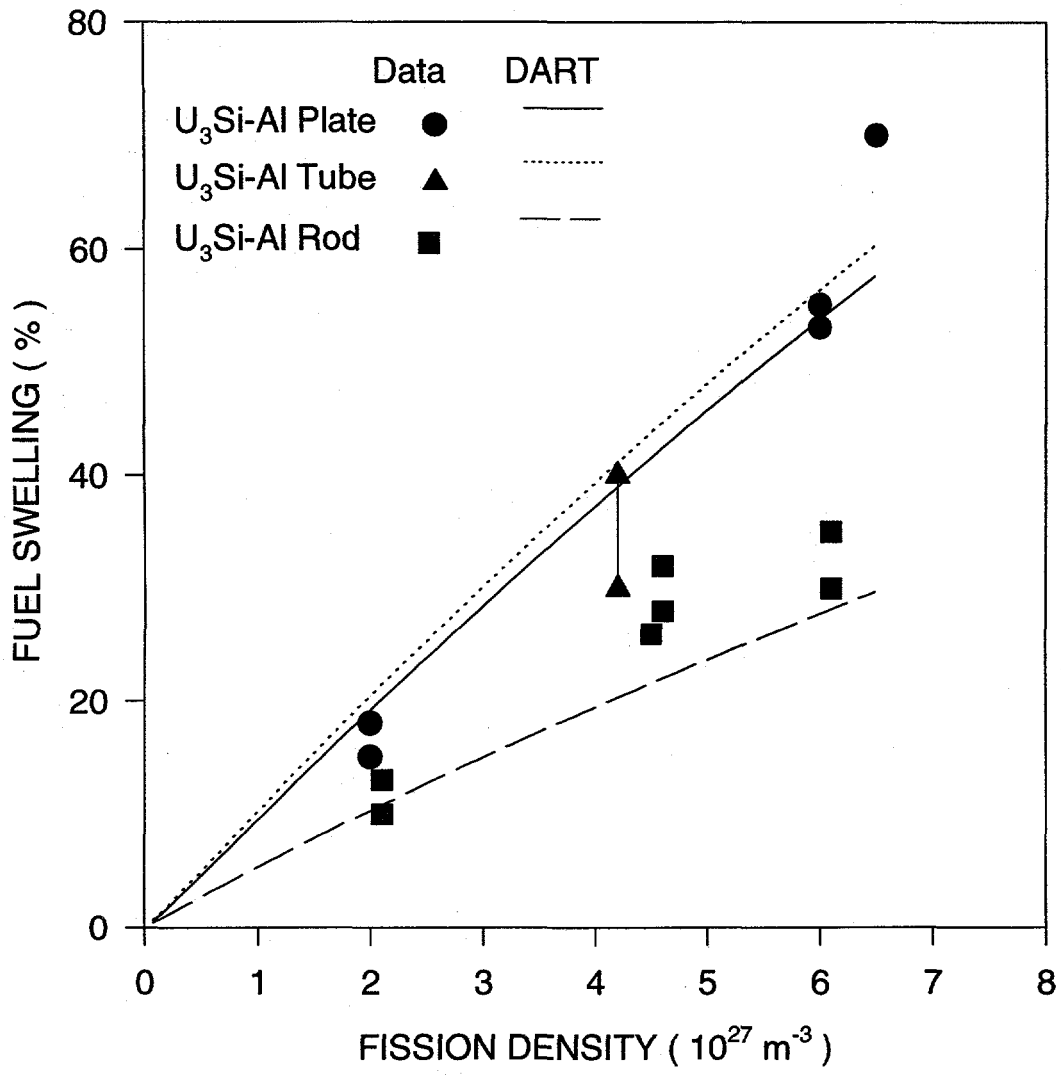

Fig. 11. DART results for swelling of U_3SiAl-Al in plate, tube, and rod configurations as a function of fission density compared with data

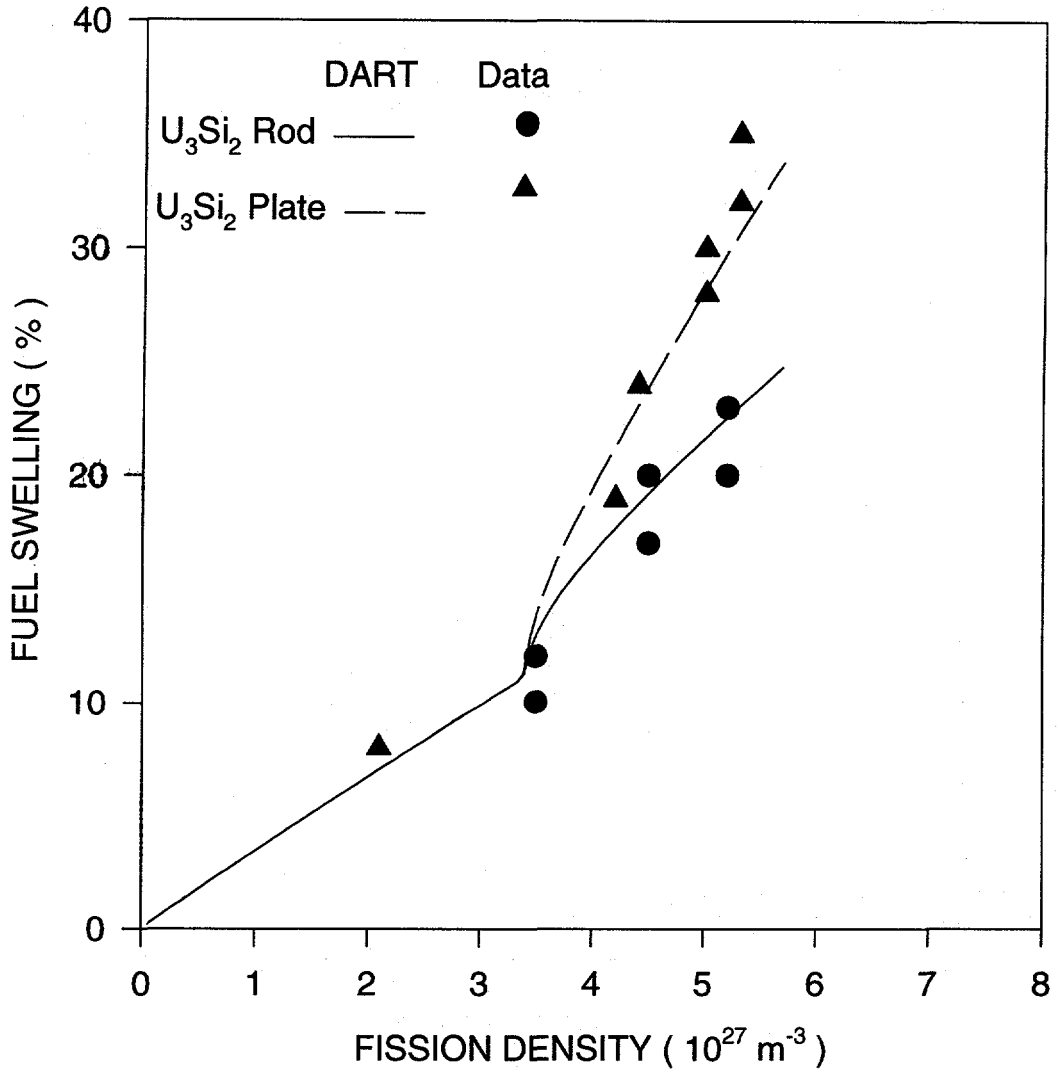

Fig. 12. DART-calculated results for fuel particle swelling of low-enriched U_3Si_2-Al fuel plates and rods as a function of fission density

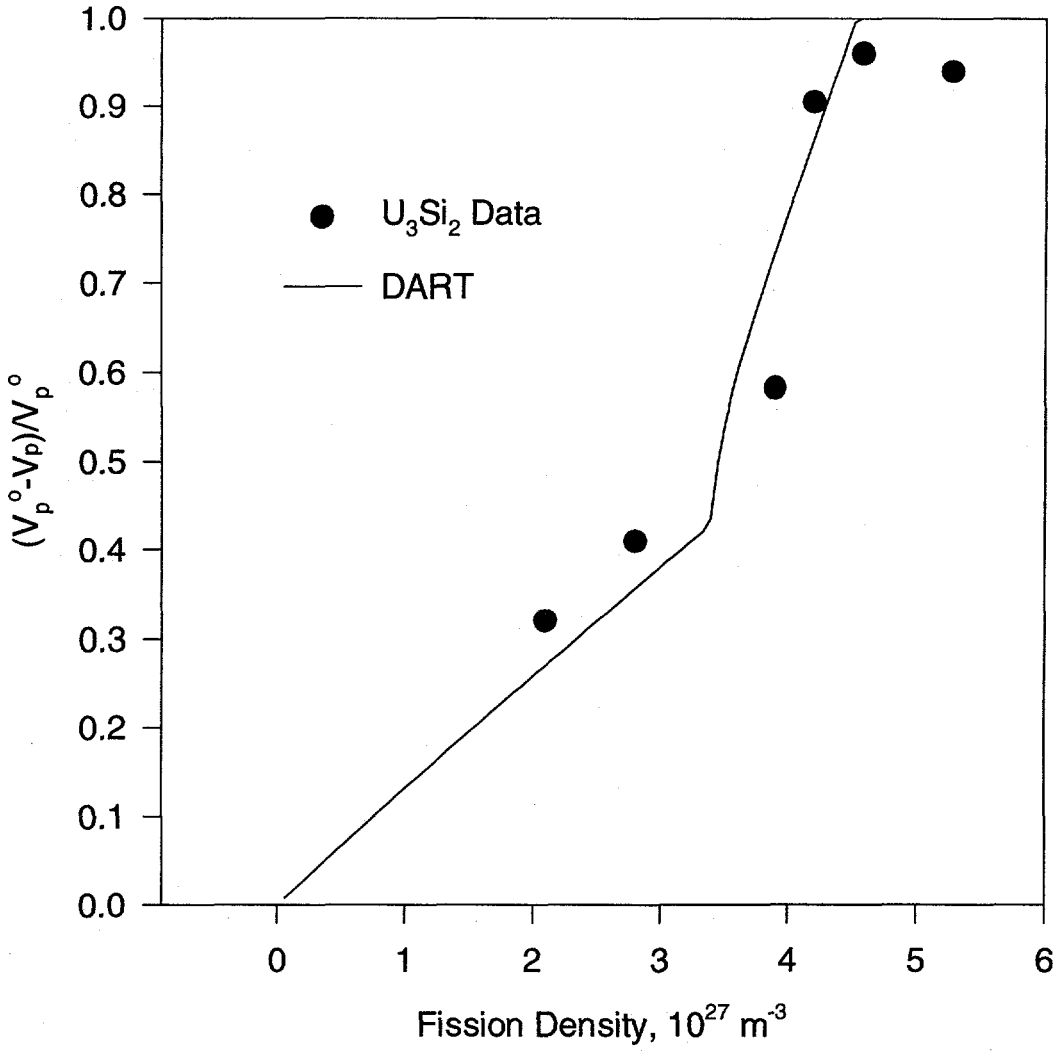

Fig. 13. DART-calculated results for pore closure of low-enriched U_3Si_2 fuel plates as a function of fission density compared with the measured values

11 DART Calculation of Dispersion Fuel Thermal Conductivity

Figures 14 and 15 show the results of DART calculations of the bulk thermal conductivity and total fuel swelling, respectively, of a 3.5-g/cm^3 35% enriched U_3Si_2 dispersion fuel containing 3.5% as-fabricated porosity for four values of fuel temperature. The calculations shown in Figs. 14 and 15 utilized a one-node mesh across the fuel plate, and a 20-node mesh across the fuel particle.

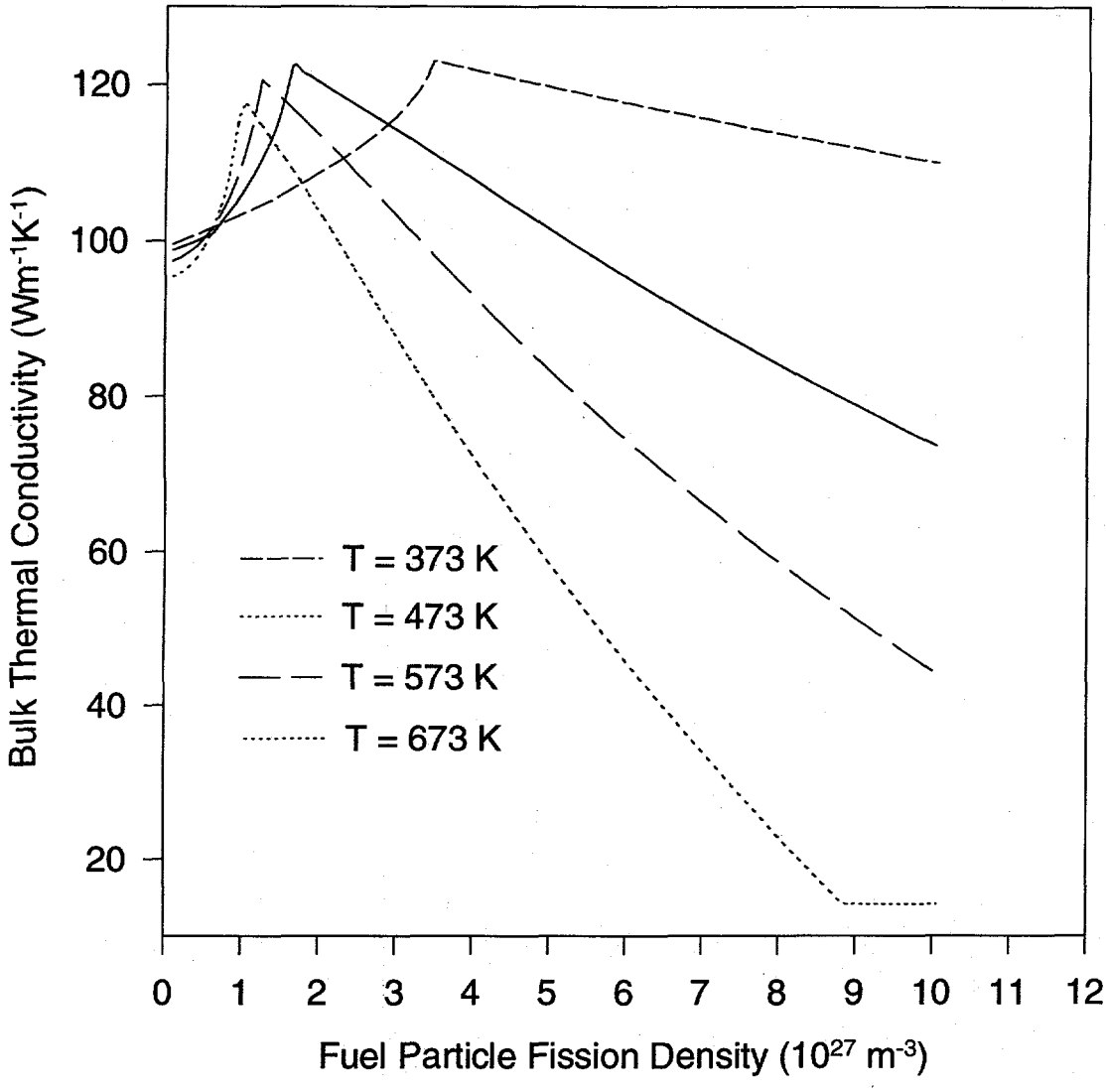

Fig. 14. DART calculated bulk thermal conductivity of a 3.5-g/cm^3, 35% enriched U_3Si_2 dispersion fuel containing 3.5% as-fabricated porosity, at four fuel temperatures

Each thermal conductivity curve shown in Fig. 14 exhibits a characteristic shape: initially, the thermal conductivity increases because of pore closure in response to fuel particle swelling; this is followed by a decrease in the thermal conductivity due to additional fuel particle swelling and a commensurate decrease in the volume fraction of aluminum; subsequently, an accelerated decrease in the thermal conductivity occurs because of the onset of grain subdivision, which leads to higher fuel particle swelling rates (see Fig. 15). Two predictions of the

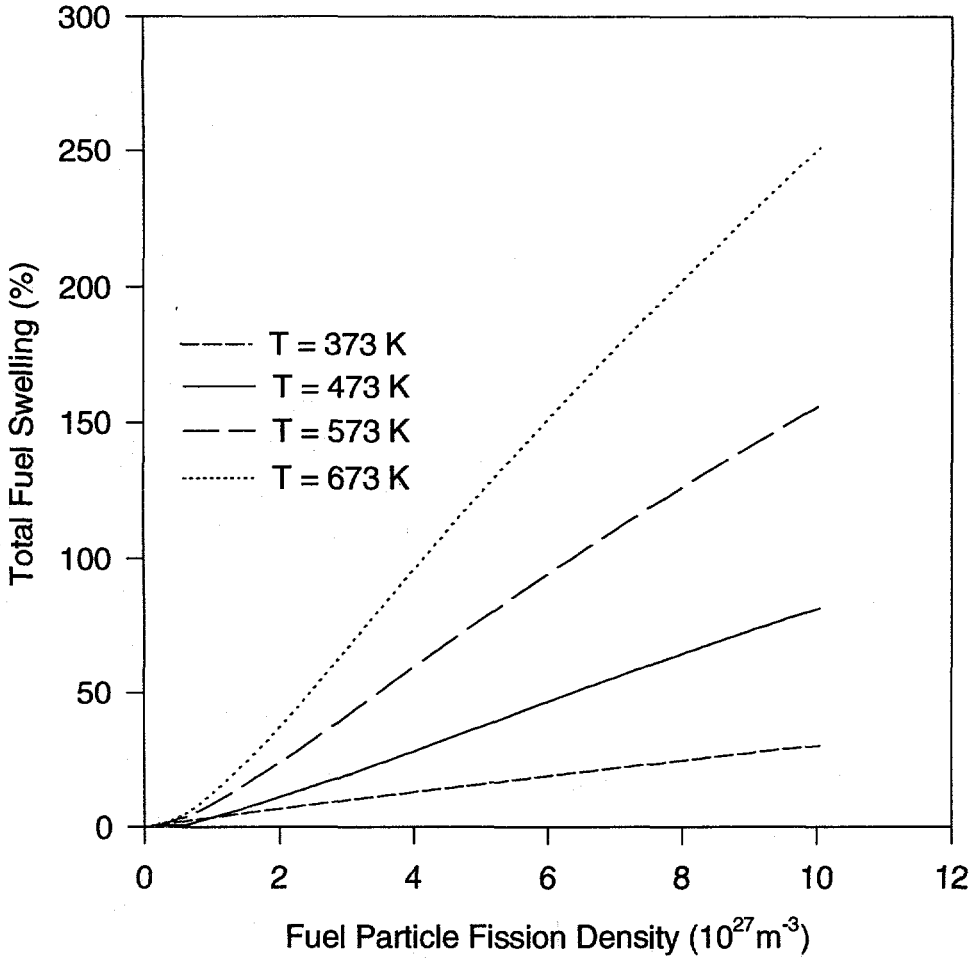

Fig. 15. DART calculated total fuel swelling (%) of a 3.5-g/cm^3, 35% enriched U_3Si_2 dispersion fuel containing 3.5% as-fabricated porosity, at four fuel temperatures

temperature dependence of the thermal conductivity are shown in Fig. 14. First, for the initial phase of the irradiation that includes pore closure (up to the onset of grain subdivision), lower thermal conductivities are predicted for the irradiations at higher temperatures because of aluminide formation. Aluminide formation is faster at higher temperatures and results in an increase in fuel swelling (see Fig. 15) because the density of the aluminide is reduced beyond that of the original U_3Si_2 . Second, for a constant fission rate, grain subdivision is predicted to occur earlier for irradiations at higher temperatures. As the swelling rate increases upon grain subdivision (see Fig. 15), the thermal conductivity starts an accelerated decrease earlier at the higher temperatures. This behavior is shown more clearly in Fig. 16, where the DART-calculated bulk thermal conductivity and total

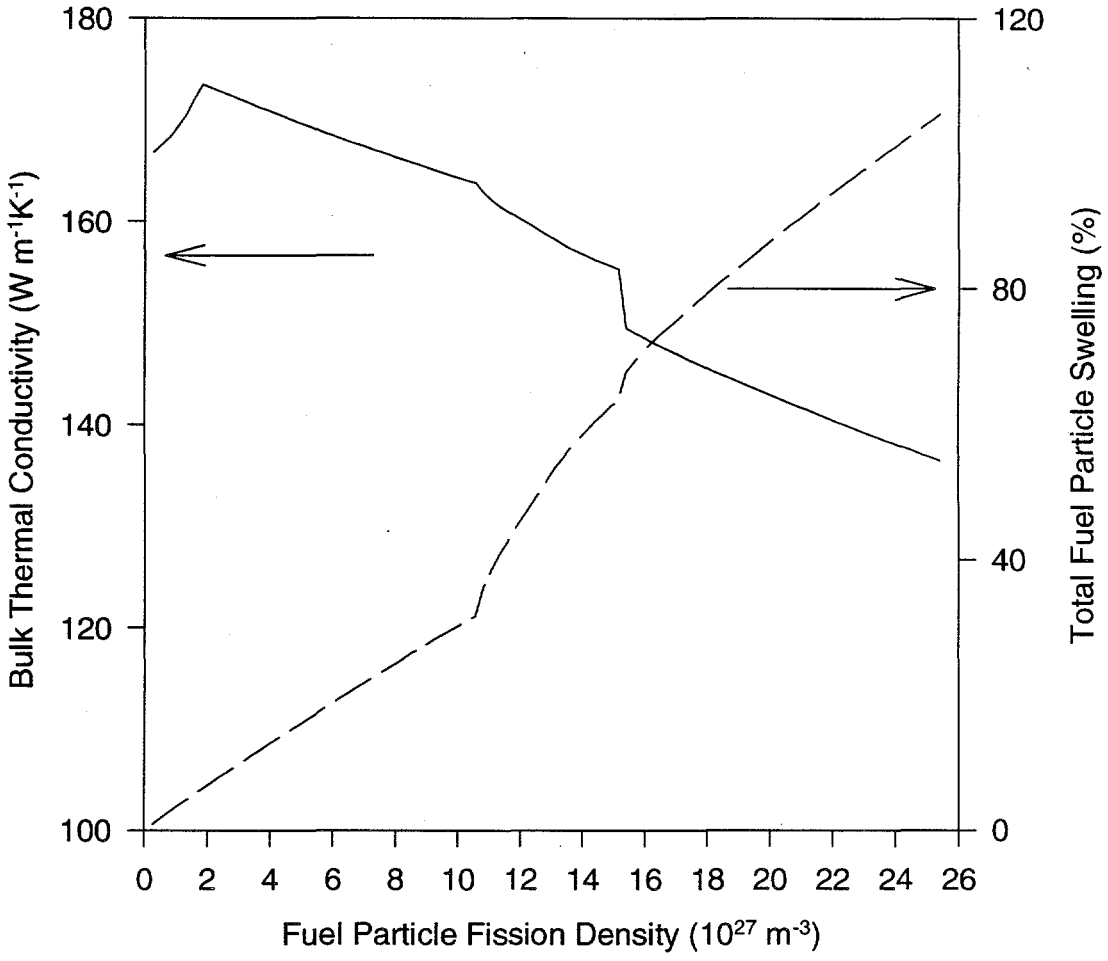

Fig. 16. DART-calculated bulk thermal conductivity and total fuel swelling of a 1.3-g/cm^3, 92.5% enriched U_3Si_2 dispersion fuel containing 0.7% as-fabricated porosity, irradiated at 373 K

fuel swelling of a 1.3-g/cm^3, 92.5% enriched U_3Si_2 dispersion fuel containing 0.7% as-fabricated porosity are exhibited. As is clear from Fig. 6, increased fission rates (enrichments) result in higher thermal conductivity predictions (all other conditions remaining constant) because of the delay in the onset of grain subdivision. The calculations shown in Fig. 16 were performed at a constant fuel temperature of 373 K, and utilized a one-node mesh across the fuel plate, and a 20-node mesh across the fuel particle.

As described above, the thermal conductivity curve shown in Fig. 16 exhibits a characteristic shape: initially, the thermal conductivity increases as pore closure occurs; this is followed by a decrease in the thermal conductivity due to fuel particle swelling, an accelerated decrease in the thermal conductivity due to the onset of grain subdivision (grain refinement leads to higher fuel swelling rates); and, finally, at high burnup, we observe an additional accelerated decrease in the thermal conductivity due to the transformation of the interior of the fuel particles to an unstable phase (e.g., see Fig. 10).

Appendix A: DART Input Description

Figure A-1 shows a typical DART input file: this file was used to generate Fig. 15. Table A-1 describes the driver input for DART.

```
$ ************************************************
$ INPUT DECK FOR DARTC
$ ************************************************
$ job title                                    irstar
HIFR IRRADIATION SIMULATION U3SI2, .....          0
$
hifrr    hifrw
$
$  grs    fl    igs   nf  lf   kf   idis    nxi
   0.0   0.10   1     1   1    5      0    1 0 1 1
$
$ prog changes
$   i      PROG(i)
   47       0.05
   48       0.932
   49    2.2285d-23
   50       12.2
   83     1938.d0
   86     253.667
  118        7.5
  195        10.
  233         1.
    0         0
$
$  geom     =1. :rod     =.5 :plate
   0.5
$
$   prsol     vfm0     vpm0      tmtp      cvf0  poros
    15.       .122     .007     .384615     0.68   .02
$
$  fuel radii
$    rs(cl)   rs(s)
     0.       0.15
$
$  pellet radii
$    rs(cl)   rs(s)
     0.       0.005
$
$   grain diameter, grsk
    5*1.0E-2
$
$    the following indices for variables to be plotted must be read in
$    the same order as done in the calculations.  This means that k's
$    are read in descending order, the l's in ascending order.
$
$ read in k,l,file name for k,l results$
```

Fig. A-1. Typical DART input file

```
$ k  l  file
$  3  1  'dump3'
   1  1  'dump1'
  0  0  ''
$
$ read in k,l,file name for specified distributions
$ k  l  file
  1  1  'd1'
  0  0  ''
$
$ read in l, file name for l results
$
$ l   file
  0   ''
$
$ read in l, file name for l distributions for each type of region
$
$ l  file
  0  ''
$
$ read in  file name for j results
$
  'dartj'
$
$   delt  nprint  iread  ip  irstar  itran  nopt   nxo
  1.3e5   1          1    1   0       0     0      1
$
$   nx1     nx2     nx3     nx4     nx5
    1         1       0       0       1
$
$   boundary temperatures
$    ts(cl)     ts(s)
    373.0      373.0
$
$   power, pow
    0.16588
$
$    tmax    iprint iwrite ipow
   1.3e7         1      4       0
$
$    td(cl)   td(sf)
      0.     0.
$    dpow
      0.
$
$   delt  nprint  iread  ip  irstar  itran  nopt   nxo
     0.     0       0     0   0       0      0      0
0       0     0
```

Fig. A-1. continued

Table A-1. Description of driver input for DART

Input No.	Variable Name	Description	
1			
	ITLE	descriptive title	
	IRSTAR	IRSTAR = 0:	Normal execution
		IRSTAR = 1:	Problem restart; program reads restart dump from Unit 15
2			
	DUMP1	Defines Unit 15 for reading restart dump (PC version only)	
	DUMP2	Defines Unit 16 for writing restart dump (PC version only)	
3			
	GRS	Initial amount of gas in fuel/cladding gap.	
	FL	Fuel rod length (cm)	
	IGS	IGS = 1,2,3: equation of state for Xe, Kr, or Ar	
	NF	Total number of vertical sections in plate or axial sections in rod	
	LF	Total number of horizontal sections in plate or radial rings in rod	
	KF	Total number of radial rings in fuel particle; each ring has a K value (1 inner to KF outer)	

IDIS	IDIS = 0;	Crystalline fuel
	IDIS = 1;	Amorphous fuel
NXI(I)	I = 1,2,3,4: bulk, dislocation, face, and edge.	NXI = 0: Don't calculate NXI = 1: Calculate

4

I PROG(I) Identifier	This card set provides the capability of modifying any member in labelled COMMON/ PROG/PROG(250). Last card of this set must have I = blank or zero. This card set is read in subroutine ZRDWR.

5

GEOM	GEOM = 0: Plate
	GEOM = 1: Rod

6

PRSOL	External pressure (PSI)
VFMO	Fuel volume fraction
VPMO	As-fabricated pore volume fraction
TMTP	Ratio of the bulk thickness to the plate thichkness
CVF0	Cladding volume fraction

	POROS	Initial porosity in fuel particle
7		
	RS(cl), RS(s)	Position of plate (rod) center and surface (cm)
8		
	RS(cl), Rs(s)	Radius of fuel particle center and surface (cm)
9		
	GRSK	Grain diameter (cm) of each K node
10		
	k l "name"	Read in k, l, file name for k, l results
11		
	k l "name"	Read in k, l, file name for specified distributions
12	l "name"	Read in l, file name for l results
13		
	l "name"	Read in l, file name for l distributions for each region type

14

"name"	Read in file name for j results	

15

DELT	Time step (s)	
NPRINT	Printout option	
	NPRINT = 1:	No printout
	NPRINT = 2:	Partial printout for axial totals and rod totals only
	NPRINT > 2:	Full printout
IREAD	IREAD = 0:	No change operating conditions for this time step
	IREAD = 1:	Fuel operating conditions to be updated for this time step; read in inputs #17-18
		IP IP = 0: No action
	IP = 1:	Read in inputs #19-21
IRSTAR	IRSTAR < 0:	Halt calculation, write restart dump on Unit 16, write summary printout
	IRSTAR > 2:	Read in new Prog Array values with same format as input #4
	IRSTAR = other	No action
ITRAN	ITRAN = 0:	Steady–state mode
	ITRAN ≠ 0:	Transient Mode

	NOPT	NOPT = 0:	No grain growth/grain boundary sweeping
		NOPT = 2:	Theoretical grain growth law
		NOPT = 3:	Empirical grain growth law
	NX0	NX0 = 0:	No writes to data files
		NX0 = 1	Read in input #16
16			
	NX1	Write k, l results every NX1 time steps	
	NX2	Write specified k, l distributions every NX2 time steps	
	NX3	Write l results every NX3 time steps	
	NX4	Write specified l distributions every NX4 time steps	
	NX5	Write j results every NX5 time steps	
		If IREAD = 0 skip inputs #17-18	
17			
	TS(cl) TS(S)	Temperatures at boundaries of regions	
18	POWER, POW	Linear power in j sections (kW/ft)	
		If IP = 0, skip input #19-21	
19			
	TMAX	The code will execute until the total time = TMAX	

	IPRINT IWRITE	Printout for every IPRINT time steps with NPRINT = IWRITE
	IPOW	IPOW = 0: Do not read in POW(J) IPOW = 1: Read in POW(J)
20	TD(cl) TD(s)	Temperatures TS(cl) and TS(s)) incremented by TD during DELT
21	DPOW	Power incremented by DPOW during DELT If IPOW = 0, skip Input #22
22	POW	Linear power in section J (kW/ft)

Repeat sequence starting with Input #15

Appendix B: Dictionary of Variables in COMMON/PROG/PROG(250)

Table B-1 lists the symbols and values of variables in COMMON/PROG/PROG(250), whereas Table B-2 lists the definitions of these variables.

Table B-1. Symbols and values of variables in COMMON/PROG/PROG(250)

a(1) = -57.364866
a(2) = -7.0264645
a(3) = .52281105
a(5) = 2.9969484e4
a(6) = -2.07175e3
a(7) = -1.4947535e8
a(8) = -3.0994649e7
a(9) = 2.0330226e6
aadc1 = xaadc1(1)
aadc2 = xaadc2(1)
acon = 2.37
alfa = .5
astar = .907
atmvol = 4.09e-23
avn = 6.02252e23
badc1 = 8.12664962e-10
badc2 = 108000.d0
badc3 = 3.5e-31
prog(20) = badc4
badc4 = 0.d0
badc5 = 2.09160553
badc6 = 6.78473797e3
boltz = 1.38e-16
bvcrit = .055
calca = 3.e-2
cd = 2.e-5
crt = 3.5e-5
cr1 = 3.e-7
delhv = 5.96e12
prog(30) = du1(1)
du1(1) = xdu11(1)
du1(2) = 3.1e-8
du1(3) = .01
du1(4) = .01
du2(1) = 6.5e4
du2(2) = 2.4e4
du2(3) = 5.4493e4
du2(4) = 5.4493e4
dzero = 57.e4
epsb = zeps(igs)
prog(40) = fawge
fawge = 14.
ffm = 7.
ffn = 12.
fgpf(1) = .31
fgpf(2) = 1.d0
fgpf(3) = time (sec) after which debugging printout is given
fgpf(4) = initial h (sec) = 1.
fgpf(5) holds factor for burnup depletion
fgpf(5) = 0.d0
fgpf(6) holds the enrichment
fgpf(6) = 1.d0
fgpf(7) holds solid fission product swelling parameter
fgpf(7) = .22285d-22
prog(50) = fgpf(8)
fgpf(8) holds theoretical fuel density
fgpf(8) = 12.20d0
fgpf(9) holds xkal term
fgpf(9) = 218.485d0
fprso = 0.d0
fn = xfn(1)
gammal = 450.d0
gbr(1) = 1.d0
gbr(2) = 0.d0
gbr(3) = 0.d0
g1 = computed
g2 = 0.
prog(60) = pds
pdsc = 68947.
ptpl = .08
pzero = 1.64e14
qs = 4.52e12
qsstar = .69466e-11
qvstar = 4.8e-12
rcv = 1.98586
redis = 1.e-6
rescon = 2.e-17
prog(70) = rg
rg = 8.31e7
rhol = 0.d0
rlams = 1.12e-6
sbcf = 100.d0
sig = 3.e-8
sigma = zsgm(igs)
sigpi = .020
tc = ztc(igs)
theta = .8203
tkauml = 3123.
prog(80) = tkdis
tkdis = 2650.d0
tkliq = 2170.d0
tksol = 1373.
upg = 1938.d0
vc = zvc(igs)
vis = 1.e-2
wm1 = 253.667d0
wm2 = 132.
xdl(1) = 3600.d0
xdl(2) = 1.
prog(90) = xdl(3)
xdl(3) = 1.d-5
xkp = 1.
xk1(1) = 1.46e-4
xk1(2) = 3.5e-5
xk2(1) = 3.21e4
xk2(2) = 2.215e4
xk3(1) = 1.e12
xk3(2) = 1.e12
xk4(1) = 4.25e4
xk4(2) = 3.5e4
prog(100) = xk4
xk4c = 1.2
xmlt = 1.e-4
xmltc = 0.d0
zcon(1) = 1.e-3
zcon(2) = 0.d0

vda = 2.9e-26
vdrho = 1.e9
vdb = 2.375e-8
vdqu = 131786.
vdql = 4.5
prog(110) = gc
gc = 8.5e-23
fef = 1.d-7
xku = 14.8d0
xkf(1-5) are coefficients determined by minitab
xkf(1) = 1.d0
xkf(2) = -1.d0
xkf(3) = 1.d0
xkf(4) = -1.d0
xkf(5) = -.63902d0
syf = 7.5d0
sig1 = 1.d0
prog(120) = sig3
sig3 = 1.d0
zz1 = 10000.d0
hfac(1) = 1.25d0
hfac(2) = 1.15d0
hfac(3) = 1.05d0
hfac(4) = 1.005d0
hfac(5) = 1.d0
hfac(6) = .995d0
hfac(7) = .985d0
hfac(8) = .95d0
prog(130) = hfac(9)
hfac(9) = .9d0
fexp = 1.d0
rnod = unused
geomy = unused
prog(134-186) are unused in this version
prog(187) = rhodsl
rhodsl = 1.d9
aagc1 = xaagc1(1)
aagc2 = xaagc2(1)
prog(190) = epsj
epsj = 1.d12
ffdslc = 10.d0
fodslc = .31831d0
fogbdy = .63662d0
gbs2 = .5d0*1.43d-4
rm = 10.d0
tkcr = 2373.d0
fnn(1) = 1.d0
fnn(2) = 2.d-7
fnn(3) = 2.d-7
prog(200) = avi
avi = .1d0
b1 = 6.d17
ei = .2d0
esf = 0.70d0
ev = .9d0
evi = 1.3d0
e3v = 1.3d0
e4v = .9d0
riv = 2.d-8
rsi = 2.d-8
prog(210) = rsm
rsm = 3.d-8
tmr = 1.5d0
xi = 1.0.d-6
xni = 5.d14
xnv = 5.d13
zb = 2.d0
grdx = 1.d-4
usr(1) = 1.5d0
usr(2) = 2.6d22
prog(220) = usr(3)
usr(3) = .625d0
usr(4) = 1.d-5
usr(5) = 3.d0
usr(6) = 4.d22
usr(7) = 1.5d0
sy0fp = 200.d0
tkdx = 1000.d0
dal0 = 42.d0
epsal = 6.d4
adp = 1.7d0
prog(230) = adpl
adpl = .5d0
tsw33 = .3333333d0
xalm = 0.d0
xpand = 1.d0
xicl = 0.d0
tamorf = 723.d0
prog(236-250) unused

Table B-2. Definition of variables in COMMON/PROG/PROG(250)

Index	Name	Definition
1 – 9	A(1–9)	Parameters in the calculation of fuel yield strength
10	AADC1	Preexponential factor for gas atom diffusion coefficient (cm^2/s)
11	AADC2	Activation energy for gas atom diffusion (cal)
12	ACON	Parameter that relates grain boundary area per unit volume to the equivalent grain diameter
13	ALFA	Unused
14	ASTAR	Fraction of areal coverage of grain face by bubbles required for channel formation
15	ATMVOL	Volume associated with one molecule of fuel (cm^3)
16	AVN	Avogadro's number
17–22	BADC(1–6)	Coefficients in the semi–empirical/ phenomenological expression for intragranular bubble diffusivities
23	BOLTZ	Boltzmann's constant (ergs/K)
24	BVCRIT	Critical value of grain edge swelling required for long–range tunnel interlinkage
25	CALCA	Unused
26	CD	Unused
27	CRT	Relative error permitted in the integration

28	CR1	Relative error permitted in the bubble radius calculation
29	DELHV	Molar heat of vaporization (ergs/mole)
30 31	DU1(1) DU1(2)	Preexponential factors in expression for vacancy diffusion, in lattice (1) and in faces and edges (2) (cm^2/s)
32	DU1(3)	Not used
33	DU1(4)	Not used
34	DU2(1)	Activation energy for vacancy diffusion corresponding to DU1(1) above (cal)
35	DU2(2)	Activation energy for vacancy diffusion corresponding to DU1(2) above (cal)
36	DU2(3)	Unused
37	DU2(4)	Unused
38	DZERO	Preexponential factor in the expression for surface diffusion of UO_2 (cm^2/s)
39	EPSB	Parameter for the modified hard–sphere equation of state
40	FAWGE	Average number of grain faces per grain
41	FFM	Parameter for the modified hard–sphere equation of state
42	FFN	Parameter for the modified hard–sphere equation of state
43	FGPF(1)	Number of noble gas atoms produced per fission event

44	FGPF(2)	Parameter that sets when the number of size classes should be increased
45	FGPF(3)	Time after which debugging printout is given (s)
46	FGPF(4)	Initial value of the internal time step h (s)
47	FGPF(5)	Factor for power depletion as a function of burnup
48	FGPF(6)	Fuel enrichment
49	FGPF(7)	Solid fission product swelling parameter
50	FGPF(8)	Theoretical fuel density
51	FGPF(9)	Temperature-indepentdent term in the expression for thermal conductivity of aluminum
52	FPRS0	External hydrostatic stress on the fuel particle
53	FN	Probability that two colliding atoms stick together to form a bubble nucleus
54	GAMMAL	Surface energy of a liquid/vapor interface (erg/cm^2)
55	GBR(1)	Multiplies RESCON to obtain effective irradiation–induced re-solution of gas atoms from grain face and edge bubbles, respectively
56-57	GBR(2-3)	Unused
58–59	G1,G2	Coefficients in the expression for fuel surface energy
60	PDSC	Converts hydrostatic stress from lbs/sq in. to $dynes/cm^2$
61	PTPL	Porosity values > PTPL contribute to the amount of open porosity

62	PZERO	Preexponential in the expression for the vapor pressure of the fuel (dynes/cm^2)
63	QS	Activation energy for surface diffusion (ergs/mole)
64	QSSTAR	Heat of transport for surface diffusion (ergs)
65	QSURF	Activation energy for surface diffusion (cal)
66	QVSTAR	Heat of transport for the volume diffusion mechanism (cal)
67	RCV	Universal gas constant, R (cal/K)
68	REDIS	Average distance traveled by an atom ejected from a grain boundary bubble (cm)
69	RESCON	Re-solution constant (cm^3)
70	RG	Gas constant (ergs/[gmol•K])
71	RHOL	Liquid density (g/cm^3)
72	RLAMS	Proportional to gas atom jump distance (cm)
73	SBCF	Width of probability distribution for grain-face channel formation
74	SIG	Average collision diameter of fuel and Xe molecules (cm)
75	SIGMA	Parameter for the modified hard-sphere equation of state
76	SIGPI	Width of probability distribution for grain edge porosity interlinkage
77	TC	Parameter for the modified hard-sphere equation of state

78	THETA	Twice THETA is the dihedral equilibrium angle that a gas bubble makes with the grain boundary
79	TKAUML	Unused
80	TKDIS	Unused
81	TKLIQ	Unused
82	TKSOL	Unused
83	UPG	Melting temperature of the fuel
84	VC	Parameter for the modified hard-sphere equation of state
85	VIS	Viscosity of liquid or liquidlike material (g/s•cm)
86	WM1	Molecular weight of fuel
87	WM2	Molecular weight of Xe
88	XDL(1)	Maximum size of time step h used internally during steady state (s)
89	XDL(2)	Maximum size of time step h used internally during transient (s)
90	XDL(3)	Maximum size of time step h used immediately after amorphization (s)
91	XKP	Ratio of the thermal conductivity of a pore to the thermal conductivity of fuel
92	XK1(1)	Nominal value of parameter in grain growth model, NOPT = 2
93	XK1(2)	Unused

94	XK2(1)	Nominal value of parameter in grain growth model, NOPT = 2
95	XK2(2)	Unused
96-97	XK3(1-2)	Nominal value of parameters in grain growth model, NOPT = 3
98-99	XK4(1-2)	Nominal value of parameters in grain growth model, NOPT = 3
100	XK4C	Unused
101	XMLT	Maximum radius of bubbles on faces
102	XMLTC	Unused
103	ZCON(1)	Unused
104	ZCON(2)	Unused
105	VDA	Unused
106	VDRHO	Unused
107	VDB	Unused
108	VDQU	Unused
109	VDQL	Unused
110	GC	Van der Waals constant
111	FEF	Thickness of grain boundary (cm)
112	XKU	Thermal conductivity of unirradiated fuel
113-117	XKF(1-5)	Coefficients in expression for thermal conductivity of the dispersion fuel

118	SYF	Phenomenological factor β in the expression for interface pressure; introduced to account for the effects of irradiation
119	SIG1	Unused
120	SIG3	Unused
121	ZZ1	Enhancement factor in the expression for irradiation-enhanced diffusion of gas atoms on the grain boundaries
122-130	HFAC(1-9)	Parameters used in the time-step algorithm
131	FEXP	Parameter that determines the temperature interpolation method given the suface and center temperatures
132	RNOD	Unused
133	GEOMY	Unused
134-186		Unused
187	RHODSL	Dislocation density (cm^{-1})
188	AAGC1	Parameter in the expression for the grain boundary bubble diffusion coeficient
189	AAGC2	Parameter in the expression for the grain boundary bubble diffusion coeficient
190	EPSJ	Parameter that sets when the number of size classes should be increased
191	FFDSLC	Enhancement factor in the expression for the gas atom diffusion coeficient on dislocations
192	FODSLC	Parameter in the expression for the velocity of a dislocation bubble moving in a temperature gradient
193	FOGBDY	Parameter in the expression for the velocity of a grain boundary bubble moving in a temperature gradient

194	GBS2	Paramter in the expression for the force on a dislocation bubble in a temperature gradient required to drag the dislocation dipole
195	RM	Factor by which the number of atoms in a bubble size class differs from the numbers in the adjacent size classes
196	TKCR	Minimum temperature required for a dislocation bubble in a temperature gradient to drag the dislocation dipole
197	FNN(1)	Nucleation factor for bubbles in the bulk material and on dislocations
198	FNN(2)	Nucleation factor for bubbles on grain faces
199	FNN(3)	Nucleation factor for bubbles on grain edges
200	AVI	Preexponential factor that accounts for deviations from diffusion in a pure solvant
201	B1	Conversion factor
202	EI	Interstitial migration energy
203	ESF	Sum of stored and formation energy of a viable nucleus
204	EV	Vacancy migration energy
205	EVI	Migration energy of a vacancy-solute pair
206	E3V	Energy in the expression for the jump rate of vacancies away from nearest-neighbor nuclei of solvent atoms
207	E4V	Energy in the expression for the jump rate of vacancies towards nearest-neighbor nuclei of solvent atoms
208	RIV	Radius of recombination volume
209	RSI	Annihilation radius for defects with sinks
210	RSM	Annihilation radius for vacancy-solute pair

211	TMR	Unused
212	XI	Solute concentration
213	XNI	Vibration-frequency factor for interstitials
214	XNV	Vibration-frequency factor for vacancys
215	ZB	Parameter in the expression for the radiation-enhanced diffusion coefficient
216	GRDX	Diameter of recrystallized grains (cm)
217-224	USR(1-7)	Parameters in the expression for the fission density at which U_3Si_2 enters an unstable phase field
225	SY0FP	Effective yield strength of fuel
226	TKDX	Temperature above which the fuel recrystallizes
227	DAL0	Preexponential factor in expression for thermal diffusivity of aluminum
228	EPSAL	Migration energy in expression for thermal diffusivity of aluminium
229	ADP	Parameter in expression for thermal diffusivity of aluminium
230	ADPL	Parameter in expression for thermal diffusivity of aluminium
231	TSW33	Fractional density increase upon formation of aluminide
232	XALM	Unused
233	XPAND	If nonzero, phase boundaries within fuel particle move in response to fuel swelling

234	XICL	Flag for different types of aluminum: XICL = 0: 1100-0 Al XICL = 1: 6061-0 Al
235	TAMORF	Temperature above which the fuel cannot become amorphous
236-250		Unused

Appendix C: DART Output Description

The first part of DART output consists of a listing of the input file and a listing of the PROG array. Figure C-1 shows the remainder of a typical DART output file and Table C-1 lists definitions of these output quantities.

```
bvsl= 7.4870207E-04 avsl= 7.4870204E-04 rggb= 9.9999996E-01  rgb= 1.5706032E-11 bulkfr=9.9999996E-01 bvvol= 0.0000000E-01
bvsf= 2.8506440E-11 avsf= 2.8506218E-11 rggf= 3.8074381E-08  rgf= 5.9799747E-19 facefr=3.8074381E-08  fbden= 2.1458039E-09
bvse= 1.4884057E-12 avse= 1.4843052E-12 rgge= 1.9858803E-09  rge= 3.1190301E-20 edgefr=1.9858803E-09

 bvs= 7.4870210E-04  avs= 7.4870207E-04 rggl= 9.9999996E-01 eprf= 3.6828315E-20  prf= 2.9797632E-03 egre= 2.1695985E-04
 ncdi  ncfi  ncei  imx1  imx2     gamma        rpin          gbs
   0    4     4    12    13    6.2056E+02  3.4992E-08 0.0000E-01
     sfps          tswl          fdnts          voltp          xkug          wkpar       vfma
 1.29766E-03 2.04636E-03 1.51667E+22 5.85392E-12     1.46883E+01 -3.55401E-02 0.00000E-01

     fden          fdx           tst1           tst2           cv            ci
 5.82303E+19 3.00170E+21 3.34236E+05 4.29732E+05 1.18443E-07 3.54576E-11

      j    l    k  ldmk     fgrk          gsgen         gout          ret           bvs           prso          errk          tki
      1    1    1    0    3.6535E-09 1.5706E-11 5.7382E-20 1.5706E-11 7.4870E-04 1.3391E+03 1.6050E-10 3.7300E+02

      j    l  nmxj  nmax      fgrl          gsgk          gouk          retk          bvlk          tswlk         errl          bupl
      1    1   60    4     3.6535E-09 1.5706E-11 5.7382E-20 1.5706E-11 7.4870E-04 2.0464E-03 1.6050E-10 1.0155E-02
                 h            hnxt         rs(kf1)       rsl(l+1)      ydep          vlml          prsol         sy0
           1.4646E+03 1.4719E+03 5.0034E-03 1.5000E-01 -9.0639E-06 9.0000E-03 1.3391E+03 6.1878E+02

     vfm           vam           cvf                vpm          dtptp         xkdis         xku3si2       xku0          xkxku         xkgxku
 1.05816E-01 2.11200E-01 6.70000E-01 1.29839E-02 -7.56637E-03 9.79017E+01 1.46883E+01 9.77683E+01 1.00137E+00 9.92456E-01

      j          dtpj          fgrj          gsgj          gouj          retj          bvsj          tswj          errj          xkdsj
      1     -7.5664E-03 3.6535E-09 1.5706E-11 5.7382E-20 1.5706E-11 7.4870E-04 2.0464E-03 1.6050E-10 9.7902E+01

                    fgrt          gsgt          gott          rett          rrcon         err
                  3.6535E-09 1.5706E-11 5.7382E-20 1.5706E-11 1.3048E-14 1.6050E-10

            ********** end of grass output for this time step **********
```

Fig. C-1. Continued

```
****************** grass output **********************

                          time= 2.800000000E+05
ts(k,j)=      3.7300E+02    3.7300E+02
tk(k,j)=      3.7300E+02

------ axial section=  1 radial section=  1  1

rs(k,j)= 0.000000E-01 rs(k+1,j)= 5.003390E-03 ts(k,j)= 3.730000E+02 ts(k+1,j)=3.730000E+02 poros =  0.000000E-01
delt  = 2.800000E+05 volume  = 5.246647E-07 area  = 0.000000E-01 prfold = 2.979763E-03 ratio =  5.000000E-01

tk= 3.73000E+02 tgrad= 0.0000E-01 dtdt= 0.0000E-01 tfpv=2.0770E+14 gsin=6.4388E+13 grd=1.0000E-02 dcie=7.2696E-17 prsoo=1.3391E+03

      savg          rad          bdsurf        bvmodl        bdmodl        betab         flux/rbf3 rbl3/pbkgby rbd3/rrgbip
 1.00000E+00 2.14808E-08 1.39135E-36 0.00000E-01 7.26956E-17 0.00000E-01 3.00113E+09 4.91229E-02 0.00000E-01
 1.00000E+00 2.14808E-08 1.39135E-36 0.00000E-01 7.26956E-13 4.74694E-06               0.00000E-01 0.00000E-01
 1.00000E+00 2.14808E-08 1.39135E-36 0.00000E-01 7.26956E-13
 1.00000E+01 4.85790E-08 2.72045E-37 0.00000E-01 7.91341E-42 0.00000E-01 1.41453E-24 1.68354E-04 0.00000E-01
 1.00000E+01 5.07949E-08 2.48827E-37 0.00000E-01 2.48827E-37 6.84397E-08               0.00000E-01 0.00000E-01
 1.00000E+01 5.24724E-08 2.33171E-37 0.00000E-01 2.33171E-37
 1.00000E+02 1.10196E-07 5.28700E-38 0.00000E-01 1.42675E-42 0.00000E-01 3.71083E-60 9.32320E-16 0.00000E-01
 1.00000E+02 1.15397E-07 4.82110E-38 0.00000E-01 4.82110E-38 7.85767E-08               0.00000E-01 0.00000E-01
 1.00000E+02 1.19305E-07 4.51046E-38 0.00000E-01 4.51046E-38
 1.00000E+03 2.50392E-07 1.02399E-38 0.00000E-01 2.56319E-43 0.00000E-01 0.00000E-01 0.00000E-01 0.00000E-01
 1.00000E+03 2.62501E-07 9.31701E-39 0.00000E-01 9.31701E-39 4.17165E-08               0.00000E-01 0.00000E-01
 1.00000E+03 2.71618E-07 8.70204E-39 0.00000E-01 8.70204E-39
 6.60179E+04 1.11879E-06

distributions follow (number/cm**3)
bulk region 1   1.803E+19 6.310E+10   9.280E-25   0.000E-01
face region 1   6.866E+11 1.485E+05   1.892E+04   2.418E+02
edge region 1   3.575E+10 2.534E+06   3.249E+05   3.052E+03
corn region 1   9.980E+05
```

Fig. C-1. Typical DART output file

Table C-1. Definition of DART output quantities

NPRINT = 1: No output
= 2: Limited output
> 2: Full output

AREA	Surface area of region (K,J) (cm^2)
AVS	Sum of AVSL, AVSF, and AVSE
AVSL	Fractional swelling in region (L,K,J) due to gas atoms in the lattice
AVSF	Fractional swelling in region (L,K,J) due to gas atoms on the grain faces
AVSE	Fractional swelling in region (L,K,J) due to gas atoms on the grain edges
BDMODL(N)	Diffusion coefficients of atoms (N =1) and bubbles (N>1) (cm^2/s)
BDSURF(N)	Diffusion coefficients for bubble movement, based on surface diffusion (cm^2/s)
BETAB(N)	Intragranular bubble nonequilibrium parameter
BULKFR	Fraction of generated gas residing in the grain lattice
BULK REGION K	Gas bubble concentration in each size class for bubbles in the grain lattice ($\#/cm^3$)
BUPL	Fractional burnup
BVLK	Swelling strain in section (J,L) due to gas bubbles
BVMODL(N)	Bubble velocity based on BDMODL(N) (cm/s)
BVS	Swelling strain in region (L,K,J) due to gas bubbles

BVSJ	Swelling strain in section J due to gas bubbles
BVSL	Fractional gas bubble strain due to bubbles trapped in the lattice
BVSE	Fractional gas bubble strain due to bubbles trapped on grain edges
BVSF	Fractional gas bubble strain due to bubbles trapped on grain faces
BVVOL	Bubble velocity based on volume diffusion in a temperature gradient
CI	Fractional interstitial concentration in region (L,K,J)
CORN REGION K	Gas bubble concentration in each size class for bubbles on the grain faces (#/cm^3)
CV	Fractional vacancy concentration in region (L,K,J)
CVF	Cladding volume fraction
DCIE	Fission–enhanced diffusion coefficient (cm^2/s)
DELT	Time step (s)
DTDT	Heating rate in region (K,J) (K/s)
DTPJ	Fractional change in thickness of fuel plate in Section J
EDGE REGION K	Gas bubble concentration in each size class for bubbles on the grain edges (#/cm^3)
EDGEFR	Fraction of generated gas residing on the grain edges
EGRE	Rate of gas migration from grain faces to edges due to grain face channel formation (s^{-1})

EPRF	Rate of gas atom release due to increased edge tunnel interconnection
ERR	Total fractional error in calculation
ERRJ	Fractional error in calculation in Section J
ERRK	Fractional error in calculation in Region (L,K,J)
ERRL	Fractional error in calculation in Section (J,L)
FACEFR	Fraction of generated gas residing on the grain faces
FBDEN	Fraction of grain face area per unit volume covered by bubbles
FDEN	Fission density (fissions/cm^3)
FDNTS	Fission density at which U_3Si_2 enters the unstable part of the U-Si phase diagram
FDX	Fission density at which fuel in region will recrystallize
FGRJ	Fractional gas release from Section J
FGRK	Fractional gas release from Region (L,K,J)
FGRL	Fractional gas release from Section (J,L)
FGRT	Total fractional gas release
FLUX	Rate at which gas is diffusing to the grain faces (atoms/cm^3/s)
GAMMA	Surface tension of fuel (dynes/cm)
GBS	Rate of intragranular gas release due to grain boundary sweeping mechanism (s^{-1})
GOTT	Total quantity of released fission gas (moles)

GOUJ	Total quantity of released fission gas in Section J (moles)
GOUK	Total quantity of released fission gas in Section (J,L) (moles)
GOUT	Total quantity of released fission gas in Region (L,K,J) (moles)
GRD	Grain size (cm)
GSGEN	Quantity of generated fission gas in Region (L,K,J) (moles)
GSGJ	Quantity of generated fission gas in Section J (moles)
GSGK	Quantity of generated fission gas in Section (J,L) (moles)
GSGT	Total quantity of generated fission gas (moles)
GSIN	Fission gas generation rate (atoms/s/cm^3)
H	Current time increment (s)
HNXT	Suggested value of next time increment (s)
IMX1 (L,K,J)	Total number of size classes considered during H in Region
IMX2	Total number of equations solved during H in Region (L,K,J)
J	Axial section
K	Radial section of fuel particle
L	Linear section of fuel plate (annular region of rod)
LDMK	Phase of region (LDMK = 0: normal; LDMK = 6: amorphous)
NCDI	Number of size classes for dislocation bubbles
NCEI	Number of size classes for edge bubbles
NCFI	Number of size classes for face bubbles

PBKGBY	Biased flux of gas to the grain faces (s^{-1})
POROS	Average as-fabricated porosity in fuel particle in region (K,J)
PRF	Pore interlinkage probability fraction at end of current time step
PRFOLD	Pore interlinkage probability fraction during the previous time step.
PRSO	Hydrostatic pressure in region (L,K,J) (lbs/cm^2)
PRSOL	Hydrostatic pressure on bubbles in section (J,L) (lbs/cm^2)
PRSOO	Hydrostatic pressure in region (L,K,J) during previous time step (lbs/cm^2)
RAD	Bubble radii (cm). Note: For grain faces and edges, RAD is the equivalent radius assuming a spherical shape, i.e., lenticular and ellipsoidal bubble geometries are used on grain faces and edges, respectively
RATIO	Fractional radius of Region (L,K,J)
RBD3	1/2 the interbubble spacing on dislocations
RBF3	1/2 the interbubble spacing on the faces
RBL3	1/2 the interbubble spacing in the lattice
RET	Retained quantity of fission gas in Region (L,K.J) (moles)
RETJ	Retained quantitiy of fission gas in Section J (moles)
RETK	Retained quantity of fission gas in Section (J,L) (moles)
RETT	Total quantity of retained fission gas (moles)
RGB	Quantity of retained gas in lattice (moles)

RGE	Quantity of retained fission gas on edges (moles)
RGF	Quantity of retained fission gas on faces (moles)
RGGB	Fraction of retained gas that resides in lattice
RGGE	Fraction of retained gas that resides on grain edges
RGGF	Fraction of gas retained that resides on grain faces
RGGL	Fracton of gas retained that resides in lattice and on dislocations
RPIN	Fraction of retained intragranular fission gas that resides in bubbles
RRCON	Fractional release rate of fission gas
RRGBIP	Rate at which gas is arriving at the grain edges (s^{-1})
RS(K,J), RS(K+1,J)	Radii of the two boundaries of Region (L,K,J) (cm)
SAVG(N)	Number of gas atoms/bubble in size class N: The last row is for the bubbles in the dead-end nodes
TFPV	Fission rate per unit volume in Region (L,K,J) (fissions/cm^3/s)
TGRAD	Temperature gradient in Region (K,J) (K/cm)
TK	Average temperature in Region (L,K,J) (K)
TS(K,J) TS(K+1,J)	Temperatures of the two boundaries of Region (L,K,J) (K)
TSWLK	Total fission-product-induced swelling strain in Section (J,L)
VAM	Aluminum volume fraction
VFM	Fuel volume fraction

VFMA	Fractional volume occupied by region of given phase
VOLTP	Fractional gas bubble strain due to bubbles trapped in dead-end nodes
VOLUME	Volume of the Region (L,K,J) (cm^3)
VPM	As-fabricated pore volume fraction
WKPAR	Change in themal conductivity of fuel particle due to irradiation-induced porosity (W/m/K)
XKDIS	Thermal conductivity of the dispersion in Section L (W/m/K)
XKDSJ	Thermal conductivity of the dispersion in Section J (W/m/K)
XKGXKU	Fractional change in thermal conducivity of fuel from as-fabricated value in Section L
XKUG	Thermal conductivity of fuel (W/m/K) in section L
XKU0	As-fabricated value of dispersion thermal conductivity (W/m/K) in Section L
XKU3SI2	Thermal conductivity of the fuel particle (W/m/K) in section L
XKXKU	Fractional change in thermal conductivity of dispersion from as-frabricated value in Section L

References

1. J. Rest, GRASS–SST: *A Comprehensive Mechanistic Model for the Prediction of Fission–Gas Behavior in UO2–Base Fuels during Steady–State and Transient Conditions*, NUREG/CR-2437 Vol. I, Argonne National Laboratory Report, ANL–78–53 (June 1978).

2. C. F. Reinke, *Irradiation and Postirradiation Annealing of Some Aluminum-Base Fuels*, Argonne National Laboratory Report, ANL-6665 (Sept. 1963).

3. M. M. Martin, A. E. Richt, and W. R. Martin, *Irradiation Behavior of Aluminum-Based Fuel Dispersions*, ORNL-4856, Oak Ridge National Laboratory (May 1973).

4. J. W. Blake, *A Mathematical Model of the Irradiation Behavior of Uranium Silicide Fuel Plates*, M.S. Thesis, Dept. of Mech. Eng., Northwestern University, Evanston, IL (June, 1984).

5. J. R. Matthews and M. H. Wood, *An Efficient Method for Calculating Diffusive Flow to a Spherical Boundary, Nucl. Eng. Des.* **56**, 439 (1980).

6. J. A. Turnbull and C. A. Friskney, *The Release of Fission Products from Nuclear Fuel During Irradiation by Both Lattice and Grain Boundary Diffusion, J. Nucl. Mater.* **58**, 31 (1975).

7. F. A. Nichols, *A Simplified Model for Stable Open Porosity, J. Nucl. Mater.* **148**, 92 (1987).

8. A. A. Solomon, A. Casagrowda, and J. Rest, *Swelling and Gas Release in UO_2 and Comparisons with FASTGRASS and OGRES Code Predictions, J. Nucl. Mater.* **154**, 332 (1988).

9. E. E. Gruber, *The Role of Bubble–Size Equilibration in the Transient Behavior of Fission Gas*, Argonne National Laboratory Report, ANL–78–36 (April 1978).

10. M. V. Speight and W. Beere, *Vacancy Potential and Void Growth on Grain Boundaries, Met. Sci.* **9**, 190 (1975).

11. M. Jakob, *Heat Transfer*, Wiley, London (1969), pp. 83-88.

12. W. H. McAdams, *Heat Transmission*, McGraw-Hill, New York (1954), p. 10, 1954.

13. D. R. Olander, *Fundamental Aspects of Nuclear Reactor Fuel Elements*, U.S. Dept. of Energy Publication, TID–26711–P1, (1976).

14. A. L. Loeb, *Thermal Conductivity: VIII, A Theory of Thermal Conductivity of Porous Materials*, J. Am. Ceram. Soc. **37**, 96 (1954).

15. H. Kamkpf and G. Karsten, *Effects of Different Types of Void Volumes as the Radial Temperature Distribution of Fuel Pins*, J. Nucl. Technol. **9**, 288 (1970).

16. G. A. Reymann and D. L. Hagrmann, *MATRPO–10: A Handbook of Material Properties for Use in the Analysis of LWR Fuel Rod Behavior*, TREE–NUREG–1180, EG&G–Idaho, Inc., Report, 1978.

17. Williams, R. K., Graves, R. S., Domagala, R. F., and Wiencek, T. C., *Thermal Conductivities of U_3Si and U_3Si_2-Al DISPERSION FUELS*, in Thermal Conductivity, **19**, Plenum Publishing Corp.,(1988), p. 271.

18. I. J. Hastings, J. R. MacEwan, and L. R. Bourque, *Effect of Swelling on Thermal Conductivity and Postirradiation Densification of U_3Si*, J. Amer. Ceram. Soc., **55** (5), 240 (1972).

19. G. L. Hofman and J. L. Snelgrove, Material Science and Technology, *A Comprehensive Treatment*, edited by R. W. Cahn, P. Haasen, and E. J. Kramer, Nuclear Materials, Part 1, edited by B. R. T. Frost, Vol. 10A, Chapter 2, Published by VCH Verlagsgesellschaft mbH, Federal Republic of Germany (1994).

20. G. L. Hofman, private communication, Argonne National Laboratory (1995).

21. J. Rest and G. L. Hofman, *Mechanistic Interpretation of an Observed Fission-Rate Dependence of Low-Temperature Swelling of Irradiated Uranium Silicide Dispersion Fuels*, in Effects of Radiation on Materials, 15th Intl. Symp. (Vol. II), ASTM STP 1125, R. E. Stoller, A. S. Kumar, and D. S. Gelles, eds., Am. Soc. Testing Mater., Philadelphia (1992), pp. 797-809.

22. J. Rest and G. L. Hofman, *Kinetics of Recrystallization and Fission-Gas-Induced Swelling in High Burnup UO_2 and U_3Si_2 Nuclear Fuels*, in Fundamental Aspects of Inert Gases in Solids, S. E. Donnelly and J. H. Evans, eds., Plenum Press, New York (1991), p. 443.

23. J. Rest and G. L. Hofman, *Dynamics of irradiation-induced grain subdivision and swelling in U_3Si_2 and UO_2 fuels*, J. Nucl. Mater. **210**, 187 (1994).

24. J. Rest, G. L. Hofman, and R. C. Birtcher, *The Effect of Crystal Structure Stability on Swelling in Intermetallic Compounds*, in Effects of Radiation on Materials, 14th Intl. Symp. (Vol. II), ASTM STP 1046, N. H. Packan, R. E. Stoller, and A. S. Kumar, eds., (Am. Soc. for Testing Mater., Philadelphia (1990), pp. 789-811.

25. M. L. Bleiberg, R. M. Berman, and B. Lustman, *Effects of High Burn-Up on Oxide Ceramic Fuels*, in Symp. on Radiation Damage in Solid and Reactor Materials, Proc. Series, IAEA, Venice (1963), p. 319.

26. J. D. B. Lambert, Met. Soc. Conf., Vol. 42, High Temperature Nuclear Fuels, Gordon and Breach, New York (1968), pp. 237–254.

27. C. T. Walker, T. Kameyama, S. Kitajima, and M. Kinoshita, *Concerning the microstructure changes that occur at the surface of UO_2 pellets on irradiation to high burnup*, J. Nucl. Mater. **188**, 73 (1992).

28. L. E. Thomas, C. E. Bexer, and L. A. Charlot, *Microstructural analysis of LWR spent fuels at high burnup*, Ibid, p. 80.

29. K. Une, K. Nogita, S. Kashine, and M. Imamura, *Microstructural change and its influence on fission gas release in high burnup UO_2 fuel*, Ibid, p. 65.

30. I. L. F. Ray, H. Thiele, and H. Matzke, *Transmission electron microscopy study of fission product behavior in high burnup UO_2,*, Ibid, p. 90.

31. H. J. Matzke, *On the rim effect in high burnup UO_2 LWR fuels*, J. Nucl. Mater. **189**, 141 (1992).

32. R. C. Birtcher and L. M. Wang, *Stability of Uranium Silicides During High Energy Ion Irradiation*, presented at 7th Intl. Conf. on Ion Beam Modification of Materials (IBMM90, Knoxville, TN, Sept. 9–14, 1990.

33. W. D. Kingery, H. R. Bowen, and D. R. Uhlman, *Introduction to Ceramics*, 2nd Ed. Wiley, New York, 1976, p. 449.

34. T. Furu, K. Karthinsen, and E. Nes, *Modeling recrystallisation*, Mater. Sci. Technol. **6**, 1093 (1990).

35. N. Hansen, *Cold deformation microstructures*, Mater. Sci. Technol. **6**, 1039 (1990).

36. D. Kuhlman-Wilsdorf, *Fundamentals of Cell and Subgrain Structures in Historical Perspective,* Scripta. Met. Mater. **27**, 951 (1992).

37. F. A. Garner and W. G. Wolfer, *A Model for the Evolution of Network Dislocation Density in Irradiated Metals*, in Effects of Radiation on Materials: 11th Conf. ASTM STP 782, H. R. Bragen and J. S. Perkin, eds., Am. Soc. Test. Mater., Phildelphia (1982) p. 1073.

38. A. R. Jones, *Grain Boundary Phenomena During the Nucleation of Recrystallization*, in Grain Boundary Structure and Kinetics, American Society of Metals, Milwaukee, WI (1980) p. 379.

39. R. W. Cahn, *A New Theory of Recrystallization Nuclei*, Proc. Roy. Soc., **60A**, 323 (1950).

40. P. A. Beck, *The Formation of Recrystallization Nuclei*, J. Appl. Phys., **20**, 633 (1949).

41. A. H. Cottrell, *Theory of Dislocations*, Prog. Met. Phys., **4**, 205 (1953).

42. S. J. Zinkle, R. A. Dodd, and G. L. Kulcinski, *Comparison of Thermal and Irradiated Behavior of High-Strength High-Conductivity Copper Alloys*, in Effects of Radiation on Materials, 12th Intl. Symp., ASTM STP 870, F. A. Garner and J. S. Perkin, eds., Am. Soc. Test. Mater., Philadelphia (1985) p. 363.

43. G. Das and T. E. Mitchell, *Recrystallization Induced by Electron Irradiation of Deformed Nickel*, Scripta Met, **8**, 1135 (1974).

44. S. M. Murphy, *A Model for Segregation in Dilute Alloys During Irradiation*, J. Nucl. Mater. **168**, 31 (1989).

45. J. Rest, Argonne National Laboratory, unpublished information (1990).

46. R. A. Johnson and N. Q. Lam, *Solute segregation in metals under irradiation*, Phys. Rev. B. 13, 4364 (1976).

47. R. A. Dugdale, *Some Properties of Vacancies and Interstitials in CU_3Au*, Phil. Mag. **1**, 537 (1956).

48. S. J. Rothman, N. Q. Lam, R. Sizmann, and H. Bisswanger, *Buildup of Point-Defect Diffusion Profiles in a Foil During Irradiation*, Rad. Effects **20**, 223 (1973).

49. J. Rest and S. A. Zawadzki, FASTGRASS: *A Mechanistic Model for the Prediction of Xe, I, Cs, Te, Ba and Sr Release from Nuclear Fuel under Normal and Severe Accident Conditions*, NUREG/CR–5840, Argonne National Laboratory Report ANL–92/3 (1992).

50. K. Nogita and K. Une, *Radiation-induced microstructural change in high burnup UO_2 fuel pellets*, Nucl. Instr. Meth. B **91**, 301 (1994).

51. P. R. Okamoto, L. E. Rehn, J. Pearson, R. Bhadra, and M. Grimsditch, Procedures of Materials Research Society Meeting, Vol. 100, Boston, MA, Nov. 1987, pp.51-56

52. P. R. Okamoto, L. E. Rehn, J. Pearson, R. Bhadra, and M. Grimsditch, *Brillouin Scattering and Transmission Electron Microscopy Studies of Radiation-Induced Elastic Softening, Disordering, and Amorphization of Intermetallic Compounds,* Journal of Less Common Metals, Vol. 140, 1988, pp. 231-244.

53. E. M. Schulson, *The Ordering and Disordering of Solid Solutions under Irradiation,* J. Nucl. Mater, **83,** 239 (1979).

54. Fu-rong Ding, R. S. Averback, and H. Hahn, *Radiation-enhanced diffusion in Ni/Zr diffusion couples,* J. Appl. Phys., **64**, 1785 (1988).

55. T. Diaz de la Rubia, R. S. Averback, R. Benedek, and W. E. King, *Role of Thermal Spikes in Energetic Displacement Cascades,* Phys. Rev. Let., **59**, 1930 (1987).

56. Gerard L. Hofman and Woo-Esog Ryu, *Detailed Analysis of Uranium Silicide Dispersion Fuel Swelling,* 12th Intl. Meeting on Reduced Enrichment for Research and Test Reactors, Sept. 10-14, 1989, IBSN 3-89336-063-8 (1991), pp. 115-135.

Distribution for ANL-95/36

Internal:

D. E. Alexander
P. I. Amundson
R. C. Birtcher
Y. I. Chang
M. H. Derbidge
D. R. Diercks
B. D. Dunlap
D. W. Green
G. L. Hofman
C. E. Klotz
L. G. LeSage
M. J. Lineberry
C. A. Malefyt
J. E. Matos
L. A. Neimark
R. B. Poeppel
L. E. Rehn
J. Rest (20)
J. I. Sackett
W. J. Shack
J. L. Snelgrove (2)
M. J. Steindler
H. R. Thresh
C. E. Till
A. Travelli (10)
D. C. Wade
L. C. Walters
R. W. Weeks
T. C. Wiencek
TIS Files

External:

DOE–OSTI, for distribution per UC–505(98)
ANL Libraries
ANL-E (2)
ANL-W
Manager, Chicago Field Office, DOE
Energy Technology Division Review Committee:
H. K. Birnbaum, University of Illinois, Urbana
R. C. Buchanan, University of Cincinnati, Cincinnati
M. S. Dresselhaus, Massachusetts Institute of Technology, Cambridge, MA
H. S. Rosenbaum, Fremont, CA
R. K. Shah, General Motors Corp., Lockport, NY
S. Smialowska, Ohio State University, Columbus
S. N. Liu, Fremont, CA
R. E. Smith, Altran Corp., Huntersville, NC
AEA Technology, Thurso Caithness, Scotland
J. Gibson
D. Thom
V. G. Aden, ENTEK, Moscow, Russia
E. Adolph, RISØ National Laboratory, Roskilde, Denmark
Babcock & Wilcox Co., Lynchburg, VA
K. R. Catlett
B. W. Pace
Jean–Pierre Durand, CERCA, Sur Isere, France
Y. Fanjas, CERCA, Romans Cedex, France
G. Gruber, Fuel Cycle Serv. Div., NUKEM GmbH, Alzenau, Germany
JAERI, Ibaraki–ken, Japan
Y. Komori,
T. Nakajima
K. Kanda, Research Reactor Institute, Kyoto University, Osaka, Japan

J. Klein, CHCEN La Reina, Santiago, Chile

KAERI, Taejon, Republic of Korea

I. H. Kuk

C. K. Kim

K. H. Kim

F. Merchie, Centre d'Etudes, Grenoble–Cedex, France

MINATOM, Moscow, Russia

N. Arkhangelsky

N. I. Ermakov

J. Mota, CEC, Euratom Supply Agency, Rue de la Loi, Brussels, Belgium

A. Nagler, SOREQ Nuclear Research Center, Yavne, Israel

NZChK, Chemelnitsky–96, Novosibirsk, Russia

A. B. Aleksandrov

A. A. Enin

Oak Ridge National Laboratory

G. L. Copeland

R. W. Knight

C. West

E. Perez, Comision Nacional de Energia Atomica, Buenos Aires, Argentina

F. Reitsma, Atomic Energy Commission of South Africa, Ltd., Pretoria, South Africa

D. Sears, Atomic Energy of Canada, Ltd., Chalk River Laboratories, Chalk River, Ontario, Canada

VNIINM, Moscow, Rogova, Russia

G. A. Srakhova

Aleksandr V. Vatulyn

A. Suripto, National Atomic Energy Agency (BATAN) Kawasan, Puspiptek, Serpong, Indonesia